

Abstract

Measurement of total hadronic differential cross sections in the LArIAT experiment

Elena Gramellini

2018

6 Abstract goes here. Limit 750 words.

Measurement of total hadronic differential cross sections in the LArIAT experiment

A Dissertation
Presented to the Faculty of the Graduate School
of
Yale University
in Candidacy for the Degree of
Doctor of Philosophy

15 by
16 Elena Gramellini

¹⁷ Dissertation Director: Bonnie T. Fleming

18 Date you'll receive your degree

¹⁹

Copyright © 2017 by Elena Gramellini

²⁰

All rights reserved.

²¹ Contents

²²	Acknowledgements	vii
²³	0 Introduction	1
²⁴	1 The theoretical framework	2
²⁵	1.1 The Standard Model	2
²⁶	1.2 Neutrinos: tiny cracks in the Standard Model	4
²⁷	1.2.1 Neutrinos in the Standard Model	4
²⁸	1.2.2 Neutrino Oscillations	6
²⁹	1.2.3 Make up of Neutrino Interactions	7
³⁰	1.3 Beyond the Standard Model	11
³¹	1.3.1 Open Questions in Neutrino Physics	11
³²	1.3.2 Towards a more fundamental theory: GUTs	15
³³	1.4 Motivations for Hadronic Cross Sections in Argon	18
³⁴	1.4.1 Pion-Argon Total Hadronic Cross Section	19
³⁵	1.4.2 Kaon-Argon Total Hadronic Cross Section	29
³⁶	2 Liquid Argon Detectors at the Intensity Frontier	34
³⁷	2.1 The Liquid Argon Time Projection Chamber Technology	34
³⁸	2.1.1 TPCs, Neutrinos & Argon	34
³⁹	2.1.2 LArTPC: Principles of Operation	38

40	2.1.3	Liquid Argon: Ionization Charge	39
41	2.1.4	Liquid Argon: Scintillation Light	45
42	2.1.5	Signal Processing and Event Reconstruction	49
43	2.2	The Intensity Frontier Program	53
44	2.2.1	Prospects for LArTPCs in Neutrino Physics: SBN and DUNE	53
45	2.2.2	Prospects for LArTPCs in GUT Physics: DUNE	55
46	2.2.3	Enabling the next generation of discoveries: LArIAT	56
47	3	LArIAT: Liquid Argon In A Testbeam	59
48	3.1	The Particles Path to LArIAT	59
49	3.2	LArIAT Tertiary Beam Instrumentation	61
50	3.2.1	Bending Magnets	62
51	3.2.2	Multi-Wire Proportional Chambers	64
52	3.2.3	Time-of-Flight System	66
53	3.2.4	Punch-Through and Muon Range Stack Instruments	67
54	3.2.5	LArIAT Cosmic Ray Paddle Detectors	69
55	3.3	In the Cryostat	70
56	3.3.1	Cryogenics and Argon Purity	70
57	3.3.2	LArTPC: Charge Collection	73
58	3.3.3	LArTPC: Light Collection System	76
59	3.4	Trigger and DAQ	78
60	3.5	Control Systems	80
61	4	Total Hadronic Cross Section Measurement Methodology	86
62	4.1	How to Measure a Hadron Cross Section in LArIAT	86
63	4.1.1	Event Selection	87
64	4.1.2	Wire Chamber to TPC Match	89
65	4.1.3	The Thin Slice Method	90

66	4.1.4	Procedure testing with truth quantities	93
67	5	Samples Preparation	96
68	5.1	LArIAT Data	96
69	5.2	LArIAT Monte Carlo	96
70	5.2.1	G4Beamline	97
71	5.2.2	Data Driven MC	97
72	5.3	Energy Calibration	99
73	5.4	Tracking Studies	103
74	5.4.1	Selection Study for the Wire Chamber to TPC Match	103
75	5.4.2	Interaction Point Optimization	106
76	5.4.3	Tracking spatial and angular resolution	107
77	6	Background subtraction	108
78	6.1	Assessing Beamline Contamination	108
79	6.1.1	Electron and Muon contamination	109
80	6.1.2	Contamination from secondaries	111
81	6.2	Beamline Background Subtraction	111
82	6.3	Capture and decay	114
83	7	Negative Pion Cross Section Measurement	117
84	7.1	Estimate of E_{loss} before the TPC	117
85	7.2	Interacting and Incident Distributions	120
86	7.3	Total Hadronic Negative Pion-Argon Differential Cross Section	120
87	8	Uncertainty budget	121
88	8.1	Pure beam of pions	121
89	8.1.1	Uncertainty on E_{Beam}^{kin}	122
90	8.1.2	Systematics on E_{loss}	122

91	8.1.3 Uncertainty on dE/dx and pitch	123
92	8.1.4 Uncertainty on track end, aka efficiency correction	123
93	A Measurement of LArIAT Electric Field	124

⁹⁴ Acknowledgements

⁹⁵ A lot of people are awesome, especially you, since you probably agreed to read this

⁹⁶ when it was a draft.

₉₇ Chapter 0

₉₈ Introduction

₉₉ **Chapter 1**

₁₀₀ **The theoretical framework**

₁₀₁ **1.1 The Standard Model**

₁₀₂ The Standard Model (SM) of particle physics is the most accurate theoretical descrip-
₁₀₃ tion of the subatomic world and, in general, one of the most precisely tested theories
₁₀₄ in the history of physics. The SM describes the strong, electromagnetic and weak
₁₀₅ interactions among elementary particles in the framework of quantum field theory,
₁₀₆ accounting for the unification of electromagnetic and weak interactions for energies
₁₀₇ above the vacuum expectation value (VEV) of the Higgs field. The SM does not
₁₀₈ describe gravity or general relativity.

₁₀₉ The Standard Model is a gauge theory based on the local group of symmetry

$$G_{SM} = SU(3)_C \otimes SU(2)_T \otimes U(1)_Y \quad (1.1)$$

₁₁₀ where the subscripts indicate the conserved charges: the strong charge, or color C,
₁₁₁ the weak isospin T (or rather its third component T3) and the hypercharge Y. These
₁₁₂ quantities can be related to the electric charge Q through the Gell-Mann-Nishijima
₁₁₃ relation:

$$Q = \frac{Y}{2} + T_3. \quad (1.2)$$

Generation	I	II	III	T	Y	Q
Leptons	$\begin{pmatrix} \nu_e \\ e \end{pmatrix}_L$	$\begin{pmatrix} \nu_\mu \\ \mu \end{pmatrix}_L$	$\begin{pmatrix} \nu_\tau \\ \tau \end{pmatrix}_L$	1/2 -1/2	-1 -1	0 -1
	e_R	μ_R	τ_R	0	-2	1
Quarks	$\begin{pmatrix} u \\ d' \end{pmatrix}_L$	$\begin{pmatrix} c \\ s' \end{pmatrix}_L$	$\begin{pmatrix} t \\ b' \end{pmatrix}_L$	1/2 -1/2	1/3 1/3	2/3 -1/3
	u_R d'_R	c_R s'_R	t_R b'_R	0 0	4/3 -2/3	2/3 -1/3

Table 1.1: SM elementary fermions. The subscripts L and R indicate respectively the negative helicity (left-handed) and the positive helicity (right-handed).

114 In the quantum field framework, the elementary particles correspond to the ir-
 115 reducible representations of the G_{SM} symmetry group. In particular, the particles
 116 are divided in two categories, fermions and bosons, according to their spin-statistics.
 117 Described by the Fermi-Dirac statistics, fermions have half-integer spin and are some-
 118 times called “matter-particles”. Bosons or “force carriers” have integer spin, follow
 119 the Bose-Einstein statistics and mediate the interaction between fermions. The fun-
 120 damental fermions and their quantum numbers are listed in Tab 1.1.

121 Quarks can interact via all three the fundamental forces; they are triplets of
 122 $SU(3)_C$, that is they can exist in three different colors: C = R, G, B. If one chooses
 123 a base where u , c and t quarks are simultaneously eigenstates of both the strong
 124 and the weak interactions, the remaining eigenstates are usually written as d , s and
 125 b for the strong interaction and d' , s' and b' for the weak interaction, because the
 126 latter ones are the result of a Cabibbo rotation on the first ones. Charged leptons
 127 interact via the weak and the electromagnetic forces, while neutrinos only interact
 128 via the weak force. The gauge group univocally determines the number of gauge
 129 bosons that carry the interaction; the gauge bosons correspond to the generators of

130 the group: eight gluons (g) for the strong interaction, one photon (γ) and three bosons
 131 (W^\pm , Z^0) for the electroweak interaction. A gauge theory by itself cannot provide
 132 a description of massive particles, but it is experimentally well known that most of
 133 the elementary particles have non-zero masses. The introduction of massive fields in
 134 the Standard Model lagrangian would make the theory non-renormalizable, and - so
 135 far - mathematically impossible to handle. This problem is solved in the SM by the
 136 introduction of a scalar iso-doublet $\Phi(x)$, the Higgs field, which gives mass to W^\pm and
 137 Z^0 gauge bosons through the electroweak symmetry breaking mechanism and to the
 138 fermions through Yukawa coupling [70, 71]. The discovery of the Higgs boson in 2012
 139 by the LHC experiments [36, 37] marked the ultimate confirmation of a long history
 140 of successful predictions by the SM.

141 **1.2 Neutrinos: tiny cracks in the Standard Model**

142 **1.2.1 Neutrinos in the Standard Model**

143 Neutrino were introduced in the SM as left-handed massless Weyl spinors. The Dirac
 144 equation of motion

$$(i\gamma^\mu \partial_\mu - m)\psi = 0 \quad (1.3)$$

145 for a fermionic field

$$\psi = \psi_L + \psi_R \quad (1.4)$$

146 is equivalent to the equations

$$i\gamma^\mu \partial_\mu \psi_L = m\psi_R \quad (1.5)$$

147

$$i\gamma^\mu \partial_\mu \psi_R = m\psi_L \quad (1.6)$$

148 for the chiral fields ψ_R and ψ_L , whose evolution in space and time is coupled
 149 through the mass m . If the fermion is massless, the chiral fields decouple and the

150 fermion can be described by a single Weyl spinor with two independent components [108]. Pauli initially rejected the description of a physical particle through
 151 a single Weyl spinor because of its implication of parity violation. In fact, since the
 152 spatial inversion operator throws $\psi_R \leftrightarrow \psi_L$, parity is conserved only if the both the
 153 chiral components exist at the same time. For the neutrino introduction in the SM,
 154 experiments came in help of the theoretical description. The constraint of parity
 155 conservation weakened after Wu's experiment in 1957 [111]. Additionally, there was
 156 no experimental indication for massive neutrinos, nor evidence of interaction via the
 157 neutrino right-handed component.
 158

159 The symmetry group $SU(2)_T \otimes U(1)_Y$ is the only group relevant for neutrino
 160 interactions. The SM electroweak lagrangian is the most general renormalizable la-
 161 grangian invariant under the local symmetry group $SU(2)_T \otimes U(1)_Y$. The lagrangian
 162 couples the weak isotopic spin doublets and singlets described in Table 1.1 with the
 163 gauge bosons A_a^μ ($a = 1,2,3$) and B^μ , and Higgs doublet $\Phi(x)$:
 164

$$\begin{aligned}
 \mathcal{L} = & i \sum_{\alpha=e,\mu,\tau} \bar{L}'_{\alpha L} \not{D} L'_{\alpha L} + i \sum_{\alpha=1,2,3} \bar{Q}'_{\alpha L} \not{D} Q'_{\alpha L} \\
 & + i \sum_{\alpha=e,\mu,\tau} \bar{l}'_{\alpha R} \not{D} l'_{\alpha R} + i \sum_{\alpha=d,s,b} \bar{q}'^D_{\alpha R} \not{D} q'^D_{\alpha R} + i \sum_{\alpha=u,e,t} \bar{q}'^U_{\alpha R} \not{D} q'^U_{\alpha R} \\
 & - \frac{1}{4} A_{\mu\nu} A^{\mu\nu} - \frac{1}{4} B_{\mu\nu} B^{\mu\nu} \\
 & + (D_\rho \Phi)^\dagger (D^\rho \Phi) - \mu^2 \Phi^\dagger \Phi - \lambda (\Phi^\dagger \Phi)^2 \\
 & - \sum_{\alpha,\beta=e,\mu,\tau} \left(Y_{\alpha\beta}^n \bar{L}'_{\alpha L} \Phi l'_{\beta R} + Y_{\alpha\beta}^{n*} \bar{l}'_{\beta R} \Phi^\dagger L'_{\alpha L} \right) \\
 & - \sum_{\alpha=1,2,3} \sum_{\beta=d,s,b} \left(Y_{\alpha\beta}^D \bar{Q}'_{\alpha L} \Phi q'^D_{\beta R} + Y_{\alpha\beta}^{D*} \bar{q}'^D_{\beta R} \Phi^\dagger Q'_{\alpha L} \right) \\
 & - \sum_{\alpha=1,2,3} \sum_{\beta=u,c,t} \left(Y_{\alpha\beta}^U \bar{Q}'_{\alpha L} \tilde{\Phi} q'^U_{\beta R} + Y_{\alpha\beta}^{U*} \bar{q}'^U_{\beta R} \tilde{\Phi}^\dagger Q'_{\alpha L} \right). \tag{1.7}
 \end{aligned}$$

164 The first two lines of the lagrangian summarize the kinetic terms for the fermionic

165 fields and their coupling to the gauge bosons $A_a^{\mu\nu}$, $B^{\mu\nu}$ ¹. The third line describes
166 the kinetic terms and the self-coupling terms of the gauge bosons. The forth line is
167 the Higgs lagrangian, which results in the spontaneous symmetry breaking. The last
168 three lines describe the Yukawa coupling between fermions and the Higgs field, origin
169 of the fermions' mass.

170 The coupling between left-handed and right-handed field generates the mass term
171 for fermions. The SM assumes only left-handed components for neutrinos, thus im-
172 plying zero neutrino mass. Since any linear combination of massless fields results in a
173 massless field, the flavor eigenstates are identical to the mass eigenstates in the SM.

174 1.2.2 Neutrino Oscillations

175 The determination of the flavor of a neutrino dynamically arises from the correspond-
176 ing charged lepton associated in a change current interaction; for example, a ν_e is a
177 neutrino which produces an e^- , a $\bar{\nu}_\mu$ is a neutrino which produces a μ^+ , etc. The
178 neutrino flavor eigenstates $|\nu_\alpha\rangle$, with $\alpha = e, \mu, \tau$, are orthogonal to each other and
179 form a base for the weak interaction matrix.

180 Overwhelming experimental data show that neutrinos change flavor during their
181 propagation [95]. This phenomenon, called “neutrino oscillations”, was predicted
182 first by Bruno Pontecorvo in 1957 [96]. Neutrino oscillations are possible only if the
183 neutrino flavor eigenstate are not identical to the mass eigenstates, thus resulting in
184 the first evidence of physics beyond the Standard Model. A minimal extension of the
185 SM introduces three mass eigenstates, $|\nu_i\rangle$ ($i = 1, 2, 3$), whose mass m_i is well defined.
186 The unitary Pontecorvo-Maki-Nakagawa-Sakata matrix transforms the spinor wave
187 functions (ψ) of each component between the flavor and mass bases as follows

187 1. In gauge theories the ordinary derivative ∂_μ is substituted with the covariant derivative D_μ . Here $D_\mu = \partial_\mu + igA_\mu \cdot I + ig'B_\mu \frac{Y}{2}$, where I and Y are the $SU(2)_L$ and $U(1)_Y$ generators, respectively.

$$\sum_{\alpha} \psi_{\alpha} |\nu_{\alpha}\rangle = \sum_i \psi_i |\nu_i\rangle, \rightarrow \psi_{\alpha} = U_{PMNS} \psi_i, \quad (1.8)$$

188 with

$$U_{PMNS} = \begin{bmatrix} c_{12} & s_{12} & 0 \\ -s_{12} & c_{12} & 0 \\ 0 & 0 & 1 \end{bmatrix} \begin{bmatrix} c_{13} & 0 & s_{13} e^{-i\delta} \\ 0 & 1 & 0 \\ -s_{13} e^{-i\delta} & 0 & c_{13} \end{bmatrix} \begin{bmatrix} 1 & 0 & 0 \\ 0 & c_{23} & s_{23} \\ 0 & -s_{23} & c_{23} \end{bmatrix} \begin{bmatrix} e^{i\alpha_1} & 0 & 0 \\ 0 & e^{i\alpha_2} & 0 \\ 0 & 0 & 1 \end{bmatrix} \quad (1.9)$$

189 where c e s stand respectively for cosine and sine of the corresponding mixing
190 angles (θ_{12} , θ_{23} and θ_{13}), δ is the Dirac CP violation phase, α_1 and α_2 are the eventual
191 Majorana CP violation phases. Experimental results on neutrino oscillations are
192 generally reported in terms of the mixing angles and of the squared mass splitting
193 $\Delta m_{ab}^2 = m_a^2 - m_b^2$, where a and b represent the mass eigenstates. A summary of the
194 current status of experimental results, albeit partial, is given in table 1.2.

Table 1.2: Summary of experimental results on neutrino oscillation parameters. ADD CITATIONS

	Value	Precision	Experiment
θ_{23}	45°	9.0%	Super Kamiokande, MINOS,
Δm_{23}^2	$2.5 \cdot 10^{-3} \text{ eV}^2$	1.8%	No ν a, MACRO
θ_{12}	34°	5.8%	SNO, Gallex,
Δm_{12}^2	$7.4 \cdot 10^{-5} \text{ eV}^2$	2.8%	SAGE, KamLAND
θ_{13}	9°	4.7%	DAYA Bay,
Δm_{13}^2	$2.5 \cdot 10^{-3} \text{ eV}^2$	1.8%	RENO

195 1.2.3 Make up of Neutrino Interactions

196 All neutrino experiments involving the detection of single neutrinos are concerned
197 with neutrino interactions (and neutrino cross sections) on nuclei. Given the invis-
198 ible nature of the neutrino, characterizing the products of its interaction is the only

199 method to a) assess the neutrino presence, b) detect its flavor in case of a charge
200 current interaction and c) eventually reconstruct its energy.

201 Historically, neutrino interactions with the nucleus in the GeV region are divided
202 into three categories as a function of increasing neutrino energy: quasi elastic (QE),
203 resonant (RES), and deep inelastic (DIS) scattering. All current and forthcoming
204 oscillation experiments live in the 0.1-10 GeV transition region, which encompasses
205 the energy where the QE neutrino-nucleus interaction transitions into RES and the
206 energy where RES transitions into DIS. Schematically, neutrino and antineutrino QE
207 charge current scattering refers to the process $\nu_l n \rightarrow l^- p$ and $\bar{\nu}_l p \rightarrow l^+ n$ where a
208 charged lepton and single nucleon are ejected in the elastic interaction, leaving the
209 target nucleus in its ground state. Resonant scattering refers to an inelastic colli-
210 sion producing a nucleon excited state (Δ, N^*) – the resonance, indeed – which then
211 quickly decays, most often to a nucleon and single-pion final state. DIS refers to the
212 head-on collision between the neutrino and a parton inside the nucleon, producing
213 hadronization and subsequent abundant production of mesons and nucleons. In addi-
214 tion to such interactions between the neutrino and a single component of the nucleus,
215 neutrinos can also interact with the nucleus as a whole, albeit more rarely, a well
216 documented process called coherent meson production scattering [53]; the signature
217 of such process is the production of a distinctly forward-scattered single meson final
218 state, most often a pion. This simple picture of neutrino interactions works rather
219 well for scattering off of light nuclear targets, such as the H₂ and D₂ of bubble cham-
220 ber experiments [59], but the complexity of the nuclear structure for heavier nuclei
221 such as argon complicates this model.

222 As we will discuss in Chapter 2, the properties of argon make it a good candidate
223 for interacting medium in neutrino experiments; in particular the density of its in-
224 teraction centers augments the yield of neutrino interactions and allows for relatively
225 compact detectors. Though, the choice of a relatively heavy nuclear target comes at

226 the cost of enhancing nuclear effects which modify the kinematic and final state of
227 the neutrino interaction products.

228 Nuclear effects can potentially affect the neutrino event rates, nucleon emission,
229 neutrino energy reconstruction, and the neutrino/antineutrino ratios, carrying deep
230 implications for oscillation experiments. Even in the case of “simple” QE scattering,
231 intra-nuclear hadron rescattering and correlation effects between the target nucleons
232 can cause the ejection of additional nucleons in the final state, modifying the final
233 state kinematics and topology. In case of resonant and DIS scattering, the hadronic
234 interactions of meson and nucleons produced in the decay of the resonance or dur-
235 ing hadronization complicate this picture even more. A large source of uncertainty
236 in modeling nuclear effects in neutrino interactions come from mesons interactions
237 (and re-interactions) in the nucleus, e.g., pion re-scattering, charge exchange, and
238 absorption.

239 A renewed interest for neutrino cross section measurements surged in recent years,
240 along with a lively discussion on the data reporting; the historical method of reporting
241 the neutrino cross section as a function of the neutrino energy or momentum trans-
242 fered shakes under the weight of its dependency on the chosen nuclear model. On one
243 hand, correcting for nuclear effects in neutrino interaction can introduce unwanted
244 sources of uncertainty and model dependency especially due to the mis-modeling of
245 the meson interactions. On the other, avoiding this correction makes a comparison
246 between neutrino interactions on different target nuclei extremely difficult.

247 Data on neutrino scattering off many different nuclei are available for both charged
248 current (CC) and neutral current (NC) channels, as summarized in [59]. A summary
249 of the results on QE, resonant and DIS scattering for neutrinos and antineutrinos from
250 accelerators on different target is reported in Figure 1.1, where the (NUANCE) [33]
251 event generator is used as comparison with the theory.

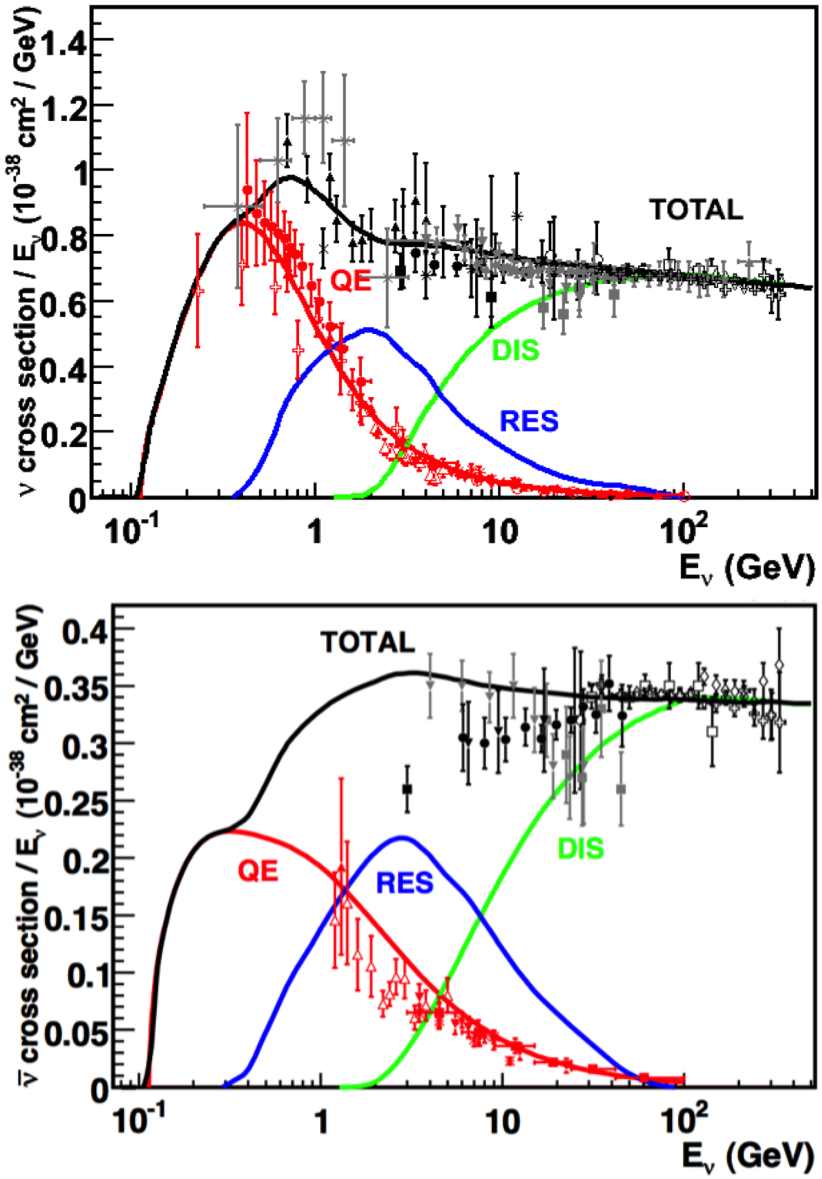


Figure 1.1: Total neutrino (top) and antineutrino (bottom) CC cross sections per nucleon divided by neutrino energy as a function of energy as reported in [59]. Predictions for the total (black), the QE (red), resonant (blue) and DIS (green) are provided by the NUANCE generator. The quasi-elastic scattering data and predictions have been averaged over neutron and proton targets (isoscalar target).

252 1.3 Beyond the Standard Model

253 The discovery of neutrino oscillation and its implication of non-zero neutrino mass
254 mark the beginning of a new, exciting era in neutrino physics: the era of physics Be-
255 yond the Standard Model (BSM) at the intensity frontier. We are currently searching
256 for new, deeper theories that can accommodate neutrinos with tiny but non-zero
257 masses, while remaining consistent with the rest of the Standard Model.

258 1.3.1 Open Questions in Neutrino Physics

259 On one hand, the last three decades of experiments in neutrino oscillations brought
260 spectacular advancements in the understanding of the oscillations pattern, measuring
261 the neutrino mixing angles and mass splitting with a precision of less than 10%. On
262 the other, they opened the field for a series of questions needing experimental answers.

263 **Sterile neutrinos.** Hints to the existence of at least one additional neutrino,
264 in the form of various anomalies, have been puzzling physicists almost from the be-
265 ginning of neutrino oscillation searches. Originally designed to look for evidence of
266 neutrino oscillation, the Liquid Scintillator Neutrino Detector (LSND) [49] provided
267 a first conflicting result with the Standard Model expectation of only three neutrinos.
268 A second conflicting result has also been provided by the MiniBooNE experiment [45].

269 The LSND and MiniBooNE ν_e and $\bar{\nu}_e$ appearance results, known as the “LSND and
270 MiniBooNE anomalies” [13, 14, 21], may be interpreted under the assumption of a new
271 right-handed neutrino. The additional neutrino needs to be “sterile”, i.e needs not
272 to couple with the electroweak force carriers, in order to meet the constraint imposed
273 by the measurement of the width of the Z boson [1]. The new sterile neutrino would
274 mainly be composed of a heavy neutrino ν_4 with mass m_4 such that $m_1, m_2, m_3 \ll m_4$
275 and $\Delta m^2 = \Delta m_{14}^2 \sim [0.1 - 10]$ eV². The introduction of sterile neutrinos is an ap-
276 pealing line of thinking, since this renormalizable generalization of the SM has the

277 potential to impact long standing questions in high energy physics and cosmology:
 278 light sterile neutrinos are candidates for dark matter particles and there are ideas
 279 that the theory could be adjusted to explain the baryon asymmetry of the Universe
 280 via leptogenesis [66].

281 **CP Violation In Lepton Sector.** The measurement of non-zero value for the
 282 oscillation parameter θ_{13} allows the exploration of low-energy CP violation in the lep-
 283 ton sector at neutrino long baseline oscillation experiments, enabling the possibility
 284 to measure the Dirac CP-violating phase δ . Exciting theoretical results tie δ directly
 285 to the generation of the baryon asymmetry of the Universe at the Grand Unified
 286 Theory scale **a couple of cit would be nice**. According to the theoretical model de-
 287 scribed in [94], for example, leptogenesis can be achieved if $|\sin \theta_{13} \sin \delta| > 0.11$, i.e.
 288 $\sin \delta > 0.7$.

289 The asymmetry in the oscillation probability of neutrinos and antineutrinos is the ob-
 290 servable sensitive to the Dirac CP-violating phase δ leveraged in neutrino oscillation
 291 experiments. Using the parameterization of the PMNS matrix shown in Equation
 292 1.9, the difference between the probability of $\nu_e \rightarrow \nu_\mu$ oscillation and the probability
 293 of $\bar{\nu}_e \rightarrow \bar{\nu}_\mu$ oscillation can be parametrized as follows [34],

$$P_{\nu_e \rightarrow \nu_\mu} - P_{\bar{\nu}_e \rightarrow \bar{\nu}_\mu} = J \cos \left(\pm \delta - \frac{\Delta_{31} L}{2} \right) \sin \left(\frac{\Delta_{21} L}{2} \right) \sin \left(\frac{\Delta_{31} L}{2} \right) \quad (1.10)$$

294 where

$$J = \cos \theta_{13} \sin 2\theta_{13} \sin 2\theta_{12} \sin 2\theta_{23} \quad (1.11)$$

295 is the Jarlskog invariant [75], L the neutrino baseline, i.e. the distance between
 296 the neutrino production and detection points, and Δ_{ab} a factor proportional to the
 297 sign and magnitude of the mass splitting. From these equations, it is clear how the
 298 relative large value of θ_{13} is a happy accident necessary not to completely suppress the
 299 sensitivity to CP violation. The equations also show how the sensitivity to δ is tied

300 to the measurement of the least precisely measured mixing angle, θ_{23} (via the $\sin 2\theta_{23}$
301 term) and to an other unknown quantity, the neutrino “mass hierarchy” (via the Δ_{ab}
302 terms). The precise determination of θ_{23} is often referred as to “the octant problem”.
303 Current experimental results [2, 11] are consistent with $\theta_{23} = 45^\circ$, which would imply
304 maximal mixing between $\nu_\mu - \nu_\tau$, hinting to an intriguing new symmetry. Therefore,
305 a precise measurement of θ_{23} is of great interest for theoretical models of quark-lepton
306 universality [69, 86, 98], whose quark and lepton mixing matrices are proportional to
307 the deviation of θ_{23} from 45° .

308 **Neutrino mass hierarchy.** The “mass hierarchy” problem refers to the unknown
309 ordering of the value of absolute mass of the neutrino mass eigenstates. Current
310 oscillation experiments are sensitive only to the magnitude of the mass splitting, and
311 not directly to its sign. In a framework where the lightest neutrino mass (arbitrarily)
312 corresponds to the first eigenstate m_1 , it is unknown whether $m_2 - m_1 < m_3 - m_1$
313 (Normal Hierarchy) or $m_2 - m_1 > m_3 - m_1$ (Inverted Hierarchy). The mass hierarchy
314 affects not only the sensitivity to CP violation searches in long baseline oscillation
315 experiments, but also the sensitivity to determine whether neutrinos are Majorana
316 particles in neutrinoless double beta decay experiments.

317 **Majorana or Dirac?** Evidence of neutrino oscillations demands the introduction
318 of a mechanism which can give mass to the neutrinos. This mechanism should possibly
319 also explain why neutrino masses are at least six orders of magnitude lower than the
320 electron mass (the second lightest SM fermion). In a description of neutrinos as Dirac
321 4-component spinors, the neutrino field acquires mass via the Higgs mechanism as
322 any other fermion of the SM. In this case, the neutrino mass is given by $m_a = \frac{y_a^\nu v}{\sqrt{2}}$,
323 where v is the Higgs VEV and y_a^ν is the Yukawa coupling between the Higgs and the
324 neutrino. The smallness of neutrino masses can only be pinned on a tiny Yukawa
325 coupling which is not justified by the theory.

326 In 1937, Majorana demonstrated that the introduction of a two components spinor is

327 sufficient to describe a massive fermion [85]. The Dirac equations of motion for the
 328 chiral fields (equations 1.5 and 1.6) hold true in the case of two components spinor
 329 under the assumption that the chiral components ψ_R and ψ_L are correlated through
 330 the charge conjugation matrix \mathcal{C} , $\psi_R = \mathcal{C}\bar{\psi}_L$. Therefore the theory is applicable only
 331 to neutral fermions. Neutrinos are the only neutral elementary particles in the SM
 332 – the only possible Majorana particle candidate. This theory constructs a neutrino
 333 Majorana mass term \mathcal{L}_5 of the following form in the Higgs unitary gauge

$$\mathcal{L}_5 = \frac{1}{2} \frac{gv^2}{\mathcal{M}} \nu_L^T \mathcal{C}^\dagger \nu_L, \quad (1.12)$$

334 where g is the coupling coefficient, v the Higgs VEV and \mathcal{M} a constant with the
 335 dimension of the mass proportional to the scale of new physics. The \mathcal{L}_5 term would
 336 introduce a non-renormalizable term in the lagrangian, since it has dimensions of
 337 energy to the fifth power. This is not allowed in the SM lagrangian; however, the
 338 existence of such terms is plausible if we consider the SM as an effective theory
 339 at low energy, manifestation of the symmetry breaking of a more general theory at
 340 higher energy, e.g. a Grand Unified Theory (GUT), and not the definitive theory.
 341 The mass term in eq 1.12 implies the neutrino mass to be $m = \frac{gv^2}{\mathcal{M}}$. The coupling
 342 coefficient can be of the order of any other fermion's coupling coefficient, since the
 343 smallness of neutrino masses is achieved by the big value of the new physics mass
 344 scale alone. This vanilla formulation is the conceptual basis for many flavors of *see-*
 345 *saw mechanism* [113], which we will not discuss here in any detail. However, it is
 346 fascinating how the puzzle of the neutrino mass hints to the existence of a deeper and
 347 more complete theory.

348 From a kinematic point of view, Dirac and Majorana neutrinos satisfy the same
 349 energy-momentum dispersion relationship. Thus, it is impossible to discern the neu-
 350 trino nature through kinematic effects such as neutrino oscillations. Neutrinoless

351 double beta decay searches are the most promising way to understand the nature of
352 the neutrino and are therefore subject of great theoretical and experimental interest.
353 Observation of the lepton number violating process $0\nu\beta\beta$ would imply neutrinos have
354 a Majorana component. Depending on the mass hierarchy, the theory also predicts
355 $0\nu\beta\beta$ exclusion regions and confirmation of the sole Dirac component for neutrinos
356 [39].

357

358 1.3.2 Towards a more fundamental theory: GUTs

359 Despite its highly predictive power, a number of conceptual issues arise in the SM
360 which disfavor it to be a good candidate for a fundamental theory.

361 The SM does not include a suitable dark matter candidate and a mechanisms
362 that accounts for the baryon asymmetry of the universe. Additionally, up to a total
363 of 25 parameters remain seemingly arbitrary and need to be fitted to data: 3 gauge
364 couplings, 9 charged fermion masses, 3 mixing angles and one CP phase in the CKM
365 matrix, the Higgs mass and quartic coupling, θ_{QCD} , 3 neutrino mixing angles, 1 Dirac
366 phase and, eventually, 2 Majorana phases.

367 From a group theory perspective, the SM has a rather complex group structure,
368 where a gauge group is formed with the direct product of other three groups as shown
369 in eq. 1.1. Drawing a parallel with the electroweak symmetry breaking mechanism,
370 where the $SU(2)_T \otimes U(1)_Y$ is recovered from $U(1)_{EM}$, an interesting line of simplification
371 for the SM group structure would be to devise a similar mechanism where
372 $SU(3)_C \otimes SU(2)_T \otimes U(1)_Y$ is recovered from an hypothetical larger group. IS THIS
373 CORRECT? Just as the electroweak unification becomes evident at energies higher
374 than the Higgs VEV, a direct manifestation of Grand Unification Theories (GUTs)
375 would occur at even higher energies.

376 As the smallness of neutrino masses suggests the existence of a higher mass scale,

377 an other, even stronger, hint to Grand Unification comes from the slope of running
 378 of the coupling constants. The coupling constants for the electromagnetic, weak and
 379 strong interactions in the SM vary as a function of the interaction energy as shown
 380 in figure 1.2; they do not exactly meet under the current experimental constraints,
 381 but their trend is interesting enough to push for the construction of theories where
 382 perfect unification is achieved through the addition of new particles.

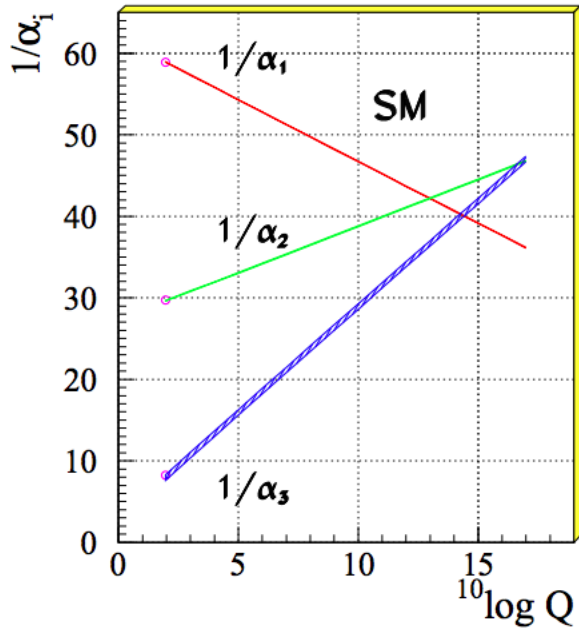


Figure 1.2: Evolution of the inverse of the three coupling constants in the Standard Model as a function of the momentum transferred, [79].

SU(5). The smallest simple group containing $SU(3)_C \otimes SU(2)_T \otimes U(1)_Y$ is SU(5), as shown first by Georgi and Glashow in [63]. Quarks and leptons in this group fit the $\bar{5}$ and 10 representations. The representation for left-handed fermions are the following

$$\bar{5} = (\nu_e, e^-)_L + \bar{d}_L \quad (1.13)$$

$$10 = e_L^+ + \bar{u}_L + (u, d)_L, \quad (1.14)$$

383 while the boson structure gains a new couple of super heavy bosons (X,Y)

$$24 = \underbrace{(8, 1)}_{\text{gluons}} + \underbrace{(1, 3) + (1, 1)}_{W^\pm, Z, \gamma} + \underbrace{(3, 2) + (\bar{3}, 2)}_{X, Y \text{ bosons}}. \quad (1.15)$$

384 Nice features such as charge quantization and the identity between the positron
385 and proton charge value come directly from the group structure. The new super
386 heavy bosons are colored and form a weak doublet. Their are the mediator of the
387 interaction that turns quarks into leptons, leading to predict the existence of processes
388 that violate baryon number, such as $p \rightarrow \pi^0 + e^+$ (see fig 1.8, right). The prediction
389 for proton decay lifetime, $\tau_p \sim \frac{M_X^4}{m_p^5} \sim 10^{30 \pm 1.5}$ years, is unfortunately experimentally
390 disproved by IMB and Super-Kamiokande [3, 26].

391 **SO(10).** More complicated group structures, such as SO(10) are still viable
392 candidates for GUT. SO(10) includes the same type of X and Y bosons as SU(5).
393 Right-handed massive neutrinos are embedded in the construction of the irreducible
394 representation of SO(10). Different patterns of SO(10) symmetry breaking to recover
395 the SM are possible and lead to different predictions for the proton decay lifetime;
396 some of these predictions are not excluded by the experiments [80].

397 **SUSY GUTs.** Supersymmetry theories allow for another family of GUTs. In
398 SUSY, every fundamental particle in the SM has a “superpartner”, identical in each
399 quantum number except for the spin-statistics: the fermion supersymmetric partners
400 are bosons and vice versa. Collider experiments (mainly LHC) constrain the mass of
401 the supersymmetric partners to be very heavy [?]. The SU(5), SU(10) groups with
402 a SUSY twist are the basic groups for SUSY GUTs. From the phenomenology point
403 of view, SUSY models tend to push the proton decay life time higher by a factor of
404 four, they solve the “hierarchy problem”, and they also predict new channels for the
405 proton decay. In particular they predict the presence of kaons in the final product,
406 with a dominant mode of $p \rightarrow K^+ \bar{\nu}$. Predictions on the proton decay lifetime depend

407 on the chosen SUSY model; again, some of the predictions are not excluded by the
408 experiments [83, 84, 102].

409 **1.4 Motivations for Hadronic Cross Sections in Ar-** 410 **gon**

411 Critical challenges await the next decade of high energy physics at the intensity
412 frontier. Following the recommendation of the latest Particle Physics Project Priori-
413 tization Panel [99], the US is dedicating substantial resources to the development of
414 a short- and long- baseline neutrino program to address many of open questions in
415 neutrino physics today. This program pivots on the Liquid Argon Time Projection
416 Chamber (LArTPC) detector technology which will be described in Chapter 2.

417 The main goals of these research programs include:

- 418 - the assessment of the existence of right-handed sterile neutrinos via the study
419 of accelerator neutrinos on a short baseline (SBN),
- 420 - the determination of the sign of Δm_{13}^2 (or Δm_{23}^2), i.e., the neutrino mass hier-
421 archy via the study of accelerator neutrinos on a long baseline (DUNE),
- 422 - the determination of the octant, i.e. whether θ_{23} is maximal, via the study of
423 accelerator neutrinos on a long baseline (DUNE),
- 424 - the determination the status of CP symmetry in the lepton sector, via the study
425 of accelerator neutrinos on a long baseline (DUNE),
- 426 - the search for observables predicted by GUTs, such as proton decay via the
427 study of non accelerator physics in massive underground detectors (DUNE).

428 **1.4.1 Pion-Argon Total Hadronic Cross Section**

429 This section outlines the importance of the pion-argon total hadronic cross section in
430 the context of the current and upcoming liquid argon neutrino experiments, SBN and
431 DUNE. We describe the signal signature and historic measurements of pion-nucleus
432 cross section, as well as the implementation of this cross sections in the current version
433 of the simulation package used by LArIAT.

434 **π^- -Ar Cross Section in the Context of Neutrino Searches**

435 As outlined in 1.2.3, neutrino experiments use the products of neutrino interactions
436 to identify the energy and flavor of the incoming neutrino. Pions are a common
437 product of neutrino interaction, especially in resonant scattering, DIS and coherent
438 pion production. For neutrino experiments in argon, there are two main reasons
439 why understanding pion hadronic interactions with argon is important: to model
440 the behavior of the pion inside the nucleus struck by the neutrino and to model the
441 behavior of the pion during its propagation inside the detector medium.

442 Assumptions on the nuclear models and on the interaction of hadrons inside the
443 nucleus performed at the level of the neutrino event generator bridge the measure-
444 ment of the products of a neutrino interaction to the reconstruction of the neutrino
445 energy and flavor. Thus, understanding pion hadronic interactions with the nucleus
446 is particularly important to model correctly resonant, DIS and coherent pion produc-
447 tion in neutrino interactions, where the presence of pions in the nucleus is abundant.
448 For example, in case of resonant scattering,

$$\nu_l + N \rightarrow l + \Delta/N^* \rightarrow l + \pi + N', \quad (1.16)$$

449 the Δ and N^* and excited states will decay hadronically in matters of $\sim 10^{-24}$ s inside
450 the nucleus producing pions which will bounce within the nuclear medium. The decay

451 modes for the lower mass Δ (1232) and $N^*(1440)$ are listed in table 1.3.

452 The key elements of a neutrino event generators for resonance and DIS events are
453 the nuclear model and the hadron treatment (both production and transportation).
454 We illustrate here the conceptual basis of the GENIE Neutrino Generator [17] as
455 an example, since GENIE is one the most popular event generators for liquid argon
456 experiments. For example, the nuclear model used by GENIE for all processes is
457 a relativistic Fermi gas (RFG) modified to incorporate short range nucleon-nucleon
458 correlations [28]. This means that the initial momentum and binding energy of the
459 struck nucleon is determined by assuming nucleons inside the nucleus are quasi-free,
460 acting independently in the mean field of the nucleus. For $A > 20$ like argon, the
461 2-parameter Woods-Saxon shell model for density function is used. The GENIE mod-
462 ule INTRANUKE [78] is used to simulate the final-state interactions (FSI) which is
463 the hadron re-interaction inside the nucleus. This module places the outgoing parti-
464 cles in the nucleus and propagates them using the “hA model”. In the INTRANUKE
465 hA model, hadrons can undergo at most one FSI per event. When possible, exter-
466 nal hadron-nucleus scattering data are used to tune INTRANUKE. Since no data is
467 available for Argon, GENIE uses an interpolation of data from heavier and lighter nu-
468 clei for the pion-argon cross section leading to big uncertainties in the INTRANUKE
469 module.

470 Once the pion has left the target nucleus, the pion-argon hadronic cross section
471 plays an important role in the pion transportation inside the argon medium: processes
472 like pion absorption with emission of nucleons or pion charge exchange can greatly
473 modify the topology of a neutrino interactions in the detector and lead to errors in the
474 event classification. Being able to reconstruct the details of pions inside the detector
475 is an imperative for modern liquid argon neutrino experiment to achieve the design
476 resolution for their key physics measurements.

477 **π^- -Ar Hadronic Interaction: Signal Signatures**

478 Strong hadronic interaction models [44, 64] predict the pion interaction processes with
479 argon in the [100 - 1200] MeV energy range. The total hadronic π^- -Ar interaction
480 cross section is defined as the one related to the single process driven only by the
481 strong interaction which is dominant in the considered energy range. In measuring
482 the “total” cross section, we include both the elastic and reaction channels, regardless
483 of the final state,

$$\sigma_{Tot} = \sigma_{Elastic} + \sigma_{Reaction}; \quad (1.17)$$

484 the reaction channel is further characterized by several exclusive channels with defined
485 topologies,

$$\sigma_{Reaction} = \sigma_{Inelastic} + \sigma_{abs} + \sigma_{chex} + \sigma_{\pi prod}. \quad (1.18)$$

486 A summary of the pion final states in order of pion multiplicity for the reaction
487 channel is given in table 1.4. Pion capture and pion decay at rest dominate the
488 cross section under 100 MeV. We define pion capture as the process determining the
489 formation of a pionic atom and the subsequent pion’s end of life. Stopping negative
490 pions can form pionic argon, where the negative pion plays the role of an orbital
491 electron. Since the pion mass is two orders of magnitude greater than the electron
492 mass, the spatial wave form of the pion will overlap more with the nucleus compared
493 to the electron case. After the electromagnetic formation of the pionic atom, the
494 pion will be quickly absorbed by the nucleus, which is put in an excited state. The
495 nucleus then de-excites with the emission of low energy nucleons and photons. Pion
496 capture is predominant compared to pion decay, the other important process for very
497 low energy pions. The decay of a pion is governed by the weak force; the pion decay
498 life time is $\tau_\pi = 2.6 \times 10^{-8}$ s and the main decay mode is $\pi^- \rightarrow \mu^- + \bar{\nu}_\mu$ (BR 99.98%).
499 Since pion capture can be considered an electromagnetic process and pion decay is a
500 weak process, this energy region is purposely excluded from the hadronic cross section

501 measurement.

502 **Previous measurements: Lighter and Heavier Nuclei**

503 Many experiments with pion beams have studied the hadronic interaction of pions on
504 light and heavy materials, such as He, Li, C, Fe, Pb [32]. However, data on argon are
505 rare: the total differential hadronic cross section has never been measured before on
506 argon. Simulation packages like Geant4 base their pion transportation for argon on
507 data from lighter and heavier nuclei: the goal of LArIAT’s dedicated measurement on
508 argon is to bridge this gap in data, thus reducing the uncertainties related to pions
509 interaction in argon in both neutrino event generators and in simulation packages of
510 pion transportation.

511 The shape of the pion-nucleus interaction cross section in the energy range con-
512 sidered shows the distinct features indicating the presence of a resonance. In fact, the
513 mean free path of a pion of kinetic energy between 100 and 400 MeV is much shorter
514 than the average distance between nucleons (which is of the order of 1 fm). There-
515 fore, the pion interacts with surface nucleons. A Δ resonance is often produced in
516 the interaction, which subsequently decays inside the nucleus. Experimental results
517 on several nuclei as reported in [32] are shown in Figure 1.3; it is interesting to notice
518 here how the shape of the Δ resonance becomes less pronounced as a function of the
519 mass number of the target nucleus. Pion interactions with heavier nuclei also shift the
520 peak of the resonance at lower energy; this effect is due to kinematic considerations
521 and to the difference in propagation of the Δ inside the nucleus. Multiple scattering
522 effect modify the resonance width, which is larger than the natural-decay width. As
523 an example of a fairly well studied target, Figure 1.4 reports the negative pion cross
524 section on Carbon for the elastic and reaction² channels, and their sum [50].

2. This paper calls “inelastic interaction” what we refer as to “reaction channel”.

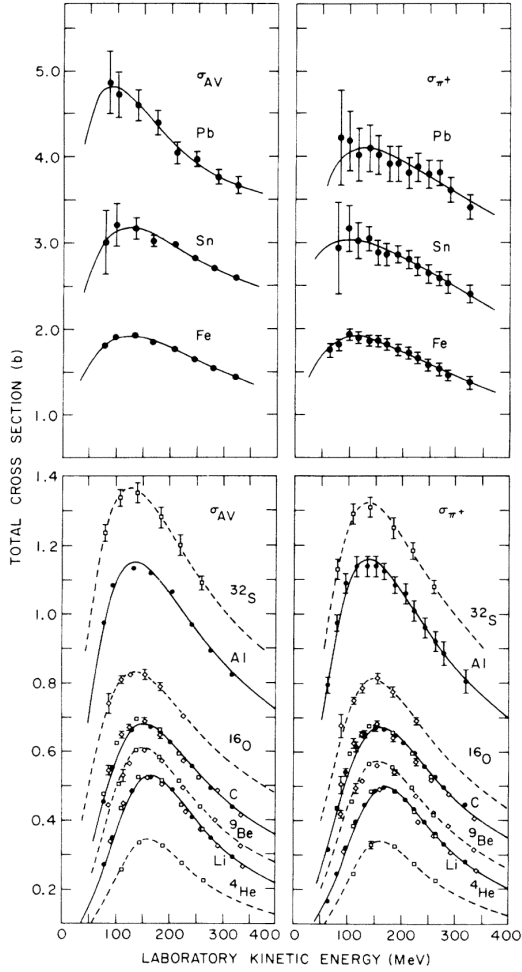


Figure 1.3: Pion-nucleus total cross sections: σ_{π^+} for positive pions (right) and σ_{AV} (left) for the average between positive and negative pions $\sigma_{AV} = \frac{\sigma_{\pi^+} + \sigma_{\pi^-}}{2}$ in the Δ resonance region. The error bars include estimates of systematic uncertainties. The curves are the results of fits to the data assuming a Breit-Wigner shape. This summary plot is reported in [32] and uses data from [47, 109].

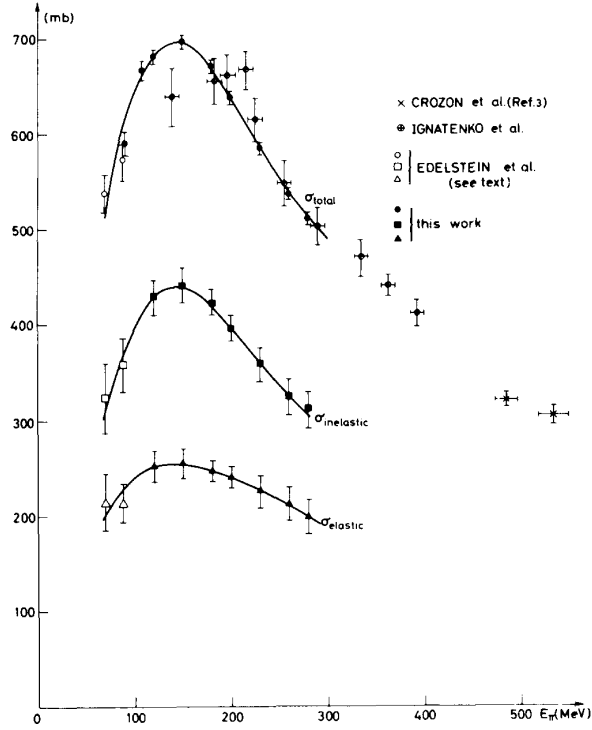


Figure 1.4: Negative pion nucleus total, elastic and reaction cross sections on ^{12}C as from [50].

525 Negative Pion Interaction Cross Section in Simulation Packages

526 LArIAT uses Geant4 as the default simulation package. In particular, pions (and
 527 kaons) transportation is achieved through the Geant4 FTFP_BERT physics list. In
 528 this physics list, Geant4 uses the Bertini cascade model [110] to simulate the products
 529 of the pion-nucleus interaction as well as the secondary hadrons re-interactions inside
 530 the target nucleus (intra-nuclear cascade). The target nucleus is represented as a
 531 continuous gas where the nuclear potential follows concentrical shells whose depths
 532 approximate the Woods-Saxon shape. The CERN-HERA compilations [106, 107] of
 533 hadron-nucleon interaction data is the data base used for the decision making process
 534 after the cascade is invoked. The cross section model determines if the pion inter-
 535 acts, the eventual type of interaction and the interaction multiplicity. For hadron
 536 projectiles with energy less than 20 GeV, Geant4 reports the uncertainty on the cross

537 section model to be about the size of the error bars on the data used, or about 10%,
538 increasing to 20-30% in energy regions where data is sparse.

539 The relevance of the GENIE generator for neutrino physics and its basic working
540 principles have been outlined earlier in this section. Given GENIE’s modularity,
541 information on hadron-nucleus interactions can be extracted from the INTRANUKE
542 module and directly compared against the Geant4 predictions. The work in [91]
543 reviews the current status of negative and positive pion simulation in Geant4 and
544 GENIE for ^{12}C , ^{56}Fe , and ^{40}Ca . From that work, we report the results for ^{12}C
545 in Figure 1.5 as it allows a direct comparison between Geant4, GENIE and data.
546 Geant4 predictions for π^- on Carbon are in good agreement with data over all the
547 spectrum, while GENIE predictions seem to show some features at around 500 MeV
548 and 900 MeV, maybe due to higher resonances in the hA model. From the same
549 work, we also report the negative pion cross section on ^{40}Ca in Figure 1.6, since this
550 is the nuclear medium closest argon with some available data. The predictions from
551 both Geant4 and GENIE agree with data in the high energy region; the Geant4 and
552 GENIE predictions diverge in the resonance region, where data is not available. These
553 few examples highlight how cross section data for the specific nucleus considered in
554 the neutrino experiments is fundamental to inform the Monte Carlo simulation.

555 For the LArIAT simulation of the MC sample used in the π^- argon total hadronic
556 cross section measurement we use the Geant4 Bertini Cascade model, whose predic-
557 tions for the total, elastic and reaction hadronic cross sections are show in Figure
558 1.7.

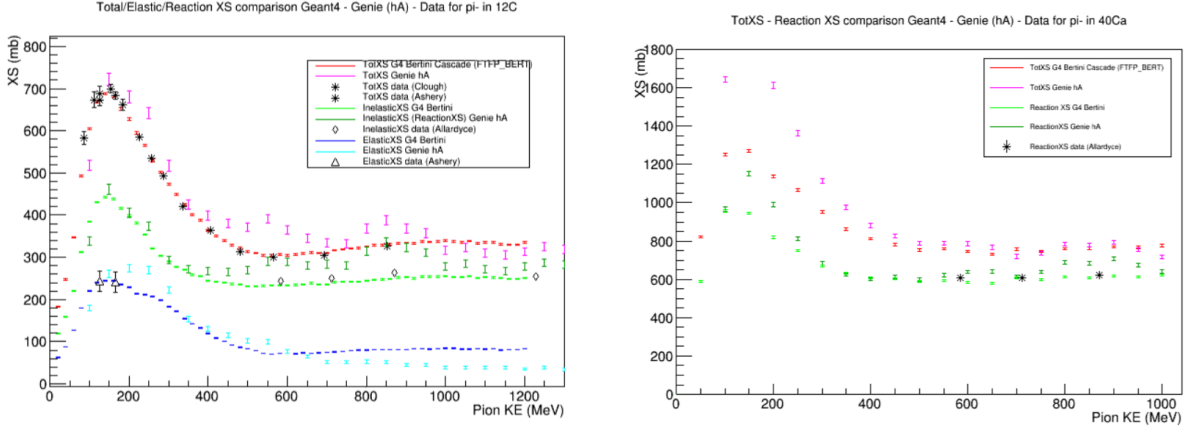


Figure 1.5: Total, elastic and reaction cross section for π^- on ^{12}C . Comparison between results from Geant4 simulation (Bertini cascade model), Genie simulation (hA model), and experimental data [20, 47, 48, 101].

Figure 1.6: Total, elastic and reaction cross section for π^- on ^{40}Ca . Comparison between results from Geant4 simulation (Bertini cascade model), Genie simulation (hA model), and experimental data [48].

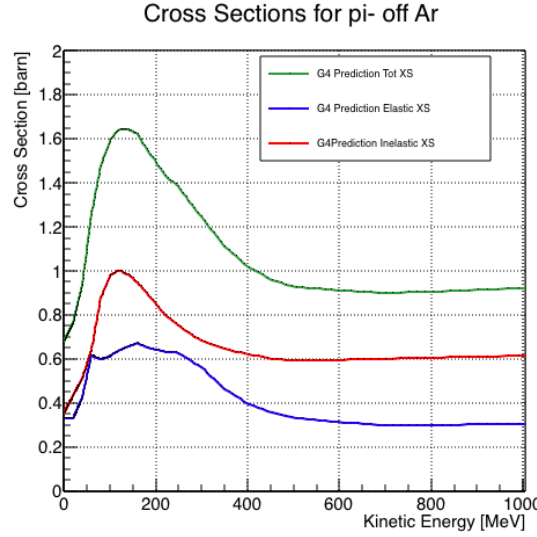


Figure 1.7: Total, elastic and reaction hadronic cross section for π^- -argon implemented in Geant4 10.01.p3.

Resonance	Decay Mode	Lifetime (s)
Δ (1232) $3/2^+$	$\Delta^{++}(\text{uuu}) \rightarrow p\pi^+$ $\Delta^+(\text{uud}) \rightarrow n\pi^+$ $\Delta^+(\text{uud}) \rightarrow p\pi^0$ $\Delta^0(\text{udd}) \rightarrow n\pi^0$ $\Delta^0(\text{udd}) \rightarrow p\pi^-$ $\Delta^-(\text{ddd}) \rightarrow n\pi^-$	$\sim 5.6 \times 10^{-24}$
N^* (1440) $1/2^+$	$N^* \rightarrow N\pi$ $N^* \rightarrow N\pi\pi$	$\sim 2.2 \times 10^{-24}$

Table 1.3: Main decay modes of the lightest Delta resonance and Nucleon excited state.

N π in FS	Channel Name	Reaction	Notes
0	Pion Absorption, σ_{abs}	$\pi^-(np) \rightarrow nn$ (2-body abs) $\pi^-(nnp) \rightarrow nnn$ (3-body abs) $\pi^-(npp) \rightarrow pnn$ (3-body abs) $\pi^-(nnpp) \rightarrow pmn$ (Multi-body abs)	Suppressed on single nucleon by energy conservation: the process occurs on at least two nucleons system.
1	Elastic Scattering, σ_{el}	$\pi^- + N \rightarrow \pi^- + N$	Scattering on nucleon or nucleus, the target is left in ground state
1	Charge Exchange, σ_{chea}	$\pi^- + p \rightarrow \Delta^0 \rightarrow \pi^0 + n$ $\pi^- + N \rightarrow \pi^+ + \text{nucleons}$	Single charge exchange: charged pion converts into neutral pion Double charge exchange: charged pion converts into opposite charge pion
1	Inelastic Scattering, σ_{inel}	$\pi^- + p \rightarrow \Delta^0 \rightarrow \pi^- + p$ (knock-out) $\pi^- + n \rightarrow \Delta^- \rightarrow \pi^- + n$ (knock-out)	Other possible reactions: Pure Inelastic scattering: population of low energy bound excited states Nuclear break-up with nucleons or fragments knock-out
2+	Pion Production, $\sigma_{\pi prod}$	$\pi^- + N \rightarrow \geq 2\pi + \text{nucleons}$	Possible if pion K.E ≥ 500 MeV/c

Table 1.4: Summary of negative pion hadronic interactions of the reaction channel as a function of the pion multiplicity in the final state in the energy range [100-1200] MeV.

559 **1.4.2 Kaon-Argon Total Hadronic Cross Section**

560 This section outlines the importance of the kaon-argon total hadronic cross section.
561 We start by discussing the measurement in the context of nucleon decay searches. We
562 then describe the signal signature and historical measurements of kaon-nucleus cross
563 section, as well as the implementation of this cross sections in the current version of
564 the simulation package used by LArIAT.

565 **K⁺Ar Cross section in the Context of Nucleon Decay Searches**

566 Baryon number is accidentally conserved in the Standard Model. Even though no
567 baryon number violation has been experimentally observed thus far, no underlying
568 symmetry in line with the Noether paradigm [90] explains its conservation. As shown
569 in section 1.3.2, almost all Grand Unified Theories predict at some level baryon num-
570 ber violation in the form of nucleon decay on long time-scales. Given the impossibil-
571 ity to reach grand unification energy scales with collider experiments (Energy Scale
572 $> 10^{15}$ GeV), an indirect proof of GUTs is needed. The experimental observation of
573 nucleon decay may be the only viable way to explore these theories.

574 In case of nucleon decay discovery, the dominant decay mode may uncover addi-
575 tional information about the GUT type. Supersymmetric GUTs [22, 41] prefer the
576 presence of kaons in the products of the decay, e.g. $p \rightarrow K^+ \bar{\nu}$ (see fig 1.8, left).
577 Gauge mediated GUTs, in which new gauge bosons are introduced that allow for the
578 transformation of quarks into leptons, and vice versa, prefer the mode $p \rightarrow e^+ \pi^0$ (see
579 fig 1.8, right).

580 LArIAT tiny active volume makes it impossible for the experiment to place com-
581 petitive limits on nucleon decay searches. However, LArIAT provides excellent data
582 to characterize kaons in liquid argon for the ‘‘LAr golden mode’’, $p \rightarrow K^+ \bar{\nu}$. The
583 result of these studies will affect future proton decay searches in LArTPCs. Previous
584 work has been done to assess the potential identification efficiency for different decay

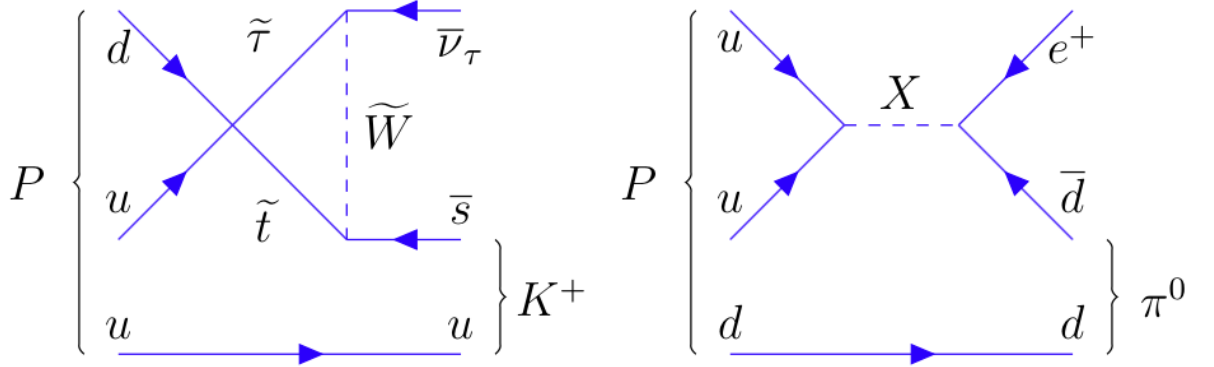


Figure 1.8: Feynman diagrams for proton decay “golden modes”: $p \rightarrow K^+\bar{\nu}$ for supersymmetric GUTs on the left and $p \rightarrow e^+\pi^0$ for gauge-mediated GUTs on the right.

585 modes in a LArTPC [46], but, as the time of this writing, no study of kaon selection
 586 efficiency in LArTPCs has been performed on data. The K^+ -Ar interaction cross
 587 section has never been measured before and can affect the possibility of detecting
 588 and measuring kaons when produced in a proton decay event. Kaon interactions with
 589 argon can distort the kaon energy spectrum as well as change the topology of single
 590 kaon events. In a LArTPC, non-interacting kaons appear as straight tracks with a
 591 high ionization depositions at the end (Bragg peak). The topology of interacting
 592 kaons can be quite different. In case of elastic scattering, a distinct kink will be
 593 present in the track. In case of inelastic scattering the Bragg peak will not be present
 594 and additional tracks will populate the event. Performing the total hadronic K^+ -Ar
 595 cross section measurement on data serves the double purpose of identifying the rate
 596 of “unusual” topologies (kinks and additional tracks) and of developing tools for kaon
 597 tracking in LAr.

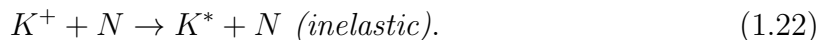
598 **K^+ Ar Hadronic Interaction: Signal Signatures**

The interaction of a mildly relativistic charged kaon with an argon nucleus is determined largely by the strong force. The total hadronic K^+ -Ar interaction cross section

is defined as the one related to the single (hadronic) process driven only by the strong interaction. In this case, “total” indicates all strong interactions regardless of the final state. This condition purposefully includes both elastic and inelastic (reaction) channels. Indeed, the total cross section section can be then decomposed into

$$\sigma_{Tot} = \sigma_{Elastic} + \sigma_{Reaction}.$$

599 For the LArIAT cross section analysis, the kaons considered span a momentum
 600 inside the TPC from 100 MeV/c to 800 MeV/c. In this energy range, the relevant
 601 K-Nucleon interactions are according to [58]:



602 **Previous Measurements: Lighter and Heavier Nuclei**

603 In general, measurements on kaon cross sections are extremely scarce. The mea-
 604 surement of the kaon interaction cross section would bring the additional benefit
 605 of reducing the uncertainties associated with hadron interaction models adopted in
 606 MC simulations for argon targets, beneficial for both proton decay studies and kaon
 607 production from neutrino interaction studies, where the uncertainties for final state
 608 interaction models are big [42].

609 Figure 1.9 shows a 1997 measurement on several elements as performed by Fried-
 610 mann et al. [60]. As a reference, this paper measures a σ_{Tot} for Si of 366.5 ± 4.8
 611 mb and a σ_{Tot} for Ca of 494.6 ± 7.7 mb at 488 MeV/c. The cross section for argon

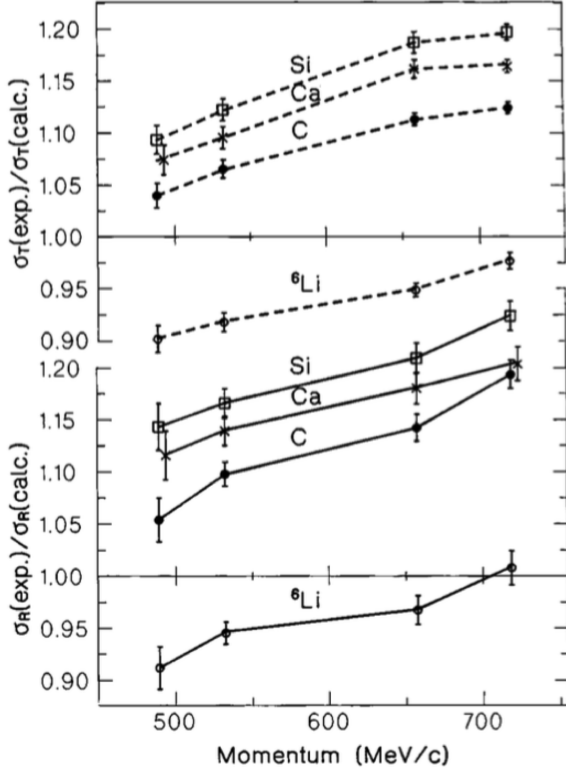


Figure 1.9: Ratios between experimental and calculated cross sections as from [60].
Top: Total cross sections.
Bottom: reaction cross sections.

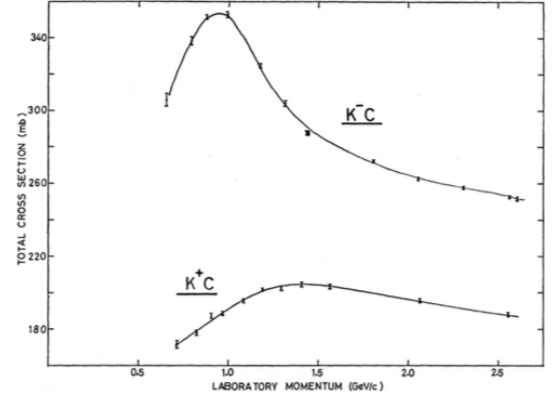


Figure 1.10: Total K^+ and K^- cross sections on carbon as from [30].

is expected to lie in between these two measurements. Additional data on the kaon cross section are provided by Bugg et al. [30]. Bugg performs a measurement of the total K^+ and K^- cross sections on protons and deuterons over the range of 0.6-2.65 GeV/c, as well as a measurement of the total K^+ and K^- cross sections on carbon for a number of momenta; the results of this paper on carbon are reported in Figure 1.10.

618 **Kaon Interaction Cross Section for thin target in Geant4**

619 Since the kaon cross section in argon has never been measured before, simulation
620 packages tune kaon transportation in argon by extrapolation from lighter and heavier
621 nuclei. LArIAT uses the Geant4 suite for particle transportation. Since kaon data on

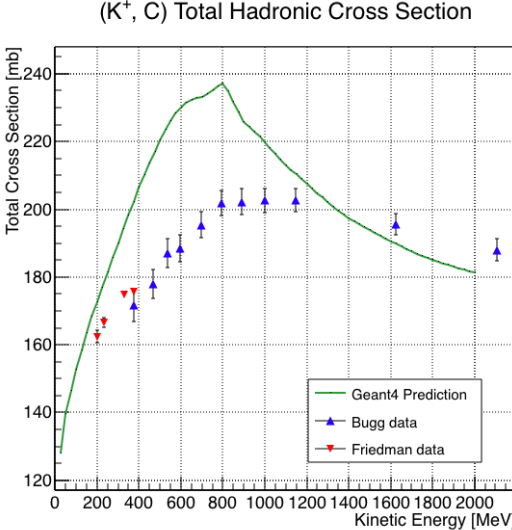


Figure 1.11: Total hadronic cross section for carbon implemented in Geant4 10.01.p3 with overlaid with the Bugg and Friedman data.

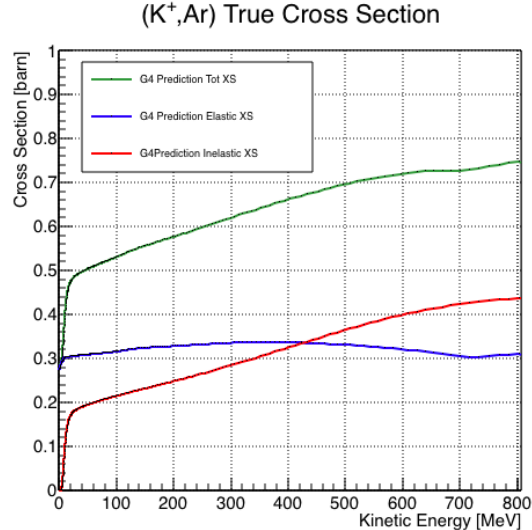


Figure 1.12: Total, elastic and reaction hadronic cross section for K^+ -argon implemented in Geant4 10.01.p3.

carbon are available, we used it as a metric to evaluate the Geant4 prediction performances. Figure 1.11 shows the total hadronic cross section for carbon implemented in Geant4 10.01.p3 overlaid with the Bugg and Friedman data. Unfortunately, the current version of Geant4 does not reproduce the data for carbon closely. On one hand, this evidence makes us even more wary when using the Monte Carlo in simulating the kaon-argon interactions. On the other, it further highlights the importance of the kaon measurement. For the LArIAT simulation of the MC sample used in the K^+ -argon total hadronic cross section measurement we use the Geant4 Bertini Cascade model, whose predictions for the total, elastic and reaction hadronic cross sections are show in Figure 1.12.

632 Chapter 2

633 **Liquid Argon Detectors at the** 634 **Intensity Frontier**

635 In the next few years, LArTPCs will be the tools to answer some of the burning
636 questions in neutrino physics today. This section illustrates the operational principles
637 of this detector technology, as well as the scope of the key detectors in the US liquid
638 argon program – SBN, DUNE and LArIAT.

639 **2.1 The Liquid Argon Time Projection Chamber** 640 **Technology**

641 **2.1.1 TPCs, Neutrinos & Argon**

642 David Nygren designed the first Time Projection Chamber (TPC) in the late 1970s [92]
643 for the PEP-4 experiment, a detector apt to study electron-positron collisions at the
644 PEP storage ring at the SLAC National Accelerator Laboratory. From the original
645 design in the seventies – a cylindrical chamber filled with methane gas – the TPC
646 detector concept has seen many incarnations, the employment of several different
647 active media and a variety of different particle physics applications, including, but

648 not limited to the study of electron/positron storage rings (e.g. PEP4, TOPAZ,
649 ALEPH and DELPHI), heavy ions collisions in fixed target and collider experiments
650 (e.g. EOS/HISSL and ALICE), dark matter (ArDM), rare decays and capture (e.g.
651 TRIUMF, MuCap), neutrino detectors and nucleon decay (ICARUS, SBN, DUNE),
652 and neutrino less double beta decay (Next). A nice review of the history of TPCs
653 and working principles is provided in [72].

654 Several features of the TPC technology make these detectors a more versatile tool
655 compared to other ionization detectors and explain such a wide popularity. TPCs are
656 the only electronically read detector which deliver simultaneous three-dimensional
657 track information and a measurement of the particle energy loss. Leveraging on both
658 tracking and calorimetry, particle identification (PID) capabilities are enhanced over
659 a wide momentum range.

660 Historically, the active medium in ionization detectors has been in the gaseous
661 form. Carlo Rubbia first proposed the use of a Liquid Argon TPC for a neutrino
662 experiment, ICARUS [100], in 1977. Using nobles elements in the liquid form for
663 neutrino detectors is advantageous for several reasons. The density of liquids is \sim 1000
664 times greater than gases, augmenting the number of targets for neutrino's interaction
665 in the same volume, in a effort to balance the smallness of neutrino cross section. Since
666 the energy loss of charged particle is proportional to the target material density, as
667 shown in the Bethe-Block equation (eq. 2.1), the increased density reflects into a
668 proportionally higher energy loss, enhancing the calorimetry capability of detectors
669 with a liquid active medium. Additionally, the ionization energy of liquids is smaller
670 than gasses by the order of tens of eV. Thus, at the passage of charged particles,
671 liquids generally produce more ionization electrons than gases for the same deposited
672 energy, forcing the particles to deposit more energy in a shorter range. The downside
673 of using noble liquid elements in experiments is that they require expensive cryogenic
674 systems to cool the gas until it transitions to its the liquid form. The properties

Element	LAr	LXe
Atomic Number	18	54
Atomic weight A	40	131
Boiling Point Tb at 1 atm	87.3 K	165.0 K
Density	1.4 g/cm ³	3.0 g/cm ³
Radiation length	14.0 cm	2.8 cm
Moliere Radius	10.0 cm	5.7 cm
Work function	23.6 eV	15.6 eV
Electron Mobility at $E_{field} = 10^4$ V/m	0.047 m ² /Vs	0.22 m ² /Vs
Average dE/dx MIP	2.1 MeV/cm	3.8 MeV/cm
Average Scintillation Light Yield	40000 γ /MeV	42000 γ /MeV
Scintillation λ	128 nm	175 nm

Table 2.1: LAr, LXe summary of properties relevant for neutrino detectors.

of liquid argon in comparison liquid xenon – a popular choice for dark matter and neutrinoless double beta decay detectors – are summarized in table 2.1. Albeit xenon would be more desirable than argon given some superior properties such as lower ionization energy and higher density and light yield, argon relative abundance abates the cost of argon compared to xenon, making argon a more viable choice for the construction of ton (and kilo-ton) scale neutrino detectors.

LArTPCs are some times referred as to “electronic” bubble-chambers, for the similarity in the tracking and energy resolution which is coupled with an electronic readout of the imaging information in LArTPCs. Compared to these historic detectors however, LArTPC bestow tridimensional tracking and a self triggering mechanism provided by the scintillation light in the liquid argon. An event display of a ν_μ CC interaction candidate in the MicroBooNE detector is shown in picture 2.1 to display the level of spatial details these detectors are capable of; the color scale of the image is proportional to the energy deposited, hinting to these calorimetry capabilities of the detectors.



Figure 2.1: Event display of a ν_μ CC interaction candidate in the MicroBooNE detector.

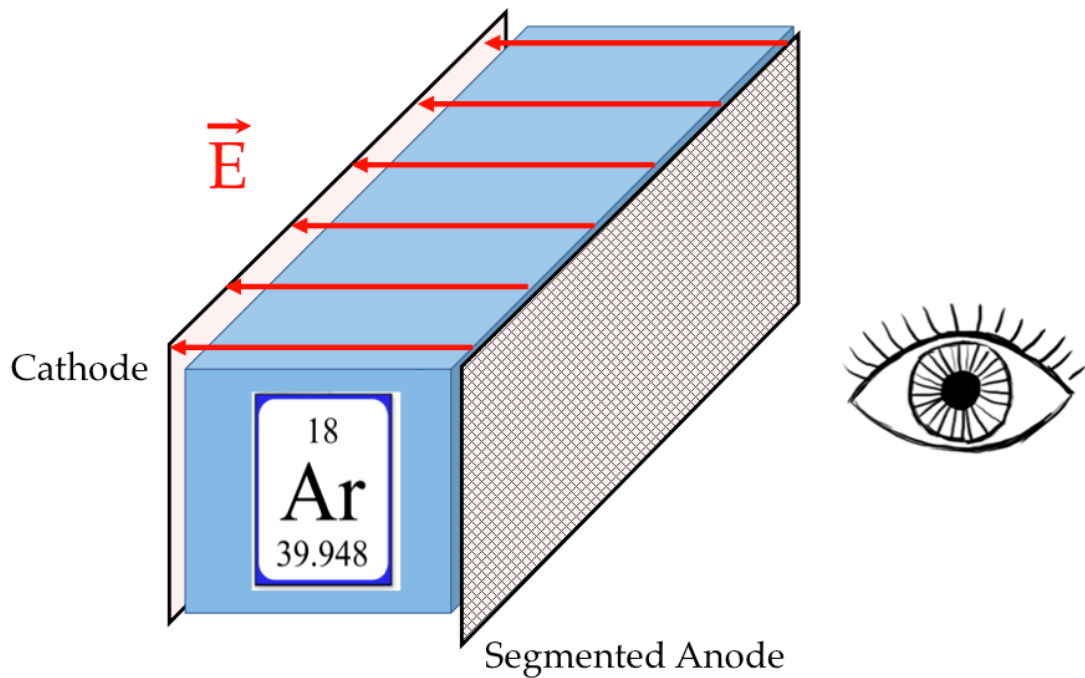


Figure 2.2: A cartoonish sketch of a LArTPC.

690 **2.1.2 LArTPC: Principles of Operation**

691 To the bare bones, a LArTPC is a bulk of liquid argon sandwiched in a flat capacitor,
692 equipped with a light collection system, as the cartoon in 2.2 shows. A uniform
693 electric field of the order of 500 V/cm is maintained constant between the faces of the
694 capacitor. The anode is sensitive to ionization charge and it is usually made of two
695 or more planes segmented into several hundreds parallel sense wires a few millimeters
696 apart; different geometries for the anode segmentation are under study [43].

697 Argon ionization and scintillation are the processes leveraged to detect particles
698 in the LArTPC active volume. When a ionizing radiation traverses the argon active
699 volume it leaves a trail of ionization electrons along its trajectory and it excites
700 the argon producing scintillation light – details on the production and detection of
701 ionization charge and scintillation light are provided in 2.1.4 and 2.1.4 respectively.

702 The optical detector sees the argon scintillation light in matters of nanoseconds.
703 This flash of light determines the start time of an event in the chamber, t_0 . The
704 uniform electric field drifts the ionization electrons from the production point towards
705 the anode in order of hundreds of microseconds or more depending on the chamber
706 dimensions¹. The anode sense wires see either an induced current by the drifting
707 ionization charge (on induction planes) or an injection of such charge (collection
708 plane). An appropriate choice of the voltage bias on each wire plane assures ideal
709 charge transparency, so that all the ionization charge is collected on the collection
710 plane and none on the induction planes.

711 The arrival time of the charge on the anode sense wires is used to measure the
712 position of the original ionizing radiation in the drift direction. In fact, since the
713 constant electric field implies that the drift velocity is also constant, the position of

1. The ionized argon also drifts, but in the opposite directions compared to the electrons. Since the drift time is proportional to the particle mass, the ions' drift time is much longer than the electrons'. Ionized argon is collected on the cathode which is not instrumented, so it is not used to infer information about the interactions in the chamber.

714 the original ionization is simply given by the multiplication of the drift velocity by the
 715 drift time, where the “drift time” is the difference between t_0 and the charge arrival
 716 time on the wire planes. The spacial resolution on this dimension is limited by the
 717 time resolution of the electronics or by longitudinal diffusion of the electrons. The
 718 spatial information on the different wire planes maps a bi-dimensional projection of
 719 the interaction pattern in the plane perpendicular to the drift direction. The spacial
 720 resolution on this dimension is limited by the transverse electron diffusion in argon
 721 and by the grain of the anode segmentation, i.e. the spacing between the wires in
 722 the sense planes [40]. The off-line combination of the 2-D information on the wire
 723 planes with the timing information allows for the 3D reconstruction of the event in
 724 the chamber.

725 Since the charge deposited by the ionizing radiation is proportional to the de-
 726 posited energy and the charge collected on the sense plane is a function of the de-
 727 posited charge, LArTPCs allow the measurement of the energy deposit in the active
 728 volume. Effects due to the presence of free charge and impurities in the active vol-
 729 ume, such as a finite electron lifetime, recombination and space charge, complicate
 730 the relationship between deposited and collected charge affecting the measurement of
 731 the particle’s energy, as described in the next section.

732 **2.1.3 Liquid Argon: Ionization Charge**

733 The mean rate of energy loss by moderately relativistic elementary charge particles
 734 heavier than electrons is well described by the modified Bethe-Bloch [95] equation

$$-\frac{dE}{dx} = K z^2 \frac{Z}{A} \varrho \frac{1}{\beta^2} \left[\frac{1}{2} \ln \frac{2m_e c^2 \beta^2 \gamma^2 T_{max}}{I^2} - \beta^2 - \frac{\delta}{2} \right], \quad (2.1)$$

735 where z is the number of unit charge of the ionizing radiation, Z , A and ϱ are the
 736 atomic number, mass number and density of the medium, m_e is the electron mass,

737 $\gamma = \frac{\beta}{\sqrt{1-\beta^2}}$ is the Lorentz factor of the ionizing radiation, T_{max} is the maximum kinetic
 738 energy which can be imparted to a free electron in a single collision, I is the mean
 739 excitation energy on eV, δ is the density correction and $K = 0.307075 \text{ MeV g}^{-1} \text{ cm}^2$ is
 740 a numerical conversion factor. The Bethe-Bloch treats the energy loss by an ionizing
 741 radiation via quantum-mechanical collisions producing ionization or an excitation in
 742 the medium as an uniform and continuous process. The density correction terms
 743 becomes relevant for incident particle with high energy, where screening effects due
 744 to the polarization of the medium by high energy particles occur.

745 Excitation and ionization of the detector medium occur in similar amounts. Since
 746 the ionizing collisions occur randomly, we can parametrize their number k in a segment
 747 of length s along the track with a Poissonian function

$$P(k) = \frac{s^k}{k! \lambda^k} e^{-s/\lambda}, \quad (2.2)$$

748 where $\lambda = 1/N_e \sigma_i$, with N_e being the electron density of σ_i the ionization cross-
 749 section per electron. About 66% of the ionizing collisions in Argon produce only
 750 a single electron/ion pair [72]; in the other cases, the transferred kinetic energy is
 751 enough for the primary electron to liberate one or more secondary electrons, which
 752 usually stay close to the original pair. Occasionally, electrons can receive enough
 753 energy to be ejected with high energy, forming a so-called “ δ -ray”: a detectable short
 754 track off the particle trajectory, as shown in figure 2.3. The average number of δ -ray
 755 with energy $E > E_0$ per cm follows the empirical form

$$P(E > E_0) \sim \frac{y}{\beta^2 E_0}, \quad (2.3)$$

756 where y is an empirical factor depending on the medium (0.114 for gaseous Ar), and
 757 β is v/c .

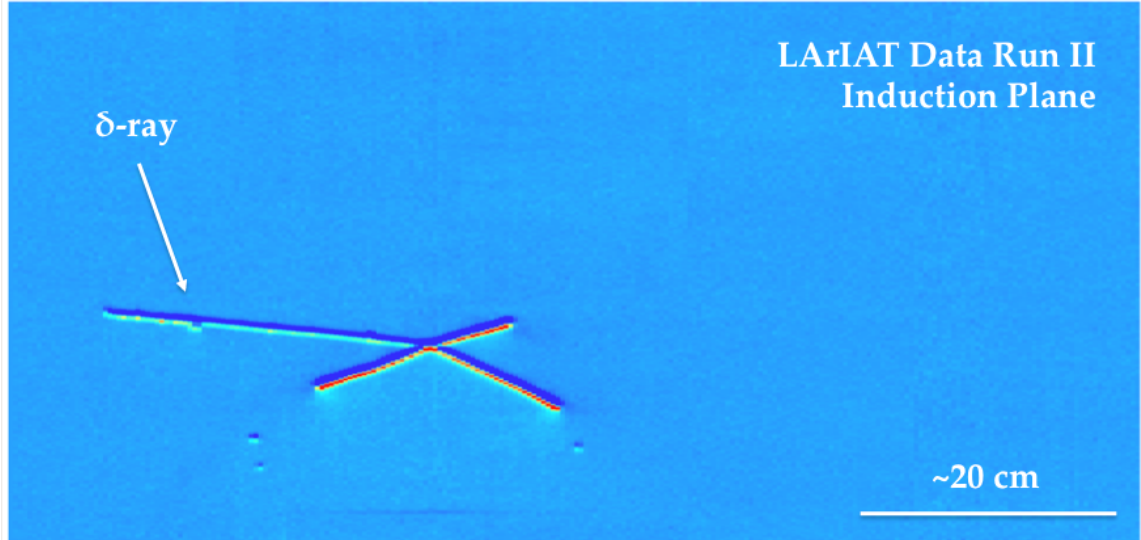


Figure 2.3: Events display for a LArIAT pion absorption candidate on the induction plane, with highlighted delta ray.

758 Purity & Electron Life Time

759 The presence of electronegative contaminants in liquid argon, such as oxygen O_2
760 and water H_2O , is particularly pernicious, since these molecules quench the charge
761 produced by the ionizing radiation. Thus, amount of charge per unit of length dQ/dx
762 collected on the collection plane depends on the charge's production point in the
763 detector: ionization produced close to the cathode will see more impurities along its
764 journey to the collection plane than ionization produced close to the anode, resulting
765 in greater attenuation of its charge. As a result, the amount of charge collected on
766 the sense wires as a function of the traveled distance follows an exponential decay
767 trend. The traveled distance is generally measured in terms of drift time and the
768 characteristic time constant of the exponential decay is called electron lifetime τ_e .
769 Figure 2.4 shows the typical life time for LArIAT data. The procedure to measure
770 the electron lifetime in LArIAT is outlined in [97]. LArIAT small drift distance (47
771 cm) allows for a relatively short electron life time. The life time for bigger detectors
772 such as MicroBooNE, whose drift distance is 2.6 m, needs to be of the order of
773 tens of milliseconds to allow a charge collection usable for physics analyses. Energy

774 reconstruction in LArTPC applies a correction for the finite lifetime to calibrate the
775 detector calorimetric response; details for LArIAT are provided in Section 5.3.

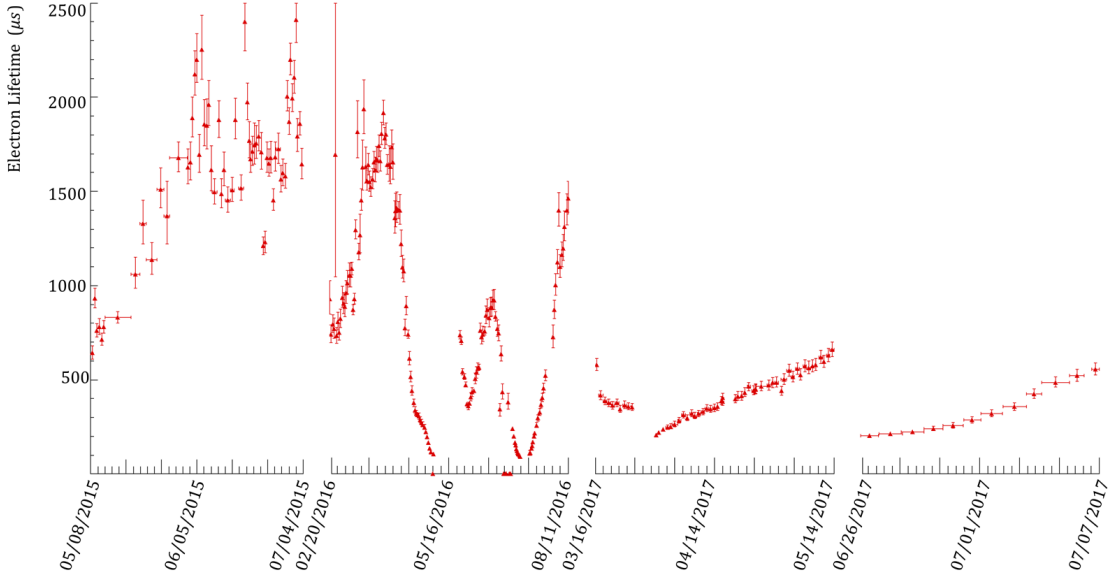


Figure 2.4: Electron lifetime during the LArIAT run period [38].

776 LArTPCs use hermetically sealed and leak-checked vessels to abate the leakage
777 and diffusion of contaminants into the system. The liquid argon filling of the vol-
778 ume occurs after the vessel is evacuated or purged with gaseous argon [9] to reduce
779 remaining gases in the volume. Even so, the construction of a pure tank of argon is
780 unviable, as several sources of impurity remain. In particular, impurities can come
781 from the raw argon supply, the argon filtration system and from the outgassing from
782 internal surfaces. Outgassing is a continuous diffusive process producing contami-
783 nants, especially water, even after the vessel is sealed, particularly from materials in

784 the ullage region². Since research-grade argon comes from the industrial distillation
785 of air, the impurities with the highest concentration are nitrogen, oxygen and water,
786 generally maintained under the 1 part per million level by the vendor. Even so, a
787 higher level of purity is necessary to achieve a free electron life time usable in meter
788 scale detectors. Thus, argon is constantly filtered in the cryogenic system, which
789 reduce the oxygen and water contamination to less than 100 parts per trillion. The
790 filtration system depends on the size and drift distance of the experiment and, for
791 experiments on several meters scale, it includes an argon recirculation system.

792 Recombination Effect

793 After production, ionization electrons thermalize with the surrounding medium and
794 may recombine with nearby ions. Recombination might occur either between the
795 electron and the parent ion through Coulomb attraction, as described in the geminate
796 theory [93], or thanks to the collective charge density of electrons and ions from
797 multiple ionizations in a cylindrical volume surrounding the particle trajectory, as
798 described in the columnar model [74]. Consideration on the average electron-ion
799 distance and the average ion-ion distance for argon show that the probability of
800 geminate recombination is low; thus recombination in argon is mainly due to collective
801 effects [4]. Since protons, kaons and stopping particles present a higher ionization
802 compared to MIPs, recombination effects are more prominent when considering the
803 reconstruction of energy deposited by these particles.

804 Theoretical descriptions of recombination based on the Birks model and the Box
805 model are provided in [27] and [105], respectively. The Birks model assumes a gaus-
806 sian spatial distribution around the particle trajectory during the entire recombi-
807 nation phase and identical charge mobility for ions and electrons. The Box model also

2. While the liquid argon low temperature reduces outgassing in the liquid, this process remains significant for absorptive material (such as plastic) above the surface of the liquid phase.

assumes that electron diffusion and ion mobility are negligible in liquid argon during recombination. In these models, the fraction of ionization electrons surviving recombination is a function of the number of ion-electron pairs per unit length, the electric field, the average ion-electron separation distance after thermalization and the angle of the particle with respect to the direction of the electric field – plus the diffusion coefficient in the Birks model. Given the stringent assumptions, it is perhaps not surprising that these models are in accordance to data only in specific regimes: the Birks model is generally used to describe recombination for low dE/dx , the Box model for high dE/dX . In LArTPC, the ICARUS and ArgoNeut experiments have measured recombination in [15] and [4] respectively. Since LArIAT uses the refurbished ArgoNeut TPC and cryostat at the same electric field, LArIAT currently corrects for recombination using the ArgoNeut measured recombination parameters in [4].

Space Charge Effect

Slow-moving positive argon ions created during ionization can build-up in LArTPC, causing the distortion of the electric field within the detector. This effect, called “space charge effect” leads to a displacement in the reconstructed position of the signal ionization electrons. In surface LArTPCs the space charge effect is primarily due to the rate of ionization produced by cosmic rays which is slowly drifting in the chamber at all times. Surface LArTPC of the size of several meters are expected to be modestly impacted from the space charge effect, where charge build-up creates anisotropy of the electric field magnitude of the order of 5% at a drift field of 500 V/cm [87]. The smallness of the LArIAT drift volume is such that effect of space charge on the electric field is expected to be negligible. **CHIEDI A FLAVIO**

831 **2.1.4 Liquid Argon: Scintillation Light**

832 Liquid argon emits scintillation light at the passage of charged particles. LArTPCs
833 leverage this property to determine when the ionization charge begins to drift towards
834 the anode plane.

835 **Scintillation Process**

836 Scintillation light in argon peaks in the ultraviolet at a 128 nm, shown in comparison
837 to Xenon and Kypton in Figure 2.5, from [88]. The light yield collected by the optical
838 detector depends on the argon purity, the electric field, the dE/dx and particle type,
839 averaging at the tens of thousands of photons per MeV.

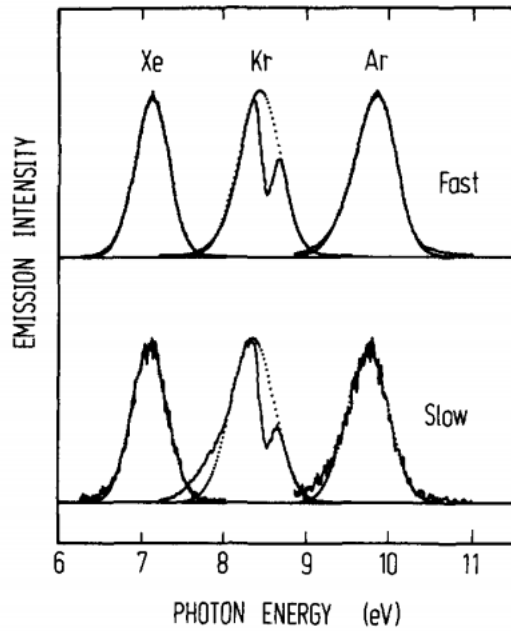


Figure 2.5: Emission spectra of the fast and slow emission components in Xenon, Kypton and Argon according to [88]. The dotted lines correspond to the Gaussian fits.

840 The de-excitation of Rydberg dimers in the argon is responsible for the scintillation
841 light. Rydberg dimers exist in two states: singlets and a triplets. The time constant
842 for the singlet radiative decay is 6 ns, resulting in a prompt component for the scin-

tillation light. The decay of the triplet is delayed by intersystem crossing, producing a slow component with a time constant of ~ 1500 ns. “Self-trapped exciton luminescence” and “recombination luminescence” are the two processes responsible for the creation of the Rydberg dimers [77]. In the first process, a charged particle excites an argon atom which becomes self-trapped in the surrounding bulk of argon, forming a dimer; the dimer is in the singlet state 65% of the times and in the triplet state 35% of the times. In case of recombination luminescence, the charged particle transfers enough energy to ionize the argon. The argon ion forms a charged argon dimer state, which quickly recombines with the thermalized free electron cloud. Excimer states are produced in the recombination, roughly half in the singlet and half in the triplet state. The light yield dependency on the electric field, on the dE/dx and particle type derives from the role of free charge in the recombination luminescence process. The spacial separation between the argon ions and the free electron cloud depends on the electric field. On one hand, a strong electric field diminishes the recombination probability, leading to a smaller light yield; on the other, it increases the free charge drifting towards the anode plane. Hence, the amount of measurable charge and light anti-correlates as a function of the electric field. Ionizing particles in the argon modify the local density of both free electrons and ions depending on their dE/dx . Since the recombination rate is proportional to the square of the local ionization density, highly ionizing particles boost recombination and the subsequent light yield compared to MIPs. The possibility to leverage this dependency for pulseshape-based particle identification has been shown in [29, 82].

Effects Modifying the Light Yield

The production mechanism through emission from bound excimer states implies that argon is transparent to its own scintillation light. In fact, the photons emitted from these metastable states are not energetic enough to re-excite the argon bulk, greatly

869 suppressing absorption mechanisms. In a LArTPC however, several processes modify
870 the light yield in between the location where light is produced and the optical detector.
871 In a hypothetical pure tank of argon, Rayleigh scattering would be the most important
872 processes modifying the light yield. Rayleigh scattering changes the path of light
873 propagation in argon, prolonging the time between light production and detection.
874 The scattering length has been measured to be 66 cm [73] , shorter than the theoretical
875 prediction of \sim 90 cm [104]; this value is short enough to be relevant for the current
876 size of LArTPCs detectors. In fact, Rayleigh scattering worsen the resolution on t_0 ,
877 the start time for charge drifting, and alters the light directionality, complicating the
878 matching between light and charge coming from the same object in case of multiple
879 charged particles in the detector.

880 Traces of impurities in argon such as oxygen, water and nitrogen also affect the
881 light yield, mainly via absorption and quenching mechanisms. Absorption occurs as
882 the interaction of a 128 nm photon directly with the impurity dissolved in the liquid
883 argon. Differently, quenching occurs as the interaction of an argon excimer and an
884 impurity, where the excimer transfers its excitation to the impurity and dissociates
885 non-radiatively. Given this mechanism, it is evident how quenching is both a function
886 of the impurity concentrations and the excimer lifetime. Since the triplet states
887 live much longer than the singlet states, quenching occurs mainly on triplet states,
888 affecting primarily the slow component of the light, reducing the scintillation yield
889 and a shortening of the scintillation time constants.

890 The stringent constraints for the electron life time limit the presence of oxygen and
891 water to such a low level that both absorption and quenching on these impurity is not
892 expected to be significant. Contrarily, the nitrogen level is not bound by the electron
893 life time constraints – nitrogen being an inert gas, expensive to filter. Thus, nitrogen
894 is often present at the level provided by the vendor. The effects of nitrogen on argon
895 scintillation light have been studied in the WArP R&D program and at several test

896 stands. The quenching process induced by nitrogen in liquid Ar has been measured
897 to be proportional to the nitrogen concentration, with a rate constant of ~ 0.11
898 μs^{-1} ppm $^{-1}$; appreciable decreasing in lifetime and relative amplitude of the slow
899 component have been shown for contamination as high as a few ppm of nitrogen [5].
900 For a nitrogen concentration of 2 parts per million, typical of the current generation
901 of LArTPC, the attenuation length due to nitrogen has been measured to be ~ 30
902 meters [76].

903 Wavelength Shifting of LAr Scintillation Light

904 Liquid argon scintillation light is invisible for most optical detectors deployed in a
905 LArTPC, such as cryogenic PMTs and SiPMs, since a wavelength of 128 nm is gen-
906 erally too short to be absorbed from most in glasses, polymers and semiconductor
907 materials. Research on prototype SiPMs absorbing directly VUV light and their
908 deployment in noble gasses experiment is ongoing but not mature [112]. Thus, ex-
909 periments need to shift the wavelength of scintillation light to be able to detect it.
910 Albeit deployed in different ways, neutrinos and dark matter experiments commonly
911 use 1,1,4,4-tetraphenyl-butadiene (TPB) to shift the scintillation light. TPB absorbs
912 the vacuum ultraviolet (VUV) light and emits in the visible at ~ 425 nm [31], with
913 a ratio of visible photon emitted per VUV photon absorbed of $\sim 1.2:1$ [61].

914 Neutrino experiments typically coat their optical detector system evaporating a
915 layer of TPB either directly on the PMTs glass surface or on acrylic plates mounted in
916 front of the PMTs [55]; this technique allows the fast detection light coming directly
917 from the neutrino interaction. Dark matter experiments typically evaporate TPB on
918 reflective foils mounted on the inside walls of the sensitive volume and detect the
919 light after it has been reflected; this technique leads to a higher and more uniform
920 light yield, though scattering effects for both the visible and VUV light augment
921 the propagation time and hinder directionality information [56]. In order to take

922 advantage of both these techniques, hybrid systems with PMT coating and foils are
923 being considered for the next generation of large neutrino detectors.

924 **2.1.5 Signal Processing and Event Reconstruction**

925 In this section we illustrate the processing and reconstruction chain of the TPC sig-
926 nals, from the pulses on the sense wire to the construction of three dimensional objects
927 with associated calorimetry. Different experiments can chose different software pack-
928 ages for their off line signal processing and event reconstruction, but a popular choice
929 for US based LArTPCs is LArSoft [35]. Based on the Art framework [67], LArSoft is
930 an event-based toolkit to perform simulation, analysis and reconstruction of LArT-
931 PCs events.

932

933 LArTPC signal processing develops in several consecutive stages that we summa-
934 rize here in the following categories: *Deconvolution*, *Hit Reconstruction*, *2D Cluster-*
935 *ing*, *3D Tracking*, *Calorimetry Reconstruction*. A visualization of the signal processing
936 workflow is shown in figure 2.6.

937

938 **Deconvolution.** Induction and collection planes have different field responses,
939 given the different nature of the signals on these planes: the wires on the induction
940 planes see the inductive signal of the drifting charge, while the wires on the collection
941 planes see the current derived from the charge entering the conductor. Thus, signals
942 on the induction plane are bi-polar pulse and signal on the collection plane are unipo-
943 lar pulses, see Figure 2.6 panel a). The first step in signal processing is deconvolution,
944 that is a series of off-line algorithms geared towards undoing the detector effects. The
945 result of the deconvolution step is the production of a comparable set waveforms on
946 all planes presenting unipolar, approximately gaussian-like pulses (Figure 2.6 panel
947 b)). Signal from all planes are treated on equal footage beyond this point. Some

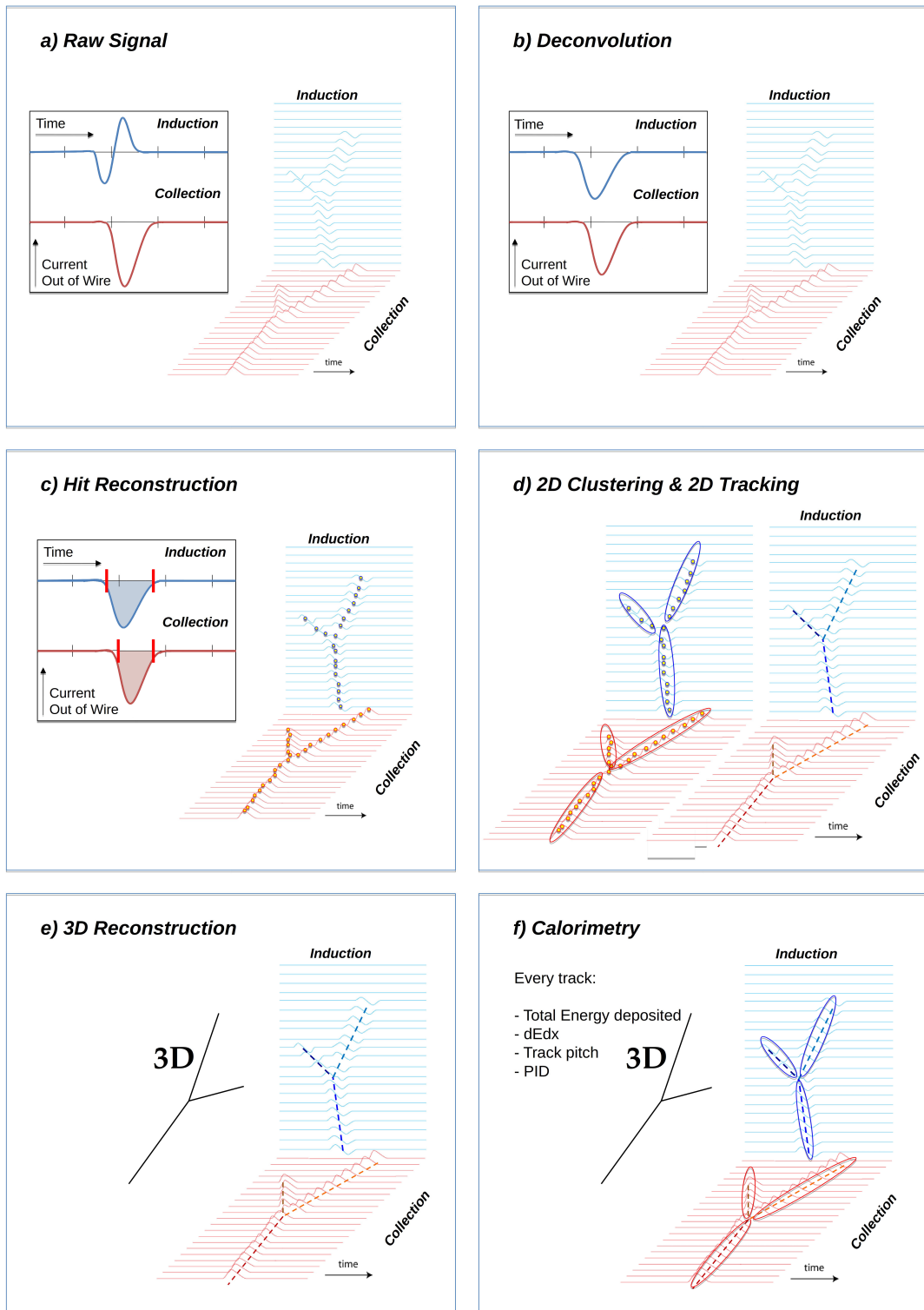


Figure 2.6: A scheme of a typical signal processing workflow in LArSoft.

948 LArTPC apply noise filtering in the frequency domain just after the deconvolution
949 to clean up wire cross talk. Since signals from the LArIAT TPC are extremely clean,
950 noise filtering is not necessary.

951

952 **Hit Reconstruction.** The second stage of the signal processing is the recon-
953 struction of hits, indicating an energy deposition in the detector. A peak finder scans
954 the deconvolved TPC waveforms for each wire on the whole readout time looking for
955 spikes above the waveform’s baseline. It then fits these peaks with gaussian shapes
956 and stores the fit parameters such as the quality of the fit, the peak time, height and
957 area under the gaussian fit. The information resulting from this process on a single
958 spike form a single reconstructed “hit”, see Figure 2.6 panel c). The next steps in
959 the event reconstruction chain will then decide if rejecting hits with poor fits. It is
960 important to notice how the height and width of the hit depend on the topology of
961 the event: for example, a particle running parallel to the wire planes will leave a series
962 of sharp hits on many consecutive wires, while a particle traveling towards the planes
963 will leave a long, wide hit on very few wires. The height of the hits and their integral
964 is proportional to the charge collected on the wire, so it depends on the particle type.

965

966 The event reconstruction chain uses collection of hits to form more complex objects
967 associated with the particles in the detector. The development of different approaches
968 to accomplish this task is an extremely hot topic in LArTPC event reconstruction
969 which spans from more traditional approaches such as line-clustering [24] to the use of
970 machine learning tools [54]. Generally speaking, the scope of hit clustering and event
971 reconstruction to provide shower-like or track like-objects with an associated energy
972 reconstruction. This is because different particles have different topology in the de-
973 tector – electrons and photon create electromagnetic showers, resulting in shower-like
974 topologies, while muons and hadrons leave track-like signals. For the scope of these

975 thesis, we will describe only LArIAT's approach to track reconstruction even if we
976 recognize the breath of LArTPC event reconstruction is much wider. We are inter-
977 ested in the reconstruction of pions and kaons in the active volume, whose topology
978 is track-like.

979

980 **2D Clustering Reconstruction.** The LArIAT reconstruction of track-like ob-
981 jects starts by clustering hits on the collection and induction planes separately with
982 the use of the TrajCluster clustering package [23]. TrajCluster looks for a collection
983 of hits in the wire-time 2D space which can be described with a line-like 2D trajec-
984 tory. TrajCluster reconstructs trajectories by adding trajectory points to the leading
985 edge of the trajectory while stepping through the 2D space of hits. Several factors
986 determine whether a hit is added to the trajectory, including but not limited to

- 987 1. the goodness of the fit of the single hit,
988 2. the charge of the hit compared to the average charge and RMS of the hits
989 already forming the trajectory,
990 3. the goodness of trajectory fit with and without the hit addition,
991 4. the angle between the two lines formed by the collection of hits before and after
992 the considered hit in the trajectory.

993 The final product of this reconstruction stage is the collection of bidimensional clusters
994 on each wire plane, see Figure 2.6 panel d).

995 **3D Tracking.** The 3D tracking set of algorithms uses clusters close in time on
996 the induction and collection planes as starting point to form a 3D track. Firstly, it
997 construct a tentative 3D trajectory using the edges of the clusters. Then, it projected
998 back the tentative trajectory on to the planes and adjusts the parameters of the 3D
999 track fit such that they minimize the distance between the fit projections and the

1000 track hits in all wire planes simultaneously. Tridimensional tracking can use multiple
1001 clusters in one plane, but it can never break them in smaller groups of hits. This
1002 algorithm was first developed for the ICARUS collaboration [18]. The final product
1003 of this reconstruction stage is the formation of tridimensional objects in the TPC
1004 active volume, see Figure 2.6 panel e).

1005

1006 **Calorimetry.** The last step in the event reconstruction chain is to assign calorimetric
1007 information to the track (or shower) objects. Calorimetry is performed separately
1008 on the different planes. A multi-step procedure is needed to retrieve the energy
1009 deposited in the TPC from the charge seen by the wires. For each hit associated with
1010 the track object, the calorimetry algorithms calculate the charge seen on every wire
1011 using the area underneath the gaussian fit; then, they correct this raw charge by the
1012 electron life time, the electronic noise on the considered wire and the recombination
1013 effect. Lastly an overall calibration of the energy, explained in detail in section 5.3,
1014 is applied and the calorimetric information for the given track is assigned. Even if
1015 calorimetry is done in 2D, it benefits from the 3D tracking information; typical information
1016 available after the calorimetric reconstruction are the total energy deposited
1017 by the particle and its stopping power dE/dx at each “track pitch”, i.e. at each 2D
1018 projection on the wire plane of the 3D trajectory.

1019 **2.2 The Intensity Frontier Program**

1020 **2.2.1 Prospects for LArTPCs in Neutrino Physics: SBN and** 1021 **DUNE**

1022 The ArgoNeut experiment [16] initiated the US LArTPC neutrino program. Following
1023 the success of this small TPC on the NuMI beam, a wide program of LArTPCs
1024 on neutrino beams has flourished. The construction of LArTPCs as near and far

1025 detectors at different baseline allows for the exploration of some of the fundamental
1026 questions in neutrino physics today illustrated in section 1.3.1.

1027 The Short-Baseline Neutrino (SBN) [19] program at Fermilab is tasked with con-
1028 clusively assess the nature of the “LSND and MiniBooNE anomalies” [13, 14, 21],
1029 resolving the mystery of sterile neutrinos at the eV² scale. The SBN program entails
1030 three surface LArTPCs positioned on the Booster Neutrino Beam at different dis-
1031 tances from the neutrino production in oder to fully exploit the L/E dependence of
1032 the oscillation pattern: SBND (100 m from the decay pipe), MicroBooNE (450 m),
1033 and ICARUS (600 m). Within the oscillation context, the choice of the LArTPC tech-
1034 nology for the SBN detectors changes the set of systematics with respect to LSND
1035 and MiniBooNE, whose detection techniques were both based on Cherenkov light.
1036 In particular, LArTPCs provide excellent electron/photon separation [8] lacking in
1037 Cherenkov detectors which can be leveraged to abate the photon background from
1038 neutral current interactions in ν_e searches. MicroBooNE [7], the first detector of the
1039 SBN program to be fully operational, started its first neutrino run in October 2015.
1040 MicroBooNE is a 89 ton active volume LArTPC, single drift chamber with TPC di-
1041 mensions of 2.6 m (drift) x 2.3 m (heigh) x 10.4 m (depth). MicroBooNE is positioned
1042 at a very similar L/E on the Booster neutrino beam as MiniBooNE has the scope to
1043 directly cross check the MiniBooNE oscillation measurement. In case MicroBooNE
1044 confirms the presence of the “low energy excess” anomaly, SBND and ICARUS will
1045 provide the full measurement of the oscillation parameters. SBND and ICARUS are
1046 both dual drift chambers, whose active volume is respectively 112 ton and 600 ton.
1047 ICARUS is scheduled to become operational by the end of 2018 and SBND shortly
1048 after. Besides the oscillation analysis, the second main goals of SBN is to perform
1049 an extensive campaign of neutrino cross section measurements in argon. Given the
1050 importance of nuclear effects in (relatively) heavy materials, as discussed in section
1051 1.2.3, both the oscillation analysis of the SBN program and the measurements of

1052 neutrino properties in DUNE will benefit from such a campaign.

1053 On a different neutrino beam and baseline, the DUNE experiment, née LBNE [10],
1054 is the flagship experiment on the medium-long term of US-based neutrino physics,
1055 scheduled to start data taking in 2026. Shooting neutrinos from Fermilab for 800 miles
1056 to the SURF laboratory in South Dakota, DUNE is tasked with performing conclusive
1057 measurements of CP violation in the lepton sector, the neutrino mass ordering and
1058 the θ_{23} octant. The DUNE far detector will count four 10 kton LArTPCs, roughly of
1059 dimensions of 19 m (horizontally) x 18 m (vertically) x 66 m (depth).

1060 **2.2.2 Prospects for LArTPCs in GUT Physics: DUNE**

1061 The experimental exploration of a manifestation of Grand Unified Theory is possible
1062 in DUNE thanks to its sheer mass. In particular, proton decay searches are a capital
1063 topic of DUNE's wide non-accelerator physics program. The key elements for a
1064 rare decay experiment are: massive active volume, long exposure, high identification
1065 efficiency and low background. Figure 2.7 shows the current best experimental limits
1066 on nucleon decay lifetime over branching ratio (dots). Historically, the dominant
1067 technology used in these searches has been water Cherenkov detectors: all the best
1068 experimental limits on every decay mode are indeed set by Super-Kamiokande [?,?].
1069 As shown in section 1.3.2, different family of GUTs predict the proton to decay in
1070 different modes. In particular, SUSY flavored GUTs prefer the presence of kaons
1071 in the decay products, e.g. $p \rightarrow K^+ \bar{\nu}$. It is particularly important to notice that
1072 the kaon energy for the proton decay mode $p \rightarrow K^+ \bar{\nu}$ is under Cherenkov threshold
1073 in water. Thus, Super-Kamiokande set the limit on the lifetime for the $p \rightarrow K^+ \bar{\nu}$
1074 mode by relying on photons from nuclear de-excitation and on the muon tagging in
1075 the kaon decay leptonic mode. For this reason, an attractive alternative approach to
1076 identifying nucleon decay is the use of a LArTPCs, where the kaon is directly visible
1077 in the detector. According to [10], DUNE will have an active volume large enough,

1078 have sufficient shielding from the surface, and will run for lengths of time sufficient
 1079 to compete with Hyper-K, opening up the opportunity for the discovery of nucleon
 1080 decay.

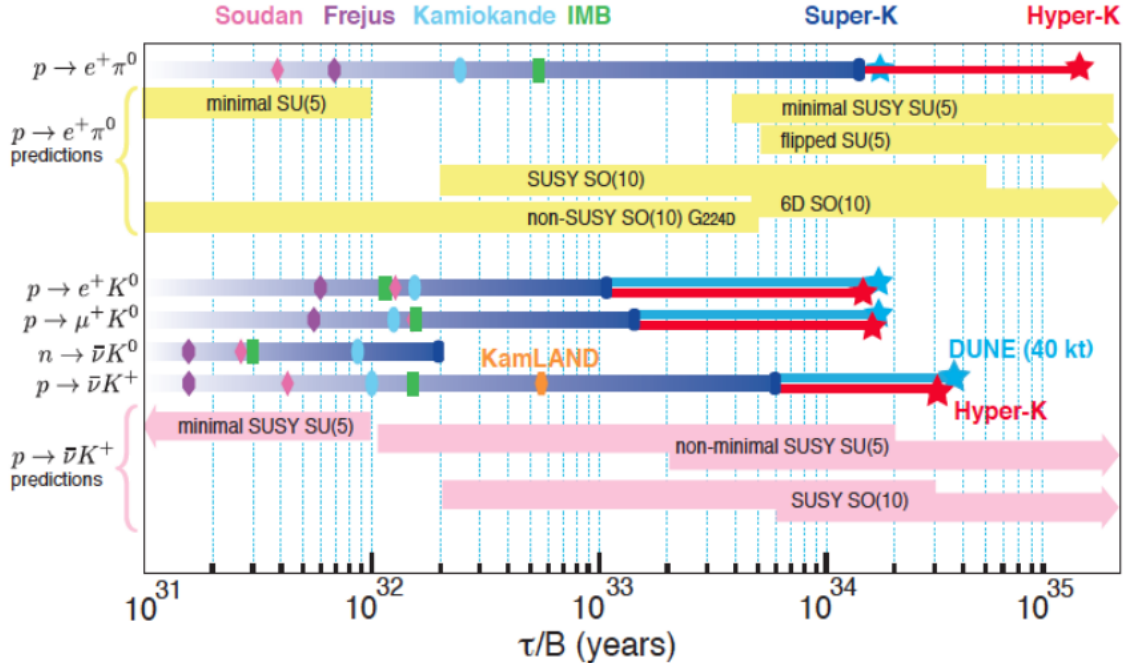


Figure 2.7: Proton decay lifetime limits from passed and future experiments.

1081 2.2.3 Enabling the next generation of discoveries: LArIAT

1082 LArIAT, a small LArTPC in a test beam, is designed to perform an extensive physics
 1083 campaign centered on charged particle cross section measurements while characteriz-
 1084 ing the detector performance for future LArTPCs. Since LArTPCs represent the most
 1085 advanced experiments for physics at the Intensity Frontier, their complex technology
 1086 needs a thorough calibration and dedicated measurements of some key quantities to
 1087 achieve the precision required for the next generation of discoveries. LArIAT's goal
 1088 is to provide such calibration and dedicated measurements. The LArIAT LArTPC is
 1089 deployed in a dedicated calibration test beamline at Fermilab. We use the LArIAT
 1090 beamline to characterize the charge particles before they enter the TPC: the particle

1091 type and initial momentum is known from beamline information. The precise calor-
1092 metric energy reconstruction of the LArTPC technology enables the measurement of
1093 the total differential cross section for tagged hadrons. The Pion-Nucleus and Kaon-
1094 Nucleus total hadronic interaction cross section have never been measured before in
1095 argon and they are a fundamental step to shed light on light meson interaction in nu-
1096 clei per se, while providing a key input to neutrino physics and proton decay studies
1097 in future LArTPC experiments like SBN and DUNE.

1098 In order to showcase LArIAT’s utility to SBN and DUNE, we illustrate briefly
1099 two comparisons as examples: one regarding neutrino interactions and the second
1100 regarding proton decay studies.

1101 The left side of figure 2.8 shows the distribution of products in momentum spectrum
1102 and particle type as simulated in a ν_e CC interaction in DUNE (according to [81]);
1103 the range of these distribution is to compare with the momentum distribution of
1104 light particles in the LArIAT beamline – shown on the right side of figure 2.8. The
1105 momentum spectrum in the LArIAT beamline for electrons, muons and pions – the
1106 most abundant particles produced in a ν_e CC interaction – covers a wide range of the
1107 expected momentum distribution in a neutrino event.

1108 The signature of a proton decay event in the “LAr golden mode” is the presence of
1109 a single kaon of about 400 MeV in the detector; the momentum spectrum of the kaon
1110 pre and post FSI in such an event as simulated by GENIE is shown on the left side
1111 of figure 2.9. The right side of figure 2.9 shows the momentum spectrum of kaons in
1112 the LArIAT beamline. Kaons arriving to the LArIAT TPC are ideal for proton decay
1113 studies, since their momentum in the beamline is just above the typical momentum
1114 for kaons in a proton decay event: the majority of LArIAT kaons slow down in the
1115 TPC enough to enter the desired momentum window.

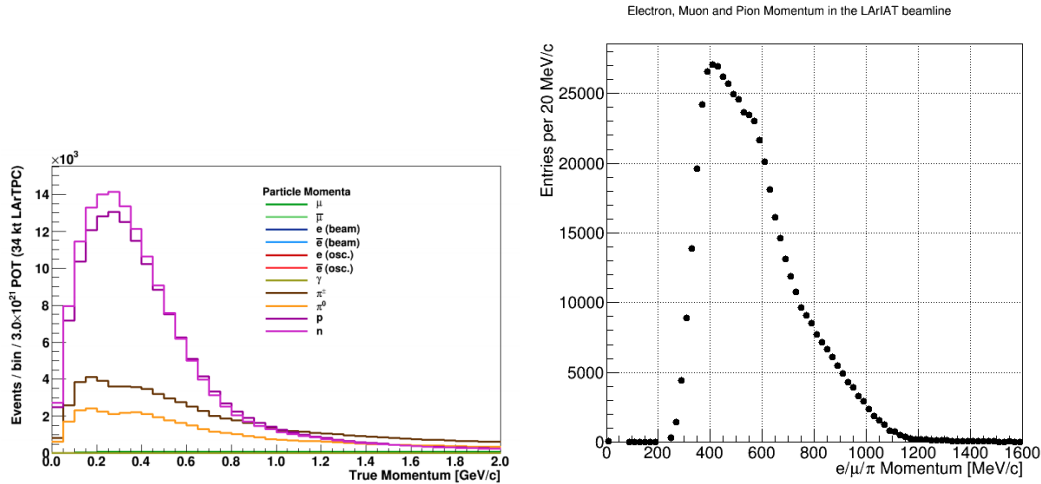


Figure 2.8: *Left.* Simulation of the products of a ν_e CC interaction in DUNE, both in particles type and momentum.
Right. Momentum spectrum for low mass particles (e, μ, π) in the LArIAT beamline, negative tune, Run II, Picky Tracks see section 3.2.2.

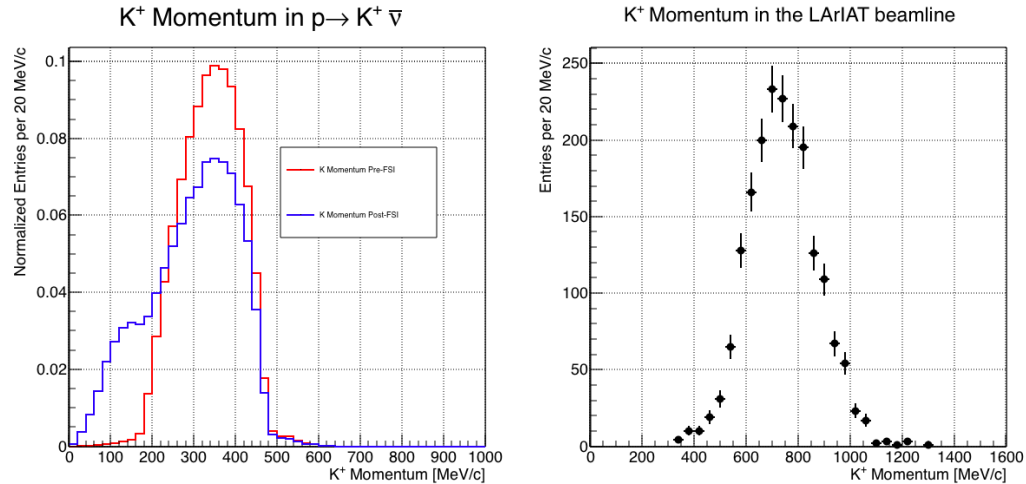


Figure 2.9: *Left.* Momentum of the kaon outgoing a proton decay $p \rightarrow K^+ \bar{\nu}$ event as simulated by the Genie 2.8.10 event generator in argon. The red line represents the kaon momentum distribution before undergoing the simulated final state interaction inside the argon nucleus, while the blue line represents the momentum distribution after FSI.
Right. Positive Kaon momentum spectrum in the LArIAT beamline, positive tune, Run II, Picky Tracks see section 3.2.2.

1116 **Chapter 3**

1117 **LArIAT: Liquid Argon In A**

1118 **Testbeam**

1119 In this chapter, we describe the LArIAT experimental setup. We start by illustrating
1120 the journey of the charge particles in the Fermilab accelerator complex, from
1121 the gaseous thermal hydrogen at the Fermilab ion source to the delivery of the LAr-
1122 IAT tertiary beam at MC7. We then describe the LArIAT beamline detectors, the
1123 LArTPC, the DAQ and the monitoring system.

1124 **3.1 The Particles Path to LArIAT**

1125 LArIAT's particles history begins in the Fermilab accelerator complex with a beam of
1126 protons. The process of protons acceleration develops in gradual stages (see picture
1127 3.1): gaseous hydrogen is ionized in order to form H^- ions; these ions are boosted to
1128 750 keV by a Cockcroft-Walton accelerator and injected to the Linac linear accelerator
1129 that increases their energy up to 400 MeV; then, H^- ions pass through a carbon
1130 foil and lose the two electrons; the resulting protons are then injected into a rapid
1131 cycling synchrotron, called Booster; at this stage, protons reach 8 GeV of energy
1132 and are compacted into bunches; the next stage of acceleration is the Main Injector,

1133 a synchrotron which accelerates the bunches up to 120 GeV; in the Main Injector,
1134 several bunches are merged into one and are ready for delivery.

1135 The Fermilab accelerator complex works in supercycles of roughly 60 seconds in
1136 duration. The beam is split by electrostatic septa and delivered at different experi-
1137 mental halls all over the lab. A 120 GeV primary proton beam with variable intensity
1138 is extracted in four-second “spills” and sent to the Meson Center beam line.

1139 LArIAT’s home at Fermilab is the Fermilab Test Beam Facility (FTBF), where
1140 the experiment characterizes a beam of charge particles downstream from the Meson
1141 Center beam line. Here, the primary beam is focused onto a tungsten target to create
1142 LArIAT’s secondary beam. The composition of the secondary particle beam is mainly
1143 positive pions. The momentum peak of the secondary beam was fixed at 64 GeV/c for
1144 the LArIAT data considered in this work, although the beam is tunable in momentum
1145 between 8-80 GeV/c; this configuration of the secondary beamline assured a stable
1146 beam delivery at the LArIAT experimental hall.

1147 The secondary beam impinges then on a copper target within a steel collimator
1148 inside the LArIAT experimental hall (MC7) to create the LArIAT tertiary beam,
1149 (shown in Fig. 3.2). The steel collimator selects particles produced with a 13° pro-
1150 duction angle at the target down the beamline. The particles are then bent by roughly
1151 10° through a pair of dipole magnets. By configuring the field intensity of the magnets
1152 we allow the particles of LArIAT’s tertiary beam to span a momentum range from
1153 0.2 to 1.4 GeV/c. The polarity of the magnet is also configurable and determines
1154 the sign of the beamline particles which are focused on the LArTPC. If the magnets
1155 polarity is positive the tertiary beam composition counts mostly pions and protons
1156 with a small fraction of electrons, muons, and kaons. It is the job of the LArIAT
1157 beamline detectors to select the particles polarity, to perform particle identification
1158 in the beamline and to measure the momentum of the tertiary beam particles be-
1159 fore they get to the LArTPC. The LArIAT detectors are described in the following

Fermilab Accelerator Complex

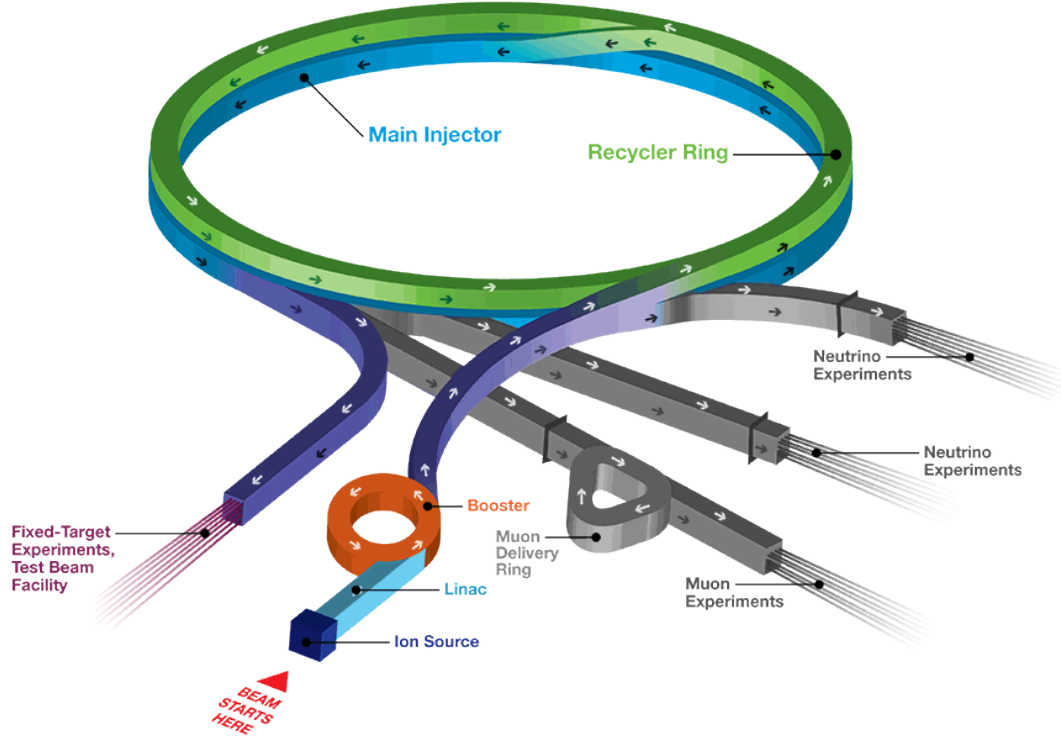


Figure 3.1: Layout of Fermilab Acellerator complex.

¹¹⁶⁰ paragraphs.

¹¹⁶¹ 3.2 LArIAT Tertiary Beam Instrumentation

¹¹⁶² The instrumentation of LArIAT tertiary beam and the TPC components have changed
¹¹⁶³ several times during the three years of LArIAT data taking. The following paragraphs
¹¹⁶⁴ describe the components operational during “Run II”, the data taking period relevant
¹¹⁶⁵ to the hadron cross section measurements considered in this thesis.

¹¹⁶⁶ The key components of the tertiary beamline instrumentation for the hadron cross
¹¹⁶⁷ section analyses are the two bending magnets, a set of four wire chambers (WCs)
¹¹⁶⁸ and two time-of-flight scintillating paddles (TOF) and, of course, the LArTPC. The
¹¹⁶⁹ magnets determine the polarity of the particles in the tertiary beam; the combination

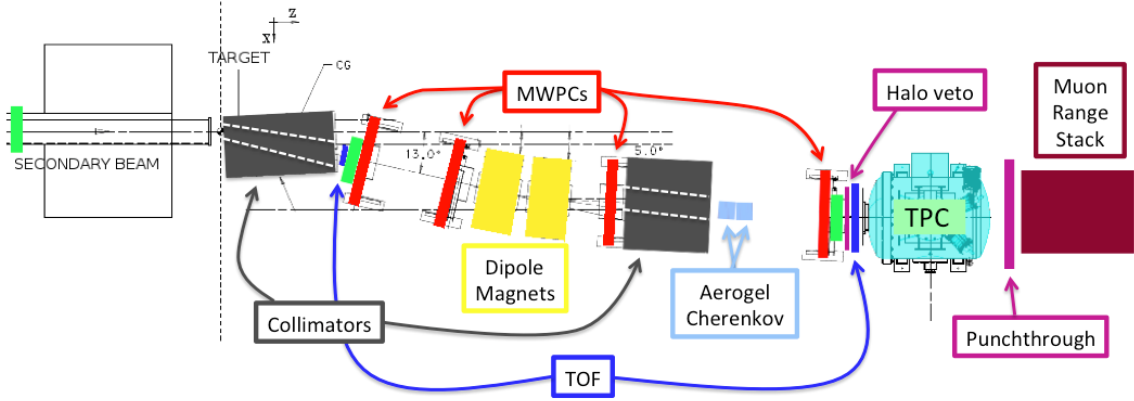


Figure 3.2: Bird’s eye view of the LArIAT tertiary beamline. In grey: upstream and downstream collimators; in yellow: bending magnets; in red: wire chambers; in blue: time of flight; in green: liquid argon TPC volume; in maroon: muon range stack.

of magnets and wire chambers determines the particles’ momentum, which is used to determine the particle species in conjunction with the TOF. A muon range stack downstream from the TPC and two sets of cosmic paddles configured as a telescope surrounding the TPC are also used for calibration purposes.

3.2.1 Bending Magnets

LArIAT uses a pair of identical Fermilab type “NDB” electromagnets, recycled from the Tevatron’s anti-proton ring, in a similar configuration used for the MINERvA T-977 test beam calibration [51]. The magnets are a fundamental piece of the LArIAT beamline equipment, as they are used for both particle identification and momentum measurement before the LArTPC. The sign of the current in the magnets allows us to select either positively or negatively charged particles; the value of the magnetic field is used in the momentum determination and in the subsequent particle identification.

We describe here the characteristics and response of one magnet, as the second one has a similar response, given its identical shape and history. Each magnet is a box with a rectangular aperture gap in the center to allow for the particle passage. The magnet aperture measures 14.224 cm in height, 31.75 cm in width, and 46.67 cm in length.

1186 Since the wire chambers aperture ($\sim 12.8 \text{ cm}^2$) is smaller than the magnet aperture,
 1187 only the central part of the magnet gap is utilized. The field is extremely uniform
 1188 over this limited aperture and was measured with two hall probes, both calibrated
 1189 with nuclear magnetic resonance probes. The probes measured the excitation curve
 1190 shown in Figure 3.3.

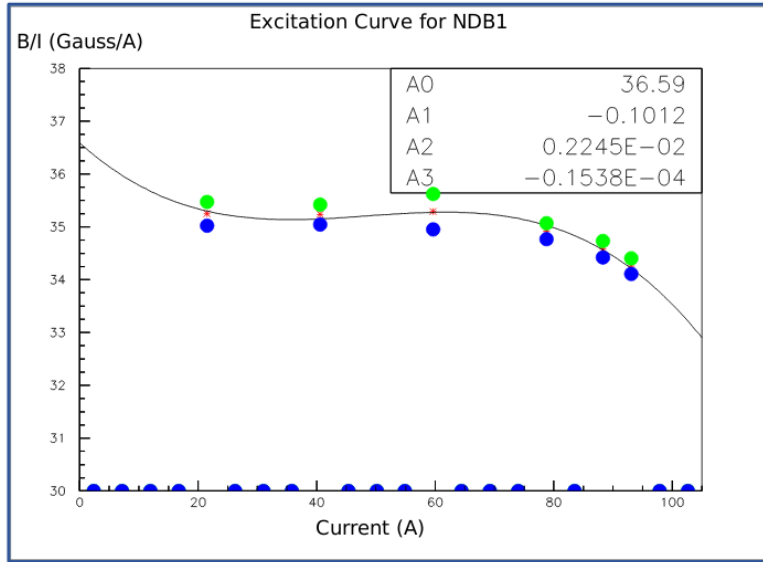


Figure 3.3: Magnetic field over current as a function of the current, for one NDB magnet (excitation curve). The data was collected using two hall probes (blue and green). We fit the readings with a cubic function (black) to average of measurements (red) given in the legend [38].

1191 The current through the magnets at a given time is identical in both magnets.
 1192 For the Run II data taking period, the current settings explored were 60A ($B \sim 0.21$
 1193 T) and 100A ($B \sim 0.35$ T) in both polarities. Albeit advantageous to enrich the
 1194 tertiary beam composition with high mass particles such as kaons, we never pushed
 1195 the magnets current over 100 A, not to incur in overheating. During operation, we
 1196 operated a air and water cooling system on the magnets and we remotely monitored
 1197 the magnets temperature.

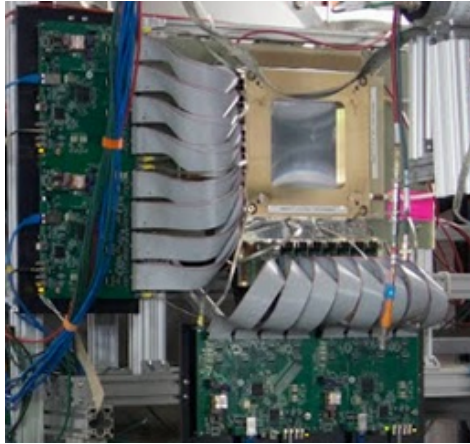


Figure 3.4: One of the four Multi Wire Proportional Chambers (WC) used in the LArIAT tertiary beamline and relative read-out electronics.

1198 3.2.2 Multi-Wire Proportional Chambers

1199 LArIAT uses four multi-wire proportional chambers, or wire chambers (WC) for short,
1200 two upstream and two downstream from the bending magnets. The geometry of one
1201 chamber is shown in Figure 3.4: the WC effective aperture is a square of 12.8 cm
1202 perpendicular to the beam direction. Inside the chamber, the 128 horizontal and 128
1203 vertical wires hang at a distance of 1 mm from each other in a mixture of 85% Argon
1204 and 15% isobutane gas. The WC operating voltage is between 2400 V and 2500 V.
1205 The LArIAT wire chambers are an upgraded version of the Fenker Chambers [57],
1206 where an extra grounding improves the signal to noise ratio of the electronic readout.

1207 Two ASDQ chips [89] mounted on a mother board plugged into the chamber serve
1208 as front end amplifier/discriminator. The chips are connected to a multi-hit TDC [68]
1209 which provides a fast OR output used as first level trigger. The TDC time resolution
1210 is 1.18 ns/bin and can accept 2 edges per 9 ns. The maximum event rate acceptable
1211 by the chamber system is of 1 MHz: this rate is not a limiting factor considering that
1212 the rate of the tertiary particle beam at the first wire chamber is estimated to be less
1213 than 15 kHz. A full spill of data occurring once per supercycle is stored on the TDC
1214 board memory at once and read out by a specially designed controller. We use LVDS
1215 cables to carry both power and data between the controller and the TDCs and from

1216 the controller to the rest of the DAQ.

1217 **Multi-Wire Proportional Chambers functionality**

1218 We use the wire chamber system together with the bending magnets to measure the
1219 particle's momentum.

1220 In the simplest scenario, only one hit on each and every of the four wire chambers
1221 is recorded during a single readout of the detector systems. Thus, we use the hit
1222 positions in the two wire chambers upstream of the magnets to form a trajectory
1223 before the bend, and the hit positions in the two wire chambers downstream of the
1224 magnets to form a trajectory after the bend. We use the angles in the XZ plane
1225 between the upstream and downstream trajectories to calculate the Z component of
1226 the momentum as follows:

$$P_z = \frac{B_{eff}L_{eff}}{3.3(\sin(\theta_{DS}) - \sin(\theta_{US}))}, \quad (3.1)$$

1227 where B_{eff} is the effective maximum field in a square field approximation, L_{eff}
1228 is the effective length of both magnets (twice the effective length of one magnet),
1229 θ_{US} is the angle off the z axis of the upstream trajectory, θ_{DS} is the angle off the
1230 z axis of the downstream trajectory and $3.3 c^{-1}$ is the conversion factor from [T·m]
1231 to [MeV/c]. By using the hit positions on the third and fourth wire chamber, we
1232 estimate the azimuthal and polar angles of the particle trajectory, and we are able to
1233 calculate the other components of the momentum.

1234 The presence of multiple hits in a single wire chamber or the absence of hits in one
1235 (or more) wire chambers can complicate this simple scenario. The first complication
1236 is due to beam pile up, while the latter is due to wire chamber inefficiency. In the
1237 case of multiple hits on a single WC, at most one wire chamber track is reconstructed
1238 per event. Since the magnets bend particles only in the X direction, we assume
1239 the particle trajectory to be roughly constant in the YZ plane, thus we keep the

1240 combination of hits which fit best with a straight line. It is still possible to reconstruct
1241 the particle's momentum even if the information is missing in either of the two middle
1242 wire chambers (WC2 or WC3), by constraining the particle trajectory to cross the
1243 plane in between the magnets.

1244 Events satisfying the simplest scenario of one single hit in each of the four wire
1245 chambers form the “Picky Track” sample. We construct another, higher statistics
1246 sample, where we loosen the requirements on single hit and wire chamber efficiency:
1247 the “High Yield” sample. For LArIAT Run II, the High Yield sample is about three
1248 times the Picky Tracks statistics. For the first measurements of the LArIAT hadronic
1249 cross section, we use the Picky Tracks sample because the uncertainty on the momen-
1250 tum is smaller and the comparison with the beamline MC results is straightforward
1251 compared with the High Yield sample; a possible future update and cross check of
1252 these analysis would be the use of the High Yield sample.

1253 **Four point track momentum uncertainty**

1254 **3.2.3 Time-of-Flight System**

1255 Two scintillator paddles, one upstream to the first set of WCs and one downstream
1256 to the second set of WCs form LArIAT time-of-flight (TOF) detector system.

1257 The upstream paddle is made of a 10 x 6 x 1 cm scintillator piece, read out by
1258 two PMTs mounted on the beam left side which collect the light from light guides
1259 mounted on all four edges of the scintillator. The downstream paddle is a 14 x 14 x
1260 1 cm scintillator piece read out by two PMTs on the opposite ends of the scintillator.
1261 The relatively thin width on the beamline direction minimizes energy loss of the
1262 particles coming from the target in the scintillator material.

1263 The CAEN 1751 digitizer is used to digitize the TOF PMTs signals at a sampling
1264 rate of 1 GHz. The 12 bit samples are stored in a circular memory buffer. At trigger
1265 time, data from the TOF PMTs are recorded to output in a 28.7 μ s windows starting

1266 approximately 8.4 μ s before the trigger time.

1267 **TOF functionality**

1268 The TOF signals rise time (10-90%) is 4 ns and a full width, half-maximum of 9 ns
1269 consistent in time. The signal amplitudes from the upstream TOF and downstream
1270 TOF are slightly different: 200 mV for the upstream PMTs but only 50 mV for
1271 downstream PMTs. The time of the pulses was calculated utilizing an oversampled
1272 template derived from the data itself. We take the pulse pedestal from samples far
1273 from the pulse and subtract it to the pulse amplitude. We then stretch vertically a
1274 template to match the pedestal-subtracted pulse amplitude and we move it horizon-
1275 tally to find the time. With this technique, we find a pulse time-pickoff resolution
1276 better than 100 ps. The pulse pile up is not a significant problem given the TOF
1277 timing resolution and the rate of the particle beam. Leveraging on the pulses width
1278 uniformity of any given PMT, we flag events where two pulses overlap as closely in
1279 time as 4 ns with an 90% efficiency according to simulation.

1280 We combine the pulses from the two PMTs on each paddle to determine the
1281 particles' arrival time by averaging the time measured from the single PMT, so to
1282 minimize errors due to optical path differences in the scintillator. However, a time
1283 spread of approximately 300 ps is present in both the upstream and downstream
1284 detectors, likely due to transit time jitter in the PMTs themselves. There is no
1285 evidence of systematic timing drift over long data-taking periods such as 3-4 months:
1286 the maximum variation of the average time differences between pairs of PMTs reading
1287 out the same scintillator is of the order of 150 ps.

1288 **3.2.4 Punch-Through and Muon Range Stack Instruments**

1289 The punch-thorough and the muon range stack (MuRS) detectors are located down-
1290 stream of the TPC. These detectors provide a sample of TPC crossing tracks without



Figure 3.5: Image of the down stream time of flight paddle, PMTs and relative support structure before mounting.

1291 relying on TPC information and can be used to improve particle ID for muons and
1292 pions with momentum higher than 450 MeV/c.

1293 The punch-thorough is simple sheet of scintillator material, read out by two PMTs.
1294 The MuRS is a segmented block of steel with four slots instrumented with scintillation
1295 bars. The four steel layers in front of each instrumented slot are 2 cm, 2 cm, 14 cm
1296 and 16 cm wide in the beam direction. Each instrumented slot is equipped with
1297 four scintillation bars each, positioned horizontally in the direction orthogonal to the
1298 beam. Each scintillator bar measures ? x ? x 2 cm and it is read out by one PMT.

1299 The signals from both the punch-thorough and the MuRS PMTs are digitized in
1300 the CAEN V1740, same as the TPC; the details of this discriminator are laid out
1301 in 3.3.2. It is worth noticing that the sampling time of the CAEN V1740 is slow
1302 (of the order of 128 ns), so pulse shape information from the PMT is lost. Punch-
1303 thorough and MuRS hits are formed utilizing the digital discriminator signals under
1304 threshold at a given time, where we obtain the threshold for each PMT directly on
1305 data distributions.

1306 It is worth mentioning here the presence of an additional scintillation paddle
1307 between WC4 and the downstream paddle of the TOF system, called halo. The
1308 halo is a 39x38x1 cm³ paddle with a 6.5 cm radius hole in the center, whose original
1309 function was to reject beam particles slightly offset from the beamline center. Data
1310 from this paddle turned out to be unusable, so our data events include both particle
1311 going through the halo scintillation material or through the halo hole.

1312 3.2.5 LArIAT Cosmic Ray Paddle Detectors

1313 LArIAT triggers both on beam events and on cosmic rays events. We perform this
1314 latter trigger by using two sets of cosmic ray paddle detectors (a.k.a. “cosmic towers”).
1315 The cosmic towers frame the LArIAT cryostat, as one sits in the downstream left
1316 corner and the other sits in the upstream right corner of the cryostat. Two paddle
1317 sets of four scintillators pieces each make up each cosmic tower, an upper set and a
1318 lower set per tower. Of the four paddles, a couple of two matched paddles stands
1319 upright while the a second matched pair lies across the top of the assembly in the top
1320 sets (or across the bottom of the assembly in the bottom sets). The horizontal couple
1321 is used as a veto for particles traveling from inside the TPC out. The four signals
1322 from the vertical paddles along one of the body diagonals of the TPC are combined
1323 in a logical “AND”. This allows to select cosmic muons crossing the TPC along one
1324 of its diagonals. Cosmic ray tracks crossing both anode and cathode populate the
1325 events triggered this way. This particularly useful sample of tracks (which we can
1326 safely assume to be associated with 5 GeV muons) can be used for many tasks; for
1327 example, we use anode-cathode piercing tracks to cross check the TPC electric field
1328 on data (see Appendix A), to calibrate the charge response of the TPC wires for the
1329 full TPC volume and to measure the electron lifetime in the chamber [97].

1330 We retrieved the scintillation paddles from the decommissioning of the CDF de-
1331 tector at Fermilab and we used only the paddles with a counting efficiency greater

1332 than 95% and low noise at working voltage. The measured trigger rate of the whole
1333 system is 0.032 Hz, corresponding to ~ 2 muons per minute.



Figure 3.6: Photograph of one of the scintillation counters used in the cosmic towers.

1334 3.3 In the Cryostat

1335 3.3.1 Cryogenics and Argon Purity

1336 LArIAT repurposed the ArgoNeuT cryostat [16] in order to use it in a beam of charge
1337 particles, and added a new process piping and a new liquid argon filtration system in
1338 FTBF. Inside the LArIAT experimental hall, the cryostat sits on the beam of charge
1339 particles with its horizontal main axis oriented parallel to the beam.

1340 Two volumes make up LArIAT cryostat, shown in Figure 3.7: the inner vessel and
1341 the outer vessel. Purified liquid argon fills the inner vessel, while the outer volume
1342 provides insulation through a vacuum jacket equipped with layers of aluminized mylar
1343 superinsulation. The inner vessel is a cylinder of 130 cm length and 6.2 cm diameter,
1344 containing about 550 L of LAr, corresponding to a mass of 0.76 ton. We run the
1345 signal cables for the LArTPC and the high voltage feedthrough through a “chimney”
1346 at the top and mid-length of the cryostat.

1347 Given the different scopes of the ArgoNeuT and LArIAT detectors, we made

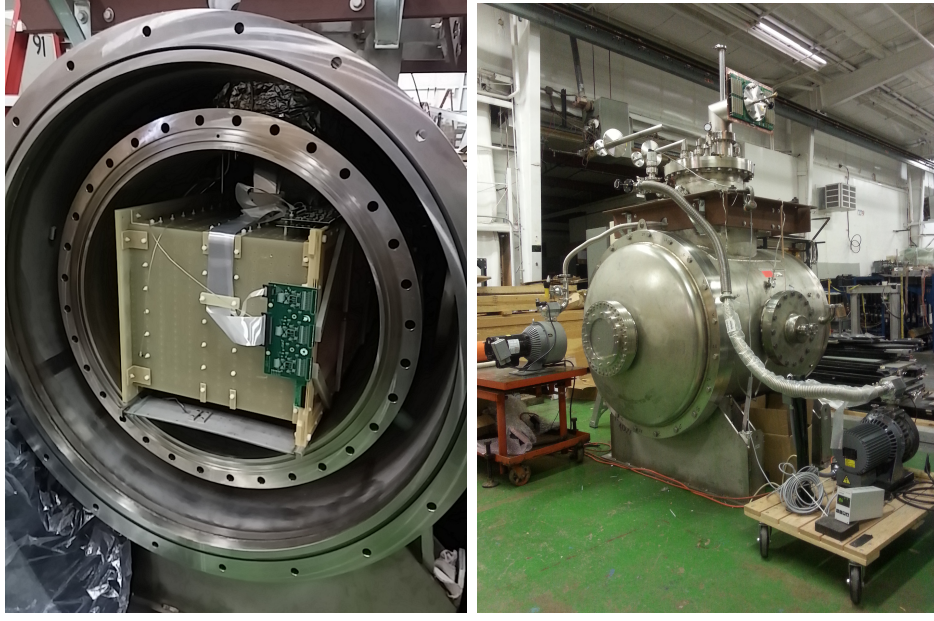


Figure 3.7: Left: the LArIAT TPC in the inner volume of the open cryostat. Right: cryostat fully sealed ready to be transported to FTBF.

1348 several modification to the ArgoNeuT cryostat in order to use it in LArIAT. In par-
 1349 ticular, the modification shown in Figure 3.8 were necessary to account for the beam
 1350 of charged particles entering the TPC and to employ the new FTBT liquid argon
 1351 purification system. We added a “beam window” on the front outer end cap and
 1352 an “excluder” on the inner endcap, with the scope of minimizing the amount of
 1353 non-instrumented material upstream of the TPC’s active volume. The amount of
 1354 non-instrumented material in front of the TPC for LArIAT corresponds to ~ 0.3 elec-
 1355 tron radiation lengths (X_0), to compare against the $\sim 1.6X_0$ of ArgoNeuT. To allow
 1356 studies of the scintillation light, we added a side port feedthrough which enables the
 1357 mounting of the light collection system, as well as the connections for the correspond-
 1358 ing signal and high-voltage cables (see Section 3.3.3). We modified the bottom of the
 1359 cryostat adding Conflat and ISO flange sealing to connect the liquid argon transfer
 1360 line to the new argon cooling and purification system.

1361 As in any other LArTPC, argon purity is a crucial parameter for LArIAT. Indeed,
 1362 the presence of contaminants effects both the basic working principles of a LArTPC,



Figure 3.8: Main modifications to the ArgoNeuT cryostat: 1) outlet for connection to the purification system at the bottom of the cryostat; 2) the “beam-window” on the outer endcap and “excluder” which reduce the amount of non-instrumented material before the TPC; 3) the side port to host the light collection system.

1363 as shown in section 2.1.2: electronegative contaminants such as oxygen and water de-
 1364 crease the number of ionization electrons collected on the wires after drifting through
 1365 the volume. In addition, contaminants such as Nitrogen decrease the light yield
 1366 from scintillation light, especially in its slow component. In LArIAT, contaminations
 1367 should not exceed the level of 100 parts per trillion (ppt). We achieve this level of
 1368 purity in several stages. The specifics required for the commercial argon bought for
 1369 LArIAT are 2 parts per million (ppm) oxygen, 3.5 ppm water, and 10 ppm nitrogen.
 1370 This argon is monitored with the use of commercial gas analyzer. Argon is stored in
 1371 a dewar external to LArIAT hall and filtered before filling the TPC. LArIAT uses a
 1372 filtration system designed for the Liquid Argon Purity Demonstrator (LAPD) [52]:
 1373 half of a 77 liter filter contains a 4A molecular sieve (Sigma-Aldrich [103]) apt to re-
 1374 move mainly water, while the other half contains BASF CU-0226 S, a highly dispersed
 1375 copper oxide impregnated on a high surface area alumina, apt to remove mainly oxy-
 1376 gen [25]. A single pass of argon in the filter is sufficient to achieve the necessary

1377 purity, unless the filter is saturated. In case the filter saturates, the media needs to
1378 be regenerated by using heated gas; this happened twice during the Run II period¹.
1379 The filtered argon reaches the inner vessel via a liquid feedthrough on the top of the
1380 cryostat. Argon is not recirculated in the system; rather, it boils off and vent to
1381 the atmosphere. During data taking, we replenish the argon in the cryostat several
1382 times per day to keep the TPC high voltage feedthrough and cold electronics always
1383 submerged. In fact, we constantly monitor the level, temperature, and pressure of
1384 the argon both in the commercial dewar and inside the cryostat during data taking.

1385 **3.3.2 LArTPC: Charge Collection**

1386 The LArIAT Liquid Argon Time Projection Chamber is a rectangular box of dimen-
1387 sions 47 cm (drift) x 40 cm (height) x 90 cm (length), containing 170 liters of Liquid
1388 Argon. The LArTPC three major subcomponents are

- 1389 1) the cathode and field cage,
1390 2) the wire planes,
1391 3) the read-out electronics.

1392 **Cathode and field cage**

1393 A G10 plain sheet with copper metallization on one of the 40 x 90 cm inner surfaces
1394 forms the cathode. A high-voltage feedthrough on the top of the LArIAT cryostat
1395 delivers the high voltage to the cathode; scope of the high voltage system (Figure 3.9)
1396 is to drift ionization electrons from the interaction of charged particles in the liquid
1397 argon to the wire planes. The power supply used in this system is a Glassman
1398 LX125N16 [65] capable of generating up to -125 kV and 16 mA of current, but

1. We deemed the filter regeneration necessary every time the electron lifetime dropped under 100 μ s.

1399 operated at -23.5kV during LArIAT Run-II. The power supply is connected via high
1400 voltage cables to a series of filter pots before finally reaching the cathode.

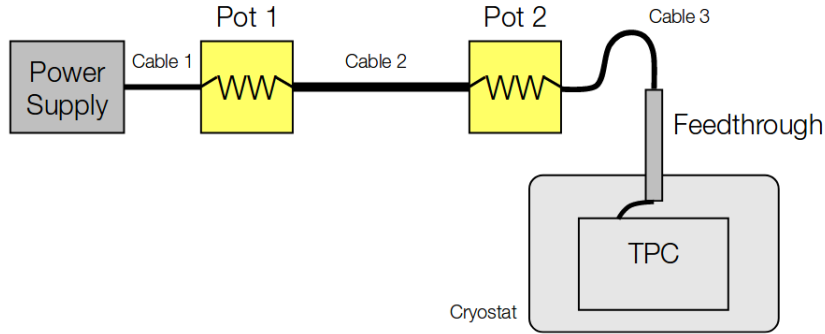


Figure 3.9: Schematic of the LArIAT high voltage system.

1401 The field cage is made of twenty-three parallel copper rings framing the inner walls
1402 of the G10 TPC structure. A network of voltage-dividing resistors connected to the
1403 field cage rings steps down the high voltage from the cathode to form a uniform electric
1404 field. The electric field over the entire TPC drift volume is 486 V/cm, as measured
1405 in appendix A. The maximum drift length, i.e. the distance between cathode and
1406 anode planes, is 47 cm.

1407 Wire planes

1408 LArIAT counts three wire planes separated by 4 mm spaces: in order of increasing
1409 distance from the cathode, they are the shield, the induction and the collection plane.
1410 The “wire pitch”, i.e., the distance between two consecutive wires in a given plane, is
1411 4 mm. The shield plane counts 225 parallel wires of equal length oriented vertically.
1412 This plane is not connected with the read-out electronics; rather it shields the outer
1413 planes from extremely long induction signals due to the ionization chamber in the
1414 whole drift volume. As the shield plane acts almost like a Faraday cage, the shape
1415 of signals in the first instrumented plane (induction) results easier to reconstruct.
1416 Both the induction and collection planes count 240 parallel wires of different length

1417 oriented at 60° from the vertical with opposite signs. Electrons moving past the
1418 induction plane will induce a bipolar pulse on its wires; the drifting electrons will be
1419 then collected on the collection plane's wires, forming a unipolar pulse.

1420 The three wire planes and the cathode form three drift volumes, as shown in Figure
1421 3.10. The main drift volume is defined as the region between the cathode plane and the
1422 shield plane (C-S). The other two drift regions are those between the shield plane and
1423 the induction plane (S-I), and between the induction plane and the collection plane
1424 (I-C). The electric field in these regions is chosen to satisfy the charge transparency
1425 condition and allow for 100% transmission of the drifting electrons through the shield
1426 and the induction planes.

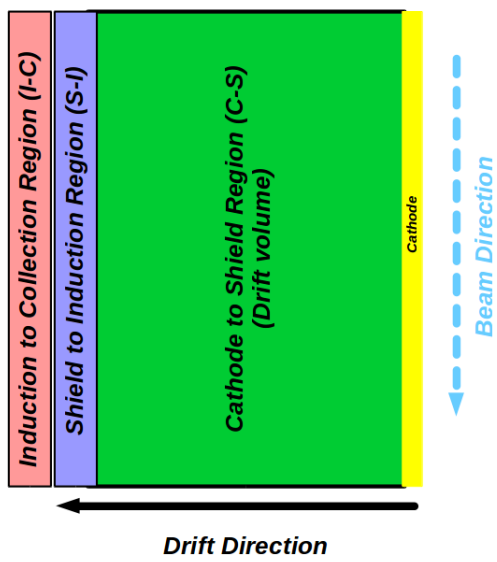


Figure 3.10: Schematic of the three drift regions inside the LArIAT TPC: the main drift volume between the cathode and the shield plane (C-S) in green, the region between the shield plane and the induction plane (S-I) in purple, and the region between the induction plane and the collection plane (I-C) in pink.

1427 Table 3.1 provides the default voltages applied to the cathode and the shield,
1428 induction, and collection plane.

Table 3.1: Cathode and anode planes default voltages

Cathode	Shield	Induction	Collection
-23.17 kV	-298.8 V	-18.5 V	338.5 V

1429 **Electronics**

1430 Dedicated electronics read the induction and collection plane wires, for a total of
1431 480-channel analog signal path from the TPC wires to the signal digitizers. A digital
1432 control system for the TPC-mounted electronics, a power supply, and a distribution
1433 system complete the front-end system. Figure 3.11 shows a block diagram of the
1434 overall system. The direct readout of the ionization electrons in liquid argon forms
1435 typically small signals on the wires, which need amplification in oder to be processed.
1436 LArIAT performs the amplification stage directly in cold with amplifiers mounted on
1437 the TPC frame inside the liquid argon, achieving a remarkable Signal-to-Noise ratio.
1438 The signal from the ASICs are driven to the other end of the readout chain, to the
1439 CAEN V1740 digitizers. The CAEN V1740 has a 12 bit resolution and a maximum
1440 input range of 2 VDC, resulting in about 180 ADC count for a crossing MIP.

1441 **3.3.3 LArTPC: Light Collection System**

1442 The collection of scintillation photons is the second mechanism of particle detection
1443 in argon other than the ionization electrons. Over the course of LArIAT's three years
1444 of data taking, the light collection system changed several times. We describe here
1445 the light collection system for Run II. Two PMTs, a 3-inch diameter Hamamatsu
1446 R-11065 and 2-inch diameter ETL D757KFL [6], as well as three SiPMs arrays (two
1447 Hamamatsu S11828-3344M 4x4 arrays and one single-channel SensL MicroFB-60035)
1448 are mounted on the PEEK support structure. PEEK screws into an access flange
1449 as shown in Figure 3.12, on the anode side, leaving approximately 5 cm of clearance
1450 from the collection plane.

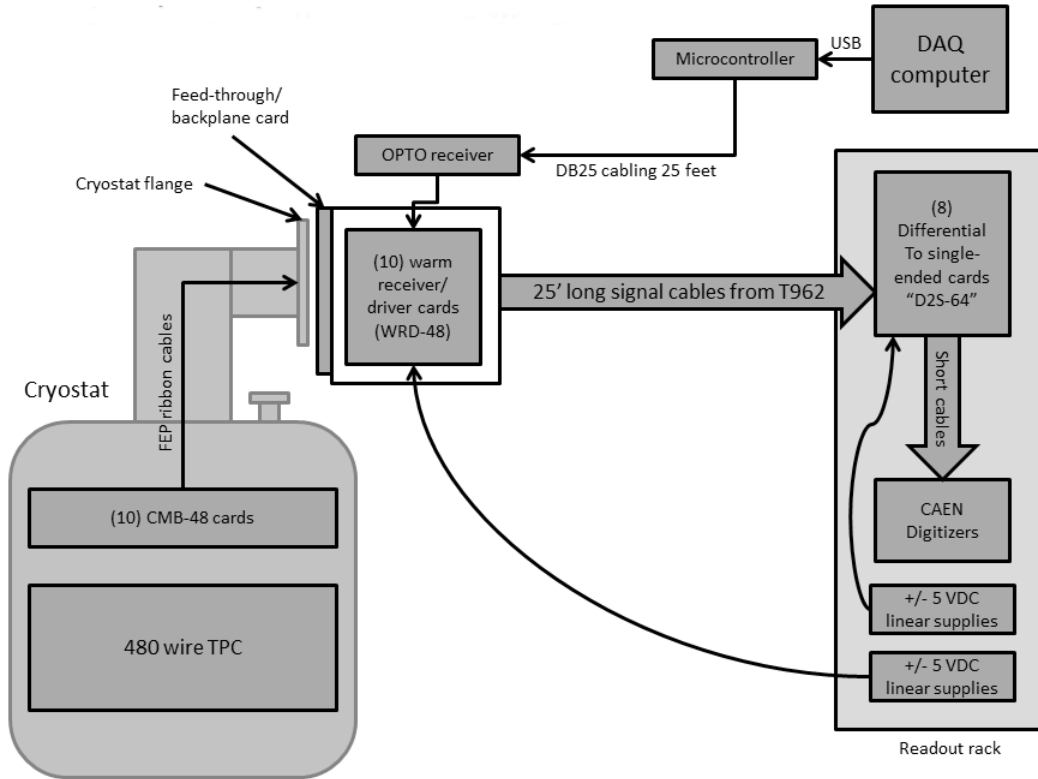


Figure 3.11: Overview of LArIAT Front End electronics.

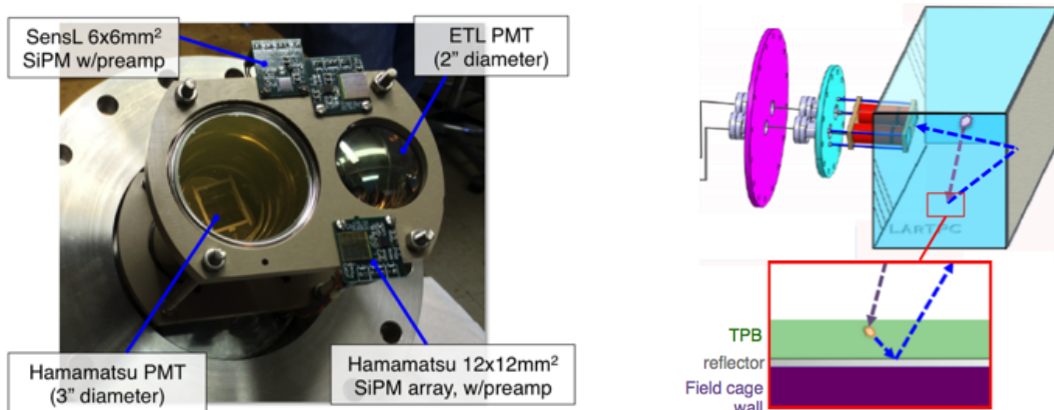


Figure 3.12: LArIAT's photodetector system for observing LAr scintillation light inside the TPC (left), and a simplified schematic of VUV light being wavelength-shifting along the TPB-coated reflecting foils (right).

1451 Liquid argon scintillates in vacuum-ultraviolet (VUV) range at 128 nm; since cryo-
1452 genic PMTs are not sensitive to VUV wavelengths, we need to shift the light in a
1453 region visible to the PMTs. In LArIAT, the wavelength shifting is achieved by in-
1454 stalling highly-reflective VIKUITY dielectric substrate foils coated with a thin layer
1455 of tetraphenyl-butadiene (TPB) on the four unbiased walls of the TPC . The scintil-
1456 lation light interaction with the TPC emits one or more visible photons, we are then
1457 reflected into the chamber. Thus, the light yield increases and results more uniform
1458 across the TPC active volume, allowing the possibility of light-based calorimetry,
1459 currently under study.

1460 For Run II, we coated both the windows of the ETL PMT and SensL SiPM with
1461 a thin layer of TPB. In doing so, some of the VUV scintillation light converts into
1462 visible right at the sensor faces, keeping information on the direction of the light
1463 source. Information about the light directionality is hindered for the light reflected
1464 on foils, as the reflection is uniform in angle.

1465 **3.4 Trigger and DAQ**

1466 The LArIAT DAQ and trigger system governs the read out of all the many subsystems
1467 forming LArIAT. The CAEN V1495 module and its user-programmable FPGA are
1468 the core of this system. Every 10 ns, this module checks for matches between sixteen
1469 logical inputs and user-defined patterns in the trigger menu; if it finds a match for
1470 two consecutive clock ticks, that trigger fires.

1471 LArIAT receives three logic signals from the Fermilab accelerator complex related
1472 to the beam timing which we use as input triggers: a pulse just before the beam, a
1473 pulse indicating beam-on, and a beam-off pulse.

1474 The beam instruments, the cosmic ray taggers, and the light collection system
1475 provide the other NIM-standard logic pulse inputs to the trigger decision. We auto-

1476 matically log the trigger inputs configuration with the rest of the DAQ configuration
1477 at the beginning of each run.

1478 Fundamental inputs to the trigger card come from the TOF (see section 3.2.3)
1479 and the wire chambers (see section 3.2.2), as activity in these systems points to the
1480 presence of a charged particle in tertiary beam line. In particular, the discriminated
1481 pulses from the TOF PMTs form a NIM logic pulse for the trigger logic. We ask for
1482 a coincidence within a 20 ns window for all the pulses from the PMTs looking at the
1483 same scintillator block and use the coincidence between the upstream and downstream
1484 paddle to inform the trigger decision. In order to form a coincidence between the
1485 upstream and downstream paddles, we delay the upstream paddle coincidence by
1486 20 ns and widen it by 100 ns. The delay and widening are necessary to account for
1487 both lightspeed particles and slower particles (high-mass) to travel the 6.5 m between
1488 the upstream and the downstream paddles. For the read out of the wire chambers,
1489 we use a total of sixteen multi-hit TDCs, four per chamber: two TDC per plane
1490 (horizontal and vertical), sixty-four wires per TDC. In each TDC, we keep the logical
1491 “OR” for any signal over threshold from the sixty-four wires. We then require a
1492 coincidence between the “OR” for the horizontal TDCs and the “OR” for the vertical
1493 TDCs: with this logic we make sure that at least one horizontal wire and one vertical
1494 wire saw significant signal in one wire chamber. The single logical pulse from each of
1495 the four wire chambers feeds into the first four inputs to the V1495 trigger card. We
1496 require a coincidence within 20 ns of at least three logical inputs to form a trigger.

1497 The cosmic towers (see Section 3.2.5) provide another primary input to the trigger,
1498 in order to capture long tracks from cosmic muons crossing the TPC. We use NIM
1499 modules to require coincidences between one upper and one lower paddle set of any
1500 opposite cosmic towers. The OR all the opposite towers’ coincidences is fed as an
1501 input to the trigger card.

1502 We use the signal from the cryogenic PMTs (see Section 3.3.3) to form several

1503 interesting triggers. The coincidence of signal from all the PMT pulses within \sim 20 ns
1504 is an indication of ionizing radiation in the TPC and forms a trigger input. The
1505 coincidence of two subsequent scintillation logic pulses delayed by a maximum of 7 μ s
1506 forms the Michel electron trigger.

1507 3.5 Control Systems

1508 LArIAT is a complex ensemble of systems which needed to be monitored at once
1509 during data taking. We performed the monitoring of the systems operations with a
1510 slow control system, a DAQ monitoring system and a low level data quality monitoring
1511 described in the following sections.

1512 Slow Control

1513 We used the Synoptic Java Web Start framework as a real-time display of subsystem
1514 conditions. Its simple Graphical User Interface allowed us to change the operating
1515 parameters and to graph the trends of several variables of interest for all the tertiary
1516 beam detectors. Among the most important quantities monitored by Synoptic there
1517 are the level of argon in both the inner vessel and the external dewar, the operating
1518 voltages of cathode and wire planes, of the PMTs and SiPMs, and of the four wire
1519 chambers, as well as the magnets temperature. Figure 3.13 shows an example of the
1520 monitoring system. LArIAT uses the Accelerator Control NETwork system (ACNET)
1521 to monitor the beam conditions of the MCenter beamline. For example, the horizontal
1522 and vertical position of the beam at the first two wire chambers (WC1 and WC2) are
1523 shown in 3.14 as seen by the shifter during data taking.

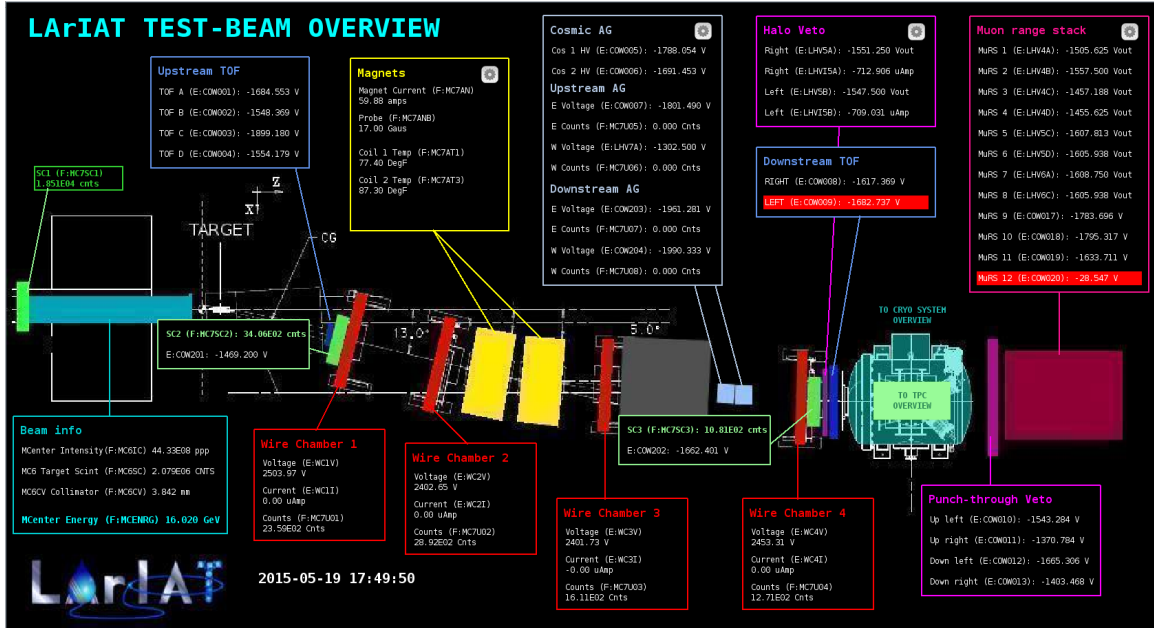


Figure 3.13: Interface of the Synoptic slow control system

1524 DAQ Monitoring

1525 We monitor the data taking and the run time evolution with the Run Status Webpage
 1526 (<http://lariat-wbm.fnal.gov/lariat/run.html>), a webpage updated in real-time. The
 1527 page displays, among other information, the total number of triggers in the event,
 1528 the total number of detectors triggered during a beam spill, the trigger patterns, the
 1529 number of times a particular trigger pattern was satisfied during a beam spill, and
 1530 the current time relative to the Fermilab accelerator complex supercycle. A screen
 1531 shot of the page is show in figure 3.15.

1532 Data Quality Monitoring

1533 We employ two systems to ensure the quality of our data during data taking: the
 1534 Near-Real-Time Data Quality Monitoring and the Event Viewer.

1535 The Near-Real-Time Data Quality Monitoring (DQM) is a webpage which receives
 1536 updates from all the VME boards in the trigger system and displays the results of
 1537 a quick analysis of the DAQ stream of raw data on a spill-by-spill basis. The DQM

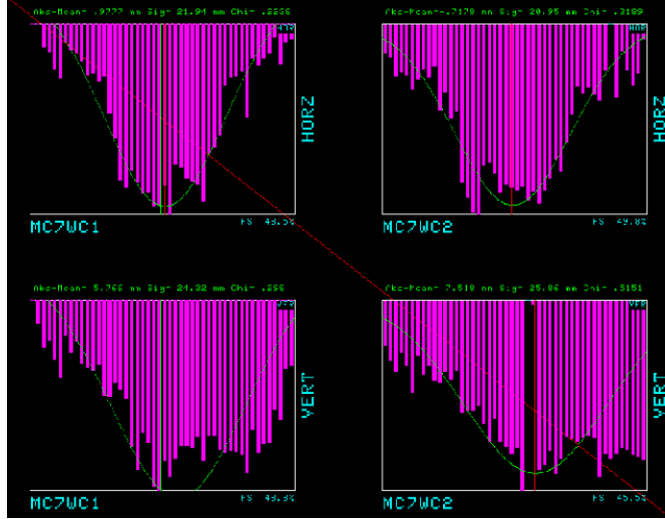


Figure 3.14: Beam position at the upstream wire chambers monitored with ACNET.

1538 allows the shifter to monitor almost in real time (typically with a 2-minute delay)
 1539 a series of low level-quantities and compare them to past collections of beam spills.
 1540 Some of the variables monitored in the DQM are the pedestal mean and RMS on
 1541 CAEN digitizer boards of the TPC wires and PMTs of the beamline detectors, the
 1542 hit occupancy and timing plots on the wire chambers, and number of data fragments
 1543 recorded that are used to build a TPC event. Abnormal values for low-level quantity
 1544 in the data activate a series of alarms in the DQM; this quick feedback on the DAQ
 1545 and beam conditions is fundamental to assure a fast debugging of the detector and a
 1546 very efficient data taking during beam uptime.

1547 The online Event Viewer displays a two dimensional representation (Wire vs Time)
 1548 of LArIAT TPC events on both the Induction and the Collection planes in near real
 1549 time. The raw pulses collected by the DAQ on each wire are plotted as a function of
 1550 drift time, resulting in an image of the TPC event easily readable by the shifter. This
 1551 tool guarantees a particularly good check of the TPC operation which activate an
 1552 immediate feedback for troubleshooting a number of issues. For example, it easy for
 1553 the shifter to spot high occupancy events and request a reduction of the primary beam
 1554 intensity, or to spot a decrease of the argon purity which requires the regeneration of

₁₅₅₅ filters, or to catch the presence of electronic noise and reboot the ASICs. An example
₁₅₅₆ of high occupancy event is shown in 3.16.

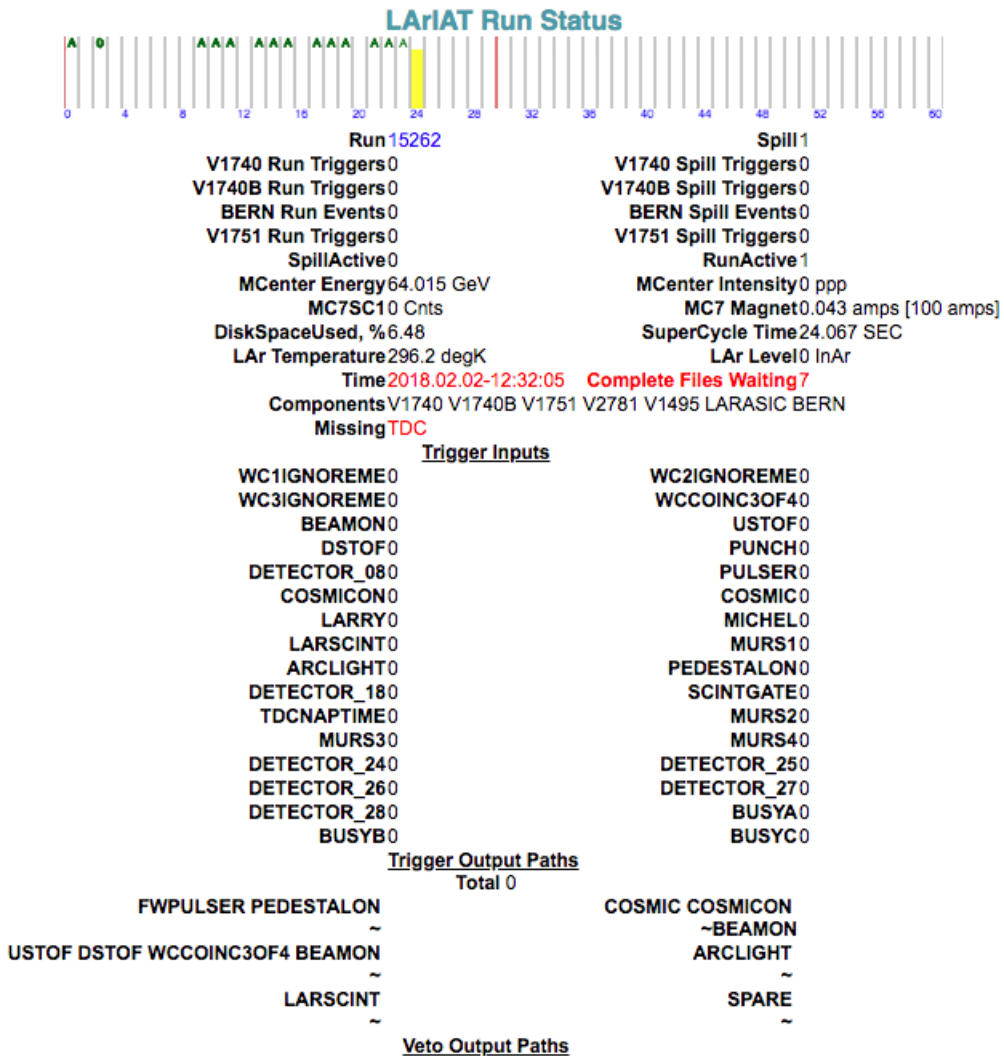


Figure 3.15: Run Status page at LArIAT downtime. At the top the yellow bar displays the current position in the Fermilab supercycle. Interesting information to be monitored by the shifter were the run number and number of spills, time elapsed from data taking (here in red), the energy of the secondary beam and the trigger paths.

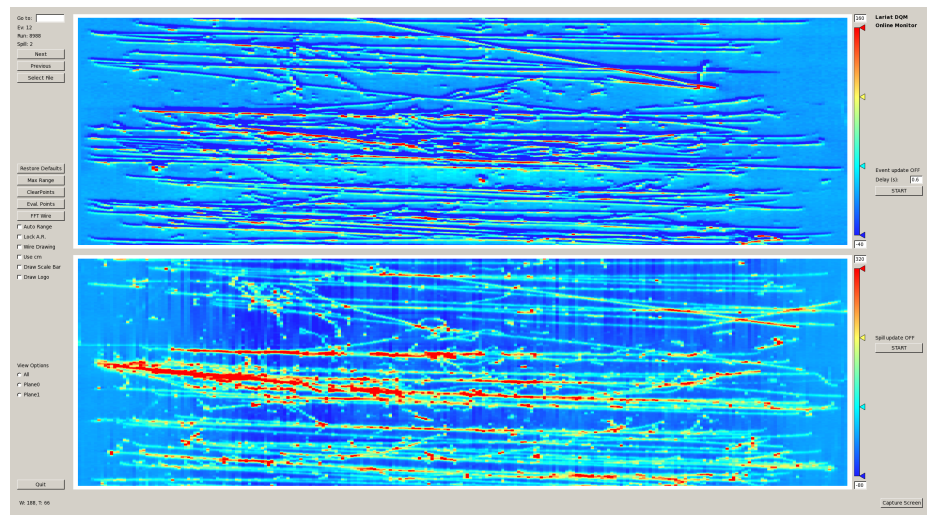


Figure 3.16: High occupancy event display: induction plane (top) and collection plane (bottom).

1557 **Chapter 4**

1558 **Total Hadronic Cross Section**

1559 **Measurement Methodology**

1560 **4.1 How to Measure a Hadron Cross Section in
1561 LArIAT**

1562 We use both the LArIAT beamline detectors and the LArTPC information to measure
1563 the total hadronic cross sections in argon. Albeit with small differences, both the π^- -
1564 Ar and K^+ - Ar total hadronic cross section measurements rely on the same procedure
1565 described in details in the following paragraphs: we select the particle of interest
1566 using a combination of beamline detectors and TPC information (paragraph 4.1.1),
1567 we perform a handshake between the beamline information and the TPC tracking to
1568 assure we are selecting the right TPC track (paragraph 4.1.2), and we apply the “thin
1569 slice” method to get to the final result (paragraph 4.1.3). At the end of this chapter,
1570 we show a cross check of this method against MC truth information (paragraph 4.1.4).

1571 **4.1.1 Event Selection**

1572 **Beamline events**

1573 As will be clear in paragraph 4.1.3, beamline particle identification and momentum
1574 measurement before entering the TPC are fundamental information for the hadronic
1575 cross sections measurements in LArIAT. Thus, we scan the LArIAT data to keep only
1576 events whose wire chamber and time of flight information is registered. Additionally,
1577 we perform a check of the plausibility of the trajectory inside the beamline detectors:
1578 given the position of the hits in the four wire chambers, we make sure the particle
1579 trajectory does not cross any impenetrable material such as the collimator and the
1580 magnets steel.

1581 **Particle Identification in the beamline**

1582 In data, the main tool to establish the identity of the hadron of interest is the LArIAT
1583 tertiary beamline, in its function of mass spectrometer. We combine the measurement
1584 of the time of flight, TOF , and the beamline momentum, p_{Beam} , to reconstruct the
1585 invariant mass of the particles in the beamline, m_{Beam} , as follows

$$m_{Beam} = \frac{p_{Beam}}{c} \sqrt{\left(\frac{TOF * c}{l}\right)^2 - 1}, \quad (4.1)$$

1586 where c is the speed of light and l is the length of the particle trajectory between the
1587 time of flight paddles.

1588 Figure 4.1 shows the mass distribution for the Run II negative polarity runs on
1589 the left and positive polarity runs on the right. We perform the classification of events
1590 into the different samples as follows:

1591 • π, μ, e : $0 \text{ MeV} < \text{mass} < 350 \text{ MeV}$

1592 • kaon: $350 \text{ MeV} < \text{mass} < 650 \text{ MeV}$

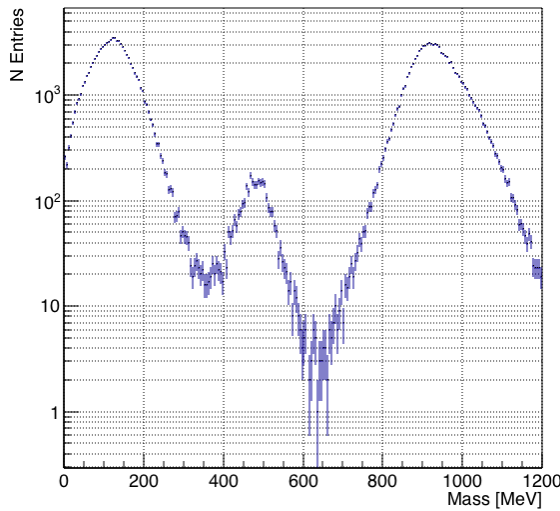


Figure 4.1: The mass plotted for a sample of Run-II events reconstructed in the beamline, negative polarity runs on the left and positive polarity runs on the right. The classification of the events into π , μ , e , kaon, or proton is based on this distribution.[CHANGE PLOTS](#)

- 1593 • proton: $650 \text{ MeV} < \text{mass} < 3000 \text{ MeV}$.

1594 **Additional Particle Identification technique**

1595 In the case of the π^- -Ar cross section, the resolution of beamline mass spectrometer is
 1596 not sufficient to select a beam of pure pions. In fact, muons and electrons survive the
 1597 selection on the beamline mass value. It is important to notice that the composition
 1598 of the negative polarity beam is mostly pions, as discussed in section 6.1.1. Anyhow,
 1599 we devise a selection on the TPC information to mitigate the presence of electrons
 1600 in the sample used for the pion cross section. The selection relies on the different
 1601 topologies of a pion and an electron event in the argon: while the former will trace
 1602 a track inside the TPC active volume, the latter will tend to “shower”, i.e. interact
 1603 with the medium, produce bremsstrahlung photons which pair convert into several
 1604 short tracks.

1605 **Pile up mitigation**

1606 The secondary beam impinging on LArIAT secondary target produces a plethora
1607 of particles. The presence of upstream and downstream collimators greatly abates
1608 the number of particles tracing down the LArIAT beamline. However, more than one
1609 beamline particles, or particles produced from the beam interaction with the beamline
1610 detectors, may sneak into the LArTPC during its readout time. The TPC readout
1611 is triggered by the actual particle firing the beamline detectors; we call “pile up”
1612 the additional traces in the TPC. We adjusted the primary beam intensity between
1613 LArIAT Run I and Run II to minimize the presence of events with high pile up
1614 particles in the data sample. For the cross section analyses, we remove events with
1615 more than 4 tracks in the first 14 cm upstream portion of the TPC from the sample.

1616 **4.1.2 Wire Chamber to TPC Match**

1617 For each event passing the selection on its beamline information we need to identify
1618 the track inside the TPC corresponding to the particle which triggered the beamline
1619 detectors, a procedure we refer to as “WC to TPC match” (WC2TPC for short).
1620 In general, the TPC tracking algorithm will reconstruct more than one track in the
1621 event, partially due to the fact that hadrons interact in the chamber and partially
1622 because of pile up particles during the triggered TPC drift time, as shown in figure

1623 **4.2. ADD EVENT DISPLAYS**

1624 We attempt to uniquely match one wire chamber track to one and only one re-
1625 constructed TPC track. In data, this match leverages on a geometrical selection
1626 exploiting both the position of the wire chamber and TPC tracks, and the angle
1627 between them. We consider only TPC tracks whose first point is in the first 2 cm up-
1628 stream portion of the TPC for the match. We project the wire chamber track to the
1629 TPC front face where we define the x_{FF} and y_{FF} coordinates used for evaluating the
1630 match. We define ΔX as the difference between the x position of the most upstream



Figure 4.2: Kaon candidate event: on the right, event display showing raw quantities; on the left, event display showing reconstructed tracks. In the reconstructed event display, different colors represent different track objects. A kink is visible in the kaon ionization, signature of a hadronic interaction: the tracking correctly stops at the kink position and two tracks are formed. An additional pile-up track is so present in the event (top track).

1631 point of the TPC track and x_{FF} . ΔY is defined analogously. We define the radius
1632 difference, ΔR , as $\Delta R = \sqrt{\Delta X^2 + \Delta Y^2}$. The angle between the incident WC track
1633 and the TPC track in the plane that contains them defines α . If $\Delta R < 4$ cm, $\alpha < 8^\circ$,
1634 a match between WC-track and TPC reconstructed track is found. We describe how
1635 we determinate the best value for the radius and angular selection in sec 5.4.1. In
1636 MC, we mimic the matching between the WC and the TPC track by constructing
1637 a fake WC track using truth information at wire chamber four. We then apply the
1638 same WC to TPC matching algorithm as in data. We discard events with multi-
1639 ple WC2TPC matches. We use only TPC track matched to WC tracks in the cross
1640 section calculation.

1641 **4.1.3 The Thin Slice Method**

1642 **Cross Sections on Thin Target**

1643 Cross section measurements on a thin target have been the bread and butter of
1644 nuclear and particle experimentalists since the Geiger-Marsden experiments [62]. At
1645 their core, this type of experiments consists in shooting a beam of particles with a
1646 known flux on a thin target and recording the outgoing flux.

1647 In general, the target is not a single particle, but rather a slab of material con-
1648 taining many diffusion centers. The so-called “thin target” approximation assumes
1649 that the target centers are uniformly distributed in the material and that the target is
1650 thin compared to the interaction length so that no center of interaction sits in front of
1651 another. In this approximation, the ratio between the number of particles interacting
1652 in the target $N_{Interacting}$ and number of incident particles $N_{Incident}$ determines the
1653 interaction probability $P_{Interacting}$, which is the complementary to one of the survival
1654 probability $P_{Survival}$. Equation 4.2

$$P_{Survival} = 1 - P_{Interacting} = 1 - \frac{N_{Interacting}}{N_{Incident}} = e^{-\sigma_{TOT} n \delta X} \quad (4.2)$$

1655 describes the probability for a particle to survive the thin target. This formula relates
1656 the total cross section σ_{TOT} , the density of the target centers n and the thickness of
1657 the target along the incident hadron direction δX , to the interaction probability¹.
1658 If the target is thin compared to the interaction length of the process considered,
1659 we can Taylor expand the exponential function in equation 4.2 and find a simple
1660 proportionality relationship between the number of incident and interacting particles,

1. The scattering center density in the target, n , relates to the argon density ρ , the Avogadro number N_A and the argon molar mass m_A as $n = \frac{\rho N_A}{m_A}$.

1661 and the cross section, as shown in equation 4.3:

$$1 - \frac{N_{\text{Interacting}}}{N_{\text{Incident}}} = 1 - \sigma_{\text{TOT}} n \delta X + O(\delta X^2). \quad (4.3)$$

1662 Solving for the cross section, we find:

$$\sigma_{\text{TOT}} = \frac{1}{n \delta X} \frac{N_{\text{Interacting}}}{N_{\text{Incident}}}. \quad (4.4)$$

1663 Not-so-Thin Target: Slicing the Argon

1664 The LArIAT TPC, with its 90 cm of length, is not a thin target. However, the fine-
1665 grained tracking of the LArIAT LArTPC allows us to treat the argon volume as a
1666 sequence of many adjacent thin targets.

1667 As described in Chapter 3, LArIAT wire planes count 240 wires each. The wires
1668 are oriented at +/- 60° from the vertical direction at 4 mm spacing, while the beam
1669 direction is oriented 3 degrees off the z axis in the XZ plane. The wires collect signals
1670 proportional to the energy loss of the hadron along its path in a $\delta X = 4 \text{ mm}/\sin(60^\circ)$
1671 $\approx 4.7 \text{ mm}$ slab of liquid argon. Thus, one can think to slice the TPC into many thin
1672 targets of $\delta X = 4.7 \text{ mm}$ thickness along the direction of the incident particle.

1673 Considering each slice j a “thin target”, we can apply the cross section calculation
1674 from Eq. 4.4 iteratively, evaluating the kinetic energy of the hadron as it enters each
1675 slice, E_j^{kin} . For each WC-to-TPC matched particle, the energy of the hadron entering
1676 the TPC is known thanks to the momentum and mass determination by the tertiary
1677 beamline,

$$E_{\text{FrontFace}}^{\text{kin}} = \sqrt{p_{\text{Beam}}^2 - m_{\text{Beam}}^2} - m_{\text{Beam}} - E_{\text{loss}}, \quad (4.5)$$

1678 where E_{loss} is a correction for the energy loss in the dead material between the
1679 beamline and the TPC front face. The energy of the hadron at the each slab is

1680 determined by subtracting the energy released by the particle in the previous slabs.

1681 For example, at the j^{th} point of a track, the kinetic energy will be

$$E_j^{kin} = E_{FrontFace}^{kin} - \sum_{i < j} \Delta E_i, \quad (4.6)$$

1682 where ΔE_i is the energy deposited at each argon slice before the j^{th} point as measured
1683 by the calorimetry associated with the tracking.

1684 If the particle enters a slice, it contributes to $N_{Incident}(E^{kin})$ in the energy bin
1685 corresponding to its kinetic energy in that slice. If it interacts in the slice, it then
1686 also contributes to $N_{Interacting}(E^{kin})$ in the appropriate energy bin. The cross section
1687 as a function of kinetic energy, $\sigma_{TOT}(E^{kin})$ will then be proportional to the ratio
1688 $\frac{N_{Interacting}(E^{kin})}{N_{Incident}(E^{kin})}$.

1689 The statistical uncertainty for each energy bin is calculated by error propagation
1690 from the statistical uncertainty on $N_{Incident}$ and $N_{Interacting}$. Since the number of
1691 incident hadrons in each energy bin is given by a simple counting, we assume that
1692 $N_{Incident}$ is distributed as a poissonian with mean and σ^2 equal to $N_{Incident}$ in each
1693 bin. On the other hand, $N_{Interacting}$ follows a binomial distribution: a particle in a
1694 given energy bin might or might not interact. The square of the variance for the
1695 binomial is given by

$$\sigma^2 = \mathcal{N} P_{Interacting} (1 - P_{Interacting}); \quad (4.7)$$

1696 since the interaction probability $P_{Interacting}$ is $\frac{N_{Interacting}}{N_{Incident}}$ and the number of tries
1697 \mathcal{N} is $N_{Incident}$, equation 4.7 translates into

$$\sigma^2 = N_{Incident} \frac{N_{Interacting}}{N_{Incident}} \left(1 - \frac{N_{Interacting}}{N_{Incident}}\right) = N_{Interacting} \left(1 - \frac{N_{Interacting}}{N_{Incident}}\right). \quad (4.8)$$

1698 $N_{Incident}$ and $N_{Interacting}$ are not independent. The uncertainty on the cross section

1699 is thus calculated as

$$\delta\sigma_{tot}(E) = \sigma_{tot}(E) \left(\frac{\delta N_{Interacting}}{N_{Interacting}} + \frac{\delta N_{Incident}}{N_{Incident}} \right) \quad (4.9)$$

1700 where:

$$\delta N_{Incident} = \sqrt{N_{Incident}} \quad (4.10)$$

$$\delta N_{Interacting} = \sqrt{N_{Interacting} \left(1 - \frac{N_{Interacting}}{N_{Incident}} \right)}. \quad (4.11)$$

1701 4.1.4 Procedure testing with truth quantities

1702 The π^- -Ar and K^+ -Ar total hadronic cross section implemented in Geant4 can be
1703 used as a tool to validate the measurement methodology. We describe here a closure
1704 test done on Monte Carlo to prove that the methodology of slicing the TPC retrieves
1705 the underlying cross section distribution implemented in Geant4 within the statistical
1706 uncertainty.

1707 For pions in the considered energy range, the Geant4 inelastic model adopted to
1708 is “BertiniCascade”, while the elastic model “hElasticLHEP”. For kaons, the Geant4
1709 inelastic model adopted to is “BertiniCascade”, while the elastic model “hElasti-
1710 cLHEP”.

1711 For the validation test, we fire about 390000 pions and 140000 kaons inside the
1712 LArIAT TPC active volume using the Data Driven Monte Carlo (see section 5.2.2).
1713 We apply the thin-sliced method using only true quantities to calculate the hadron
1714 kinetic energy at each slab in order to decouple reconstruction effects to eventual
1715 issues with the methodology. For each slab of 4.7 mm length on the path of the
1716 hadron, we integrate the true energy deposition as given by the Geant4 transportation
1717 model. Then, we recursively subtracted it from the hadron kinetic energy at the TPC
1718 front face to evaluate the kinetic energy at each slab until the true interaction point

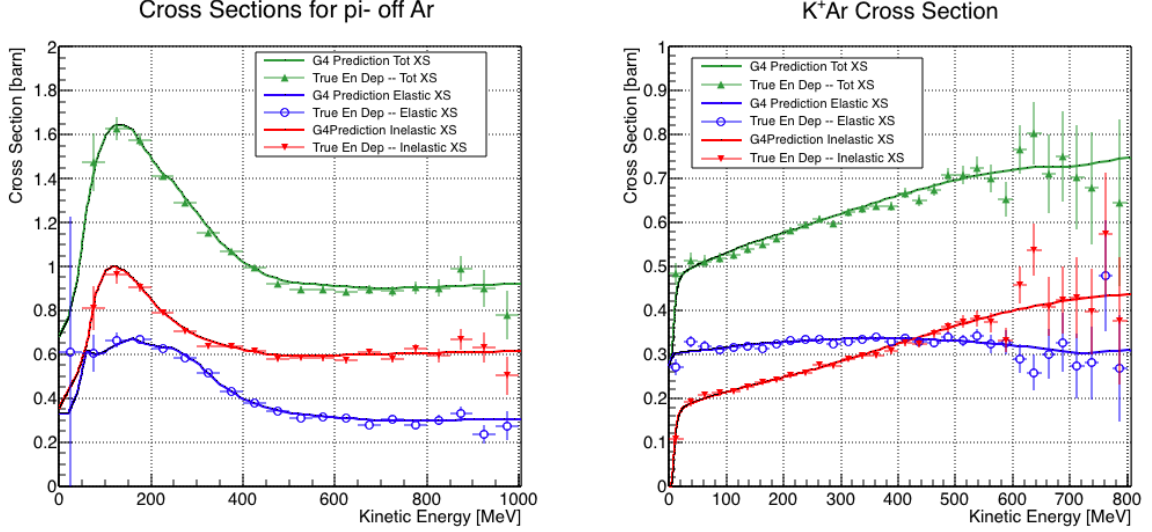


Figure 4.3: Hadronic cross sections for π^- -Ar (left) and K^+ -Ar (right) implemented in Geant4 10.01.p3 (solid lines) overlaid the true MC cross section as obtained with the sliced TPC method (markers). The total cross section is shown in green, the elastic cross section in blue and the inelastic cross section in red.

1719 is reached. Doing so, we obtain the true interacting and incident distributions for
 1720 the considered hadron and we obtain the true MC cross section as a function of the
 1721 hadron true kinetic energy.

1722 Figure 4.3 shows the total hadronic cross section for argon implemented in Geant4
 1723 10.01.p3 (solid lines) overlaid with the true MC cross section as obtained with the
 1724 sliced TPC method (markers) for pions on the left and kaons on the right; the total
 1725 cross section is shown in green, the elastic cross section in blue and the inelastic
 1726 cross section in red. The nice agreement with the Geant4 distribution and the cross
 1727 section obtained with the sliced TPC method gives us confidence in the validity of
 1728 the methodology.

¹⁷²⁹ **Chapter 5**

¹⁷³⁰ **Samples Preparation**

¹⁷³¹ This chapter describes the preparation of the data and Monte Carlo samples used for
¹⁷³² the cross section analyses. This entails:

¹⁷³³ 1. the beamline event selection on data,

¹⁷³⁴ 2. the MC production,

¹⁷³⁵ 3. the energy calibration of the detector both in data and MC,

¹⁷³⁶ 4. the optimization of the tracking algorithm for the total cross section analyses.

¹⁷³⁷ **5.1 LArIAT Data**

¹⁷³⁸ **5.2 LArIAT Monte Carlo**

¹⁷³⁹ For the simulation of LArIAT events and their particle make up, we use a combination
¹⁷⁴⁰ of two MC generators: the G4Beamline Monte Carlo and the Data Driven single
¹⁷⁴¹ particle Monte Carlo (DDMC). We use the G4Beamline MC to simulate the particle
¹⁷⁴² transportation in the beamline and calculate the particle composition of the beam just

1743 past the fourth Wire Chamber (WC4). In order to simulate the beam line particles
1744 after WC4 and in the TPC, we use the DDMC.

1745 5.2.1 G4Beamline

1746 G4Beamline simulates the beam collision with the LArIAT secondary target, the
1747 energy deposited by the particles in the LArIAT beamline detectors and the action
1748 of the LArIAT magnets, effectively accounting for particle transportation through
1749 the beam line from the LArIAT target until “Big Disk”, a fictional, void detector
1750 located just before the cryostat. At the moment of this writing, G4Beamline does
1751 not simulated the responses of the beam line detectors. It is possible to interrogate
1752 the truth level information of the simulated particles in several points of the geometry.
1753 In order to ease the handshake between G4Beamline and the DDMC, we ask for the
1754 beam composition just after WC4. Since LArIAT data are taken under different
1755 beam conditions, G4Beamline simulates separately the beam composition according
1756 to the magnets’ settings and the secondary beam intensity. For the pion cross section
1757 analysis the relevant beam conditions are secondary beam energy of 64 GeV, negative
1758 polarity magnet with current of 100 A and 60 A. For the kaon cross section analysis
1759 the relevant beam conditions is a secondary beam energy of 64 GeV, positive polarity
1760 magnet with current of 100 A.

1761 DECIDE IF YOU WANT THE BEAM COMPOSITION HERE

1762 5.2.2 Data Driven MC

1763 The Data Driven single particle Monte Carlo (DDMC) is a single particle MC gun
1764 which simulates the particle transportation from WC4 into the TPC leveraging on
1765 the beamline data information. The DDMC uses the data momentum and position
1766 at WC4 to derive its initial conditions: a general sketch of the DDMC workflow is
1767 shown in Figure 5.1.

When producing a DDMC sample, beam line data from a particular running period and/or running condition are selected first. Figure 5.2 schematically shows the data quantities of interest leveraged from data: the momentum (P_x, P_y, P_z) and position (X, Y) at WC4. For each data event, we obtain the particle position (X, Y) at WC4 directly from the data measurement. On the contrary, we calculate the components of the momentum using the beamline measurement of the momentum magnitude (see section 3.2.2) in conjunction with the hits on WC3 and WC4 to determine the direction of the momentum vector, as described in 3.2.2. The momentum and position of the selected data is sampled thousand of times through a 5-dimensional hit-or-miss sampling procedure. This produces MC distributions with the same momentum and position distributions as data, with the additional benefit of accounting for the correlations between the considered variables. A LArSoft simulation module then launches single particle MC from $z = -100$ cm (the location of the WC4) using the sampled momentum and position distributions as a template. As an example, the results of the DDMC generation compared to data for the pion 60A sample are shown in figure ??; as expected, MC and data agree within the statistical uncertainty by construction. Using this technique ensures the MC and data particles have very similar momentum, position and angular distributions at WC4 and allow us to use the MC sample in several occasions, for example to calibrate the energy loss upstream of the TPC or account for the WC2TPC match inefficiency. A small caveat is in order here: the DDMC is a single particle Monte Carlo, which means that the beam pile-up is not simulated. Three sample of **NUMBERS** pions, muons and electrons, as well as a sample of **NUMBERS** kaons have been generated with the DDMC and are used for the MC cross section study.

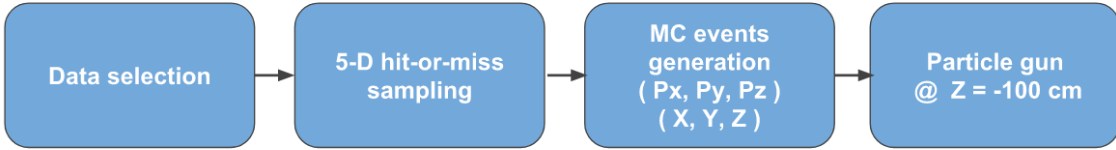


Figure 5.1: Workflow for Data Driven single particle Monte Carlo production.

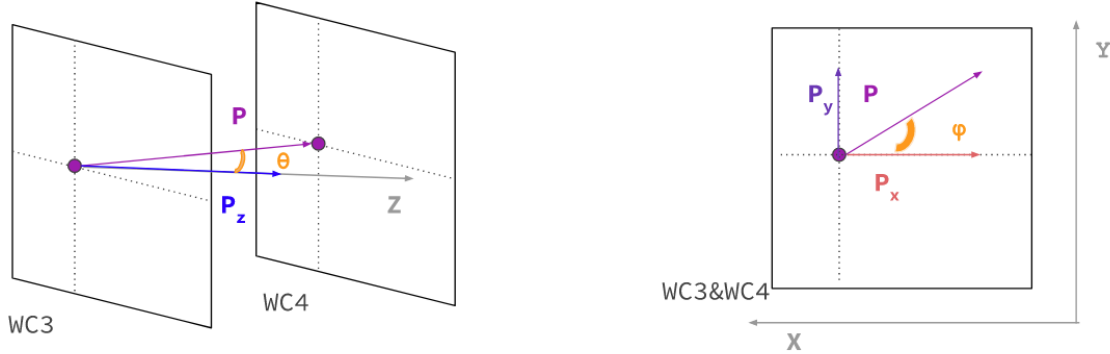


Figure 5.2: Scheme of the quantities of interest for the DDMC event generation: P_x, P_y, P_z, X, Y at WC4.

1792 5.3 Energy Calibration

1793 Scope of the energy calibration is to identify the factors which convert the charge
1794 collected (dQ) to energy deposited in the chamber(dE). As described in section 2.1.5,
1795 this is a multi-step procedure. In LArIAT, we first correct the raw charge by the
1796 electronic noise on the considered wire [?], then by the electron life time [?], and then
1797 by the recombination effect using the ArgoNeut recombination values. Lastly, we
1798 apply overall calibration of the energy, i.e. we determine the “calorimetry constants”
1799 using the procedure described in this paragraph.

1800 The general idea is to use a parametrization of the energy deposited per unit length
1801 (dE/dX) as a function of momentum to independently determine the calorimetry
1802 constants for the data and Monte Carlo in the LArIAT Run-II data samples. This is
1803 done by comparing the stopping power measured on reconstructed quantities against
1804 the Bethe-Bloch theoretical prediction for various particle species.

Momentum Z Component

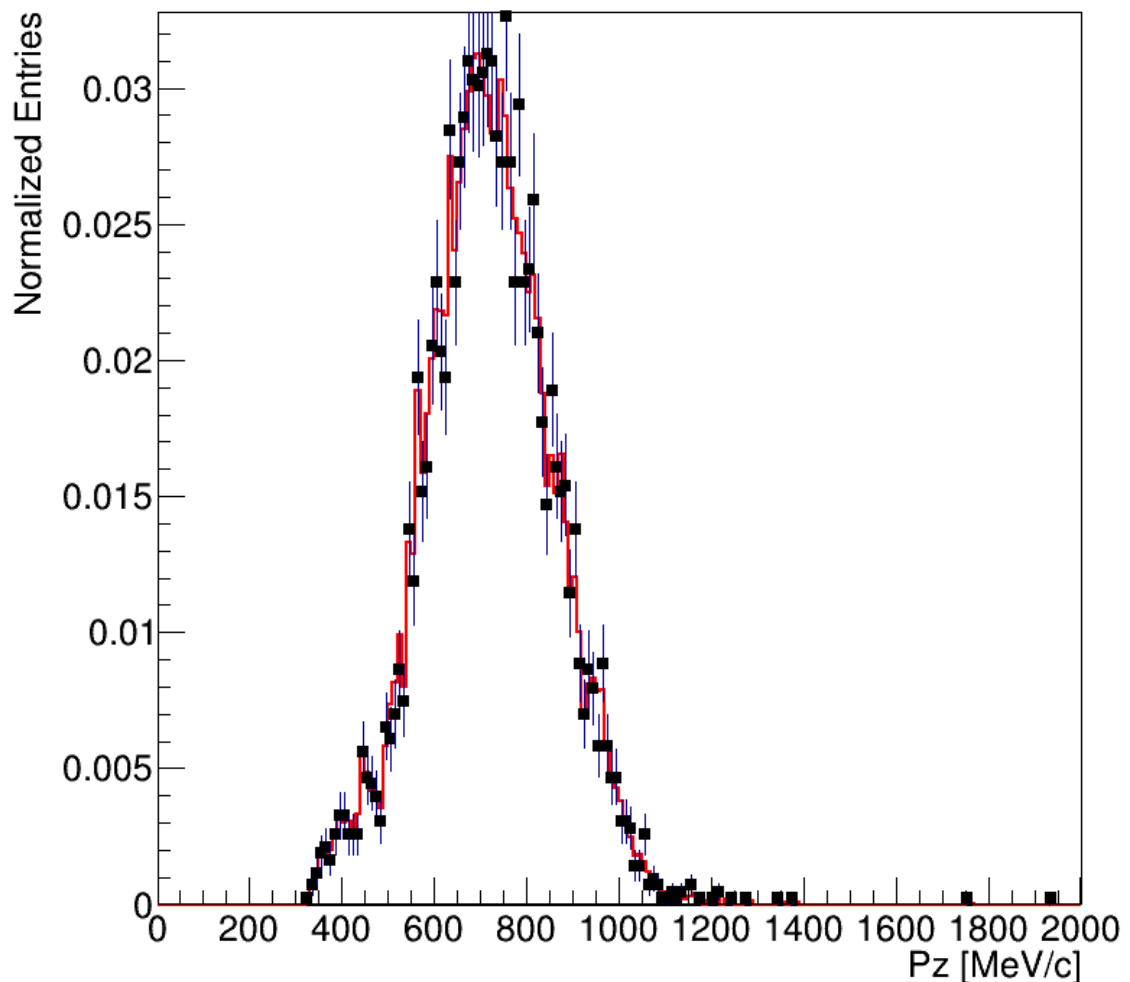


Figure 5.3: Comparison between generated quantities and data distributions for the 60A pion sample: Z component of the momentum (top left), X position at Wire Chamber 4 (top right), Y position at Wire Chamber 4 (bottom).

1805 This is best represented by Figure 5.4, taken from the Particle Data Group [?].
1806 Using the tables provided by the PDG for liquid argon ([?]), we calculate the theo-
1807 retical values for the most probably value for the stopping power of pions (π), muons
1808 (μ), kaons (K), and protons (p) in the momentum range most relevant for LArIAT,
1809 shown in Figure 5.5.

Figure 5.4: Mean energy loss in various materials over a range of particle momenta as produced in Reference [?].

Figure 5.5: Mean energy loss for pions, muons, and protons in liquid argon over the momentum range most relevant for LArIAT.

1810 Using the predictions in Figure 5.5, allows us to tune the calorimetry constants.
1811 The goal is to have the data and the Bethe-Bloch prediction agree across the broad
1812 range of momentum.

1813 The basic idea of this calibration technique is to utilize a portion of a track within
1814 the LArTPC that has a well known momentum and particle species to measure the
1815 stopping power (or energy deposited per unit length, dE/dX) as recorded inside the
1816 TPC. Once a sample of particles dE/dX has been measured at various momenta, we
1817 then tune to calorimetry constants within the reconstruction software to align these
1818 measured values to match the theoretical ones found in Figure 5.5.

1819 The calibration procedure follows the following steps:

- 1820 • **Species and Momentum Determination** We first select a sample of beam-
1821 line events that correspond to either a sample of π, μ, e , kaons or protons. This
1822 is done by selecting based on the invariant beamline mass as shown in section
1823 ?. The beamline particle is matched to the TPC information. In order to de-
1824 termine the particle momentum at the TPC front face, we use the momentum
1825 measured by the LArIAT spectrometer and we apply a flat correction for the
1826 energy loss between the beamline and the TPC. For the Monte Carlo, no such

1827 beamline identification is done and instead we generate DDMC for each particle
1828 species.

- 1829 • **dE/dX sampling:** With the track within the TPC identified and the momen-
1830 tumb for that track measured, we require the track to be of a minimum length
1831 of 10 cm long (to ensure we are away from any interaction point where the
1832 track may be broken into subsequent tracks). We then take the first twelve
1833 spacepoints of the track (excluding the first point to avoid edge effects near
1834 the field cage) and sample the reconstructed dE/dX for each point along the
1835 track. On average, this samples 5 cm of the track (shown in Section ??). These
1836 dE/dX measurements are then put into a histogram that corresponds to mea-
1837 sured momentum of the track. The dE/dX histograms are sampled every 50
1838 MeV in momentum (e.g. $150 \text{ MeV} < P < 200 \text{ MeV}$, $200 \text{ MeV} < P < 250 \text{ MeV}$,
1839 etc...). On average, pions and muons only lose ~ 10 MeV in this 5 cm section
1840 of the track and protons lose ~ 20 MeV. Thus choosing 50 MeV size bins for
1841 our histograms covers the energy spread within those bins due to energy loss
1842 from ionization. This process of selecting, sampling, and recording the dE/dX
1843 for various momentum bins is now repeated over the entire sample of events,
1844 allowing us to collect sufficient statistic in most of the momentum bins between
1845 150 MeV and 1100 MeV.

- 1846 • **Fit, tune, repeat:** Each 50 MeV momentum binned dE/dX histogram is now
1847 fit with a simple Landau function. The most probable value (MPV) and the
1848 associated error on the MPV from the fit are extracted and plotted on Figure
1849 5.5. Depending on the outcome of the fit, the calorimetry constants are either
1850 tuned up or down. The values are tuned for both the collection and induction
1851 plane to try to achieve the best possible match to the theoretical curve. The
1852 exact match is left as a qualitative exercise and is not quantitatively evaluated.

Figure 5.6: Illustration of the calibration technique. Here we depict a 325 MeV wire chamber track (shown in green) which enters the TPC (taking into account the energy loss from the upstream material) and we sample the first 12 spacepoints (shown in teal) to extract the dE/dX distribution which is fit with a Landau.

1853 5.4 Tracking Studies

1854 In this section, we describe three studies. The first is a justification of the selection
1855 criteria for the beamline handshake with the TPC information. We perform this
1856 study to boost the correct identification of the particles in the TPC associated with
1857 the beamline information, while maintaining sufficient statistics for the cross section
1858 measurement. The second study is an optimization of the tracking algorithm, with
1859 the scope of maximizing the identification of the hadronic interaction point inside the
1860 TPC. These two studies are related, since the optimization of the tracking is per-
1861 formed on TPC tracks which have been matched to the wire chamber track; in turn,
1862 the tracking algorithm for TPC tracks determine the number of reconstructed tracks
1863 in each event used to try the matching with the wire chamber track. Starting with
1864 a sensible tracking reconstruction, we perform the WC2TPC matching optimization
1865 first, then the tracking optimization. The WC2TPC match purity and efficiency are
1866 then calculated again with the optimized tracking.

1867 We perform the following studies on a MC sample of 191000 kaons and 359000
1868 pions produced with the DDMC technique. DDMC particles are shot from the WC4
1869 location into the TPC following the beam profile. We mimic the matching between the
1870 WC and the TPC track on Monte Carlo by constructing a fake WC track using truth
1871 information at wire chamber four. We then apply the same WC to TPC matching
1872 algorithm as in data described in 4.1.2.

1873 5.4.1 Selection Study for the Wire Chamber to TPC Match

1874 Plots I want in this section:

1875 1. WC2TPC MC DeltaX, DeltaY and α

1876 Scope of this study is assessing the goodness of the wire chamber to TPC match
1877 on Monte Carlo and decide the selection values we will use on data. A word of caution
1878 is necessary here. With this study, we want to minimize pathologies associated with
1879 the presence of the primary hadron itself, e.g. the incorrect association between the
1880 beamline hadron and its decay products inside the TPC. Assessing the contamination
1881 from pile-up¹, albeit related, is beyond the scope of this study.

1882 In MC, we are able to define a correct WC2TPC match using the Geant4 truth
1883 information. We are thus able to count how many times the WC tracks is associated
1884 with the wrong TPC reconstructed track.

1885 We define a correct match if the all following conditions are met:

- 1886 - the length of the true primary Geant4 track in the TPC is greater than 2 cm,
1887 - the length of the reconstructed track length is greater than 2 cm,
1888 - the Z position of the first reconstructed point is within 2 cm from the TPC
1889 front face
1890 - the distance between the reconstructed track and the true entering point is the
1891 minimum compared with all the other reconstructed tracks.

1892 In order to count the wrong matches, we consider all the reconstructed tracks
1893 whose Z position of the first reconstructed point lies within 2 cm from the TPC front
1894 face. Events with true length in TPC < 2 cm are included. Since hadrons are shot
1895 100 cm upstream from the TPC front face, the following two scenarios are possible
1896 from a truth standpoint:

1897 [Ta] the primary hadron decays or interact strongly before getting to the TPC,

1. We remind the reader that the DDMC is a single particle Monte Carlo, where the beam pile up is not simulated.

1898 [Tb] the primary hadron enters the TPC.

1899 Once we choose the selection cuts to determine a reconstructed wire chamber-
1900 to-TPC match r_T and α_T , the following five scenarios are possible in the truth to
1901 reconstruction interplay :

1902 1) only the correct track is matched

1903 2) only one wrong track is matched

1904 3) the correct track and one (or more) wrong tracks are matched

1905 4) multiple wrong tracks matched.

1906 5) no reconstructed tracks are matched

1907 Since we keep only events with one and only one match, we discard cases 3), 4)
1908 and 5) from the events used in the cross section measurement. For each set of r_T and
1909 α_T selection value, we define purity and efficiency of the selection as follows:

$$\text{Efficiency} = \frac{\text{Number of events correctly matched}}{\text{Number of events with primary in TPC}} \quad (5.1)$$

$$\text{Purity} = \frac{\text{Number of events correctly matched}}{\text{Total number of matched events}}. \quad (5.2)$$

1910 Figure 5.7 shows the efficiency (left) and purity (right) for wire chamber-to-TPC
1911 match as a function of the radius, r_T , and angle, α_T , selection value. It is apparent how
1912 both efficiency and purity are fairly flat as a function of the radius selection value at a
1913 given angle. This is not surprising. Since we are studying a single particle gun Monte
1914 Carlo sample, the wrong matches can occur only for mis-tracking of the primary or
1915 for association with decay products; decay products will tend to be produced at large
1916 angles compared to the primary, but could be fairly close to the in x and y projection
1917 of the primary. The radius cut would play a key role in removing pile up events.

1918 For LArIAT cross section measurements, we generally prefer purity over efficiency,
 1919 since a sample of particles of a pure species will lead to a better measurement. Ob-
 1920 viously, purity should be balanced with a sensible efficiency to avoid rejecting the
 1921 whole sample.

1922 We choose $(\alpha_T, r_T) = (8 \text{ deg}, 4 \text{ cm})$ and get a MC 85% efficiency and 98% purity
 1923 for the kaon sample and a MC BOH% efficiency and 98% purity for the BOH sample.

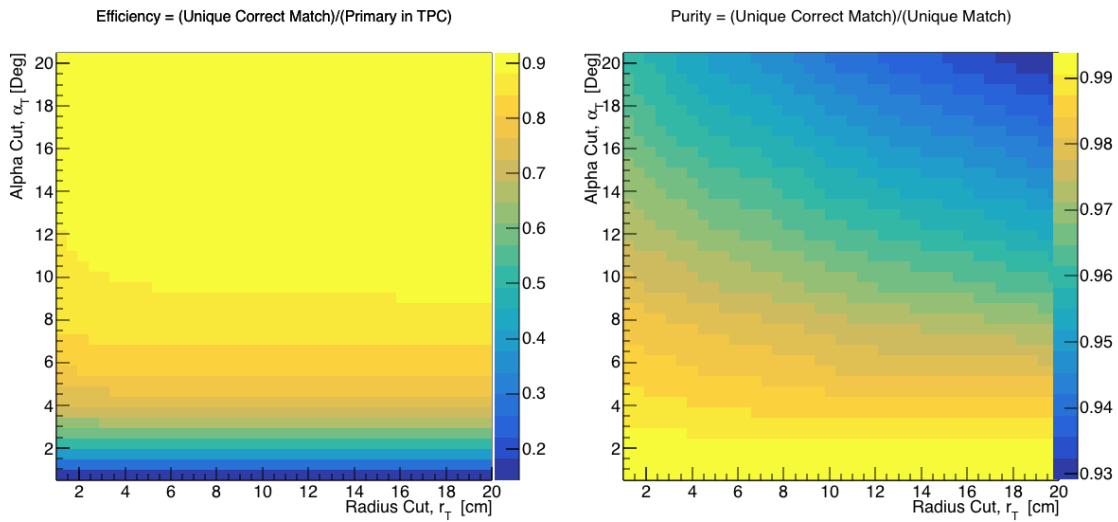


Figure 5.7: Efficiency (left) and purity (right) for wire chamber-to-TPC match as a function of the radius and angle selections.

1924 5.4.2 Interaction Point Optimization

1925 Scheme of this subsection

1926 **Brief Explanation of the reconstruction chain**

1927 **Explanation of clustering parameters**

1928 **Figure of merit and spanning of cluster**

1929 **Important numbers out of this optimization**

1930 Plots I want in this section:

- ¹⁹³¹ 1. Delta L, reco - true
- ¹⁹³² 2. Delta L, reco - true Elastic, Delta L, reco - true Inelastic, other
- ¹⁹³³ 3. Length Quality cut
- ¹⁹³⁴ 4. Efficiency as a function of true KE and Angle

¹⁹³⁵ 5.4.3 Tracking spatial and angular resolution

¹⁹³⁶ Scope of this study is understanding and comparing the tracking spatial and angular
¹⁹³⁷ resolution on data and MC. We start by selecting all the WC2TPC matched tracks.
¹⁹³⁸ We fit a line on all the space points of the track and calculate the χ^2 . The χ^2
¹⁹³⁹ distribution for data and MC is shown in Figure ??.

¹⁹⁴⁰ For the spatial and angular resolution study, we reject tracks with less than 14
¹⁹⁴¹ space points. For each track, we order the space points according to their Z position
¹⁹⁴² and we split them in two sets: the first set counts all the points belonging to the first
¹⁹⁴³ half of the track and the second set counts all the points belonging to the second half
¹⁹⁴⁴ of the track. We remove the last 5 points in the first set and the first 5 points in the
¹⁹⁴⁵ second set, so to have a gap in the middle of the original track. We fit the first and
¹⁹⁴⁶ the second set of points with a line separately. We reject the event entirely if the
¹⁹⁴⁷ χ^2 for the fit of either of the halves is greater than four. We define a track middle
¹⁹⁴⁸ plane as the plane perpendicular to the original track fit, positioned in the middle
¹⁹⁴⁹ of its length. We project the tracks on the middle plane and calculate the impact
¹⁹⁵⁰ parameter, d , i.e. the distance between the projected points. We also calculate the
¹⁹⁵¹ angle between the original track direction and the fit of the first and second half,
¹⁹⁵² called α_1 and α_2 respectively. The spatial resolution of the track will be $\sigma_S = \frac{d}{\sqrt{2}}$
¹⁹⁵³ while the angular resolution of the tracks will be $\sigma_\alpha = \alpha_1 - \alpha_2$. The distributions for
¹⁹⁵⁴ data and MC for σ_α and σ_S are given in ??.

¹⁹⁵⁵ Chapter 6

¹⁹⁵⁶ Background subtraction

¹⁹⁵⁷ 6.1 Assessing Beamline Contamination

¹⁹⁵⁸ Even if pions are by far the biggest beam component in negative polarity runs, the
¹⁹⁵⁹ LArIAT beam is not a pure pion beam. While useful to discriminate between pions,
¹⁹⁶⁰ kaons, and protons, the beamline detectors are not sensitive enough to discriminate
¹⁹⁶¹ among the lighter particles in the beam: electrons, muons and pions fall under the
¹⁹⁶² same mass hypothesis. Thus, we need to assess the contamination from beamline
¹⁹⁶³ particles other than pions in the event selections used for the pion cross section
¹⁹⁶⁴ analysis and correct for its effects.

¹⁹⁶⁵ We define beamline contamination every TPC track matched to the WC track
¹⁹⁶⁶ which is not a primary pion. Potentially, there are 4 different types of beamline
¹⁹⁶⁷ contaminations:

- ¹⁹⁶⁸ 1) electrons,
- ¹⁹⁶⁹ 2) muons,
- ¹⁹⁷⁰ 3) secondaries from pion events,
- ¹⁹⁷¹ 4) matched pile up events.

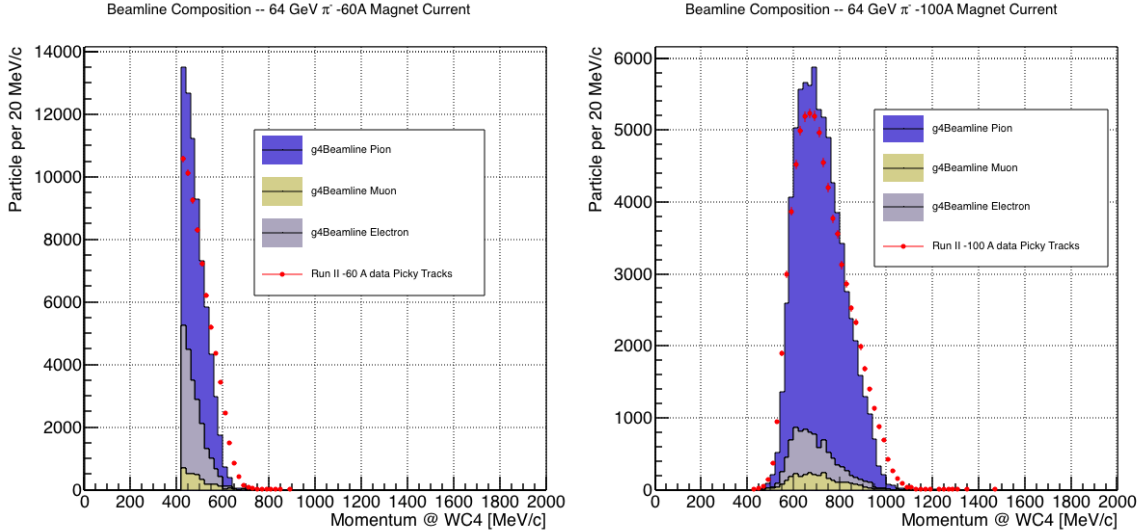


Figure 6.1: Beam composition for the -60A runs (left) and -100A runs (right). The solid blue plot represents the simulated pion content, the yellow plot represents the simulated muon content and the grey plot represents the simulated electron content. The plots are area normalized to the number of data events, shown in red.

1972 So, how do we handle this contamination? The first step is to estimate what
 1973 percentage of events used in the cross section calculation is not a primary pion. The
 1974 next two sections will illustrate this estimate for the electrons, muons and secondaries
 1975 from pion event. We estimate the last type of contamination, the “matched pile up”
 1976 events, to be a negligible fraction, because of the definition of the WC2TPC match:
 1977 we deem the probability of a single match with a halo particle in the absence of a
 1978 beamline particle¹ negligibly small.

1979 6.1.1 Electron and Muon contamination

1980 We estimate the percentage of electrons and muons in the beam via the G4Beamline
 1981 MC. Since the beamline composition is a function of the magnet settings, we simulate
 1982 separately events for magnet current of -60A and -100A.

1983 Table 6.1 shows the beam composition per magnet setting after the mass selection

1. Events with multiple WC2TPC matches are always rejected.

	I = -60 A	I = -100 A
G4Pions	68.8 %	87.4 %
G4Muons	4.6 %	3.7 %
G4Electrons	26.6 %	8.9 %

Table 6.1: Simulated beamline composition per magnet settings

	I = -60 A	I = -100 A	Total	w _{60A}	w _{100A}
N Data Events after Mass Selection	70192	76056	146248	0.48	0.52

Table 6.2: Number of data events which fit the pion mass hypothesis as a function of magnet settings. The last two columns represent the fraction of the data in the given magnet setting.

¹⁹⁸⁴ according to the G4Beamline simulation.

¹⁹⁸⁵ We calculate the electron to pion, as well as the muon to pion ratio on the whole
¹⁹⁸⁶ sample as the weighted sum of the corresponding ratio in the two current settings,

$$\frac{N_e}{N_{\pi} \text{Data}} = w_{60A} \frac{N_e}{N_{\pi} 60A} + w_{100A} \frac{N_e}{N_{\pi} 100A}, \quad (6.1)$$

$$\frac{N_{\mu}}{N_{\pi} \text{Data}} = w_{60A} \frac{N_{\mu}}{N_{\pi} 60A} + w_{100A} \frac{N_{\mu}}{N_{\pi} 100A}, \quad (6.2)$$

¹⁹⁸⁸ where the weights w_{60A} and w_{100A} are the percentage of events in the corresponding
¹⁹⁸⁹ magnet configuration passing the mass selection in data, as shown in table 6.2. Figure
¹⁹⁹⁰ 6.1 shows the momentum predictions from G4Beamline overlaid with data for the 60A
¹⁹⁹¹ runs (left) and for the 100A runs (right). The predictions for electrons, muons and
¹⁹⁹² pions have been staggered and their sum is area normalized to data. Albeit not
¹⁹⁹³ perfect, these plots show a reasonable agreement between the momentum shapes in
¹⁹⁹⁴ data and MC. We attribute the difference in shape to the lack of simulation of the
¹⁹⁹⁵ WC efficiency in the MC which is momentum dependent and leads to enhance the
¹⁹⁹⁶ number events in the center of the momentum distribution.

¹⁹⁹⁷ Once the beam composition is known, we simulate the electrons, muons and pi-
¹⁹⁹⁸ ons with the DDMC and we subject the three samples to the same selection chain

1999 (WC2TPC match, shower filter, pile up filter). The percentage of electrons and muons
2000 surviving the selection chain weighted by the beam composition is the electron and
2001 muon contamination in the pion cross section sample, as shown in Table 6.3.

2002 **6.1.2 Contamination from secondaries**

2003 Pions can travel the length of the LArIAT beamline and interact hadronically in the
2004 steel or in the non-instrumented argon upstream to the TPC front face. One of these
2005 products can leak into the TPC and be matched with the WC track, contributing
2006 to the pool of events used for the cross section calculation. We call this type of
2007 particles “secondaries” from pion events, with a terminology inspired by Geant4. We
2008 estimate the number of secondaries using the DDMC pion sample. The percentage of
2009 secondaries is given by the number of matched WC2TPC tracks whose corresponding
2010 particle is not flagged as primary by Geant4 and is not a muon, to avoid double
2011 counting with the G4Beamline estimate. The secondary to pion ratio is $X\%$ in the
2012 60A sample and $Y\%$ in the 100A sample.

2013 **6.2 Beamline Background Subtraction**

2014 Once we estimate the contaminants to primary pion ratio, the next step is subtracting
2015 their collective contribution from data. To do so, we simulate the same number of
2016 electrons, muons and pions with the DDMC separately for the two magnet settings,
2017 and we apply the same selection filters on the three samples. The number of events
2018 per particle species surviving this selection is shown on table 6.3.

2019 We then produce the interacting and incident histograms for the events surviving
2020 the selection for both the pions and the contaminants, weighted by the estimated
2021 beam composition.

2022 We then evaluate the relative contribution of the contaminants bin by bin in the

	π^- 60A	μ^- 60A	e^- 60A	π^- 100A	μ^- 100A	e^- 100A
Total Initial events	334500	334500	334500			
After Multiplicity Rejection	331313	322436	186261			
After WC2TPC: Selection	201458	285686	79109			
Evts After Shower Rejection	191655	277914	17477			
Survival rate	57%	83%	5%			
Beam Composition						
After Selection	88.5%	8.5%	3%			

Table 6.3: MC selection flow per particle species.

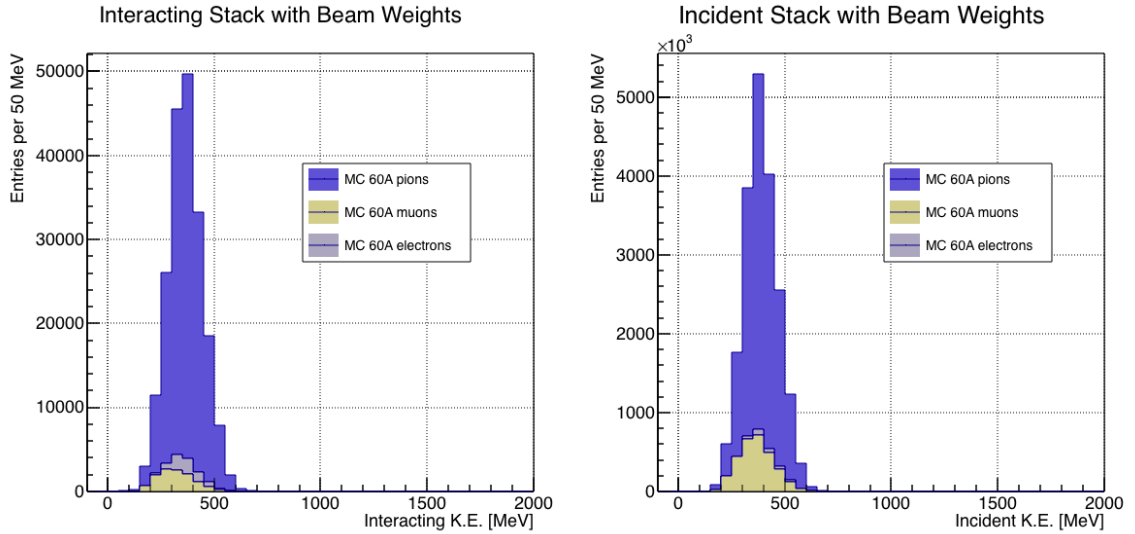


Figure 6.2: Left: staggered contributions to the interacting kinetic energy distribution for electron (grey), muons (yellow) and pion (blue) in the 60A simulation sample. Right: staggered contributions to the incident kinetic energy distribution for electron (grey), muons (yellow) and pion (blue) in the 60A simulation sample.

2023 interacting and incident histograms separately. In data, we subtract this estimated
 2024 relative contaminants contribution on the interacting and incident histograms bin by
 2025 bin.

2026 We estimate the systematic uncertainty on the cross section from this subtraction
 2027 procedure by varying the electron to pion and muon to pion ratio in a suitable range
 2028 of values. Figure

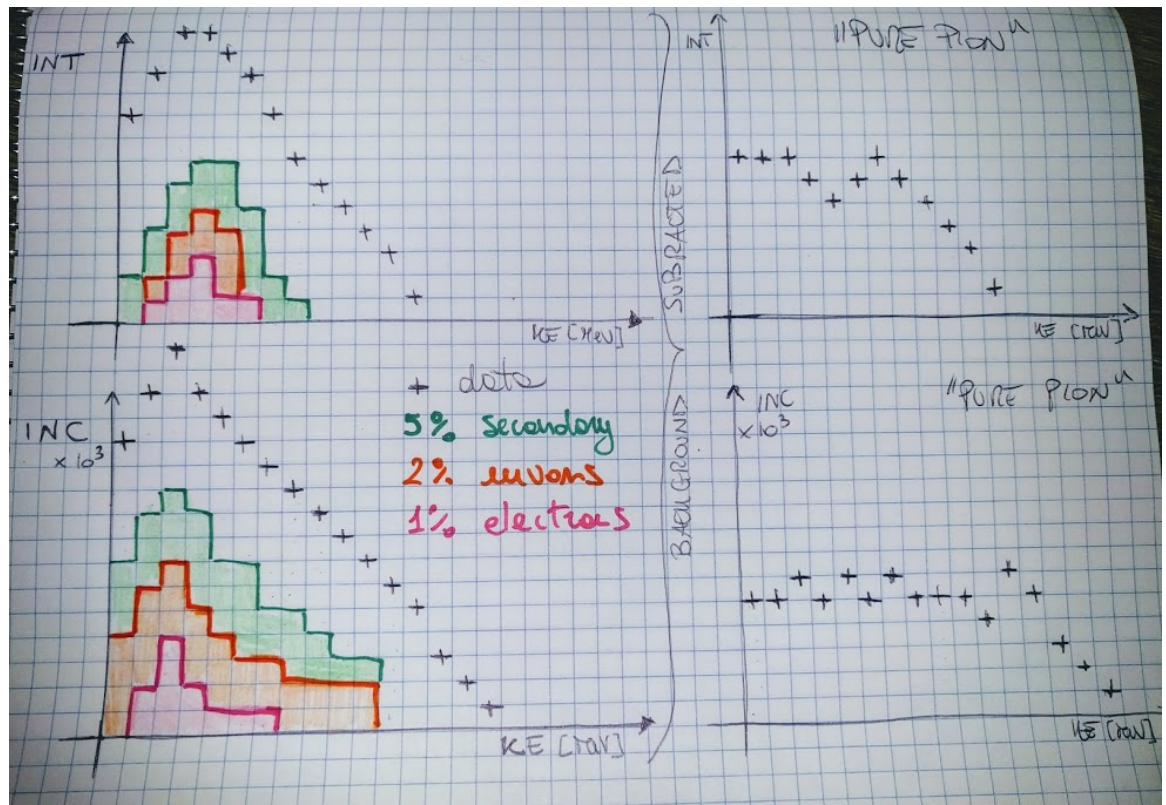


Figure 6.3: A graphical rendering of the beamline contamination background subtraction. The contribution of the contaminants is shown in green for the secondaries, in orange for the muons and in pink for electrons. The colored plots are coming from the MC and are staggered. The percentages shown in the legend are the percentages of contaminants over the total number of events passing the selection chain. We actually expect way less contamination.

2029 **6.3 Capture and decay**

2030 Our goal is to measure the total hadronic cross section for negative pions in argon.
2031 Since pion capture can be classified as an electromagnetic process and pion decay is a
2032 weak process, capture and decay represent unwanted interactions. We present here a
2033 study of capture and decay in Monte Carlo and the solution we adopted to mitigate
2034 their present in the data sample.

2035 For this MC study, we use a sample of 359000 MC pions generated according to
2036 the beam profile with the DDMC described in 5.2.2. It is important to notice that
2037 capture occurs predominantly at rest, while decay may occur both in flight and at
2038 rest. Thus, we can highly mitigate capture and decay at rest by removing pions
2039 which would release all their energy in the TPC and stop. This translates into a
2040 momentum selection, where we keep only events whose WC momentum is above a
2041 certain threshold. Figure 6.4 shows the true momentum distribution for the primary²
2042 pions that arrive to the TPC (pink), that capture (green) or decay (blue) inside the
2043 TPC, on a linear and log scale vertical axis.

2044 In order to choose the selection value for the wire chamber momentum, it is
2045 beneficial to estimate the ratio of events which capture or decay that survive the
2046 selection in MC as a function of the momentum threshold, and compare it with the
2047 survival ratio for all events. This is done in figure 6.5. We define the survival ratio
2048 simply as the number of events surviving the true momentum selection divided by
2049 the number of events of that category. We calculate the survival ratio separately for
2050 the three event categories explained above: total (pink), capture (green) and decay
2051 (blue). Selecting pions with momentum greater than 420 MeV/c reduces the capture
2052 events by 99% while maintaining about 80% of the total data sample. Figure 6.6

2. We use here the Geant4 denomination “primary” to indicate that the pion considered does not undergo interactions modifying its energy before getting to the TPC. In fact, not every pion shot from wire chamber four will arrive to the TPC as primary, some will decay or interact before the TPC.

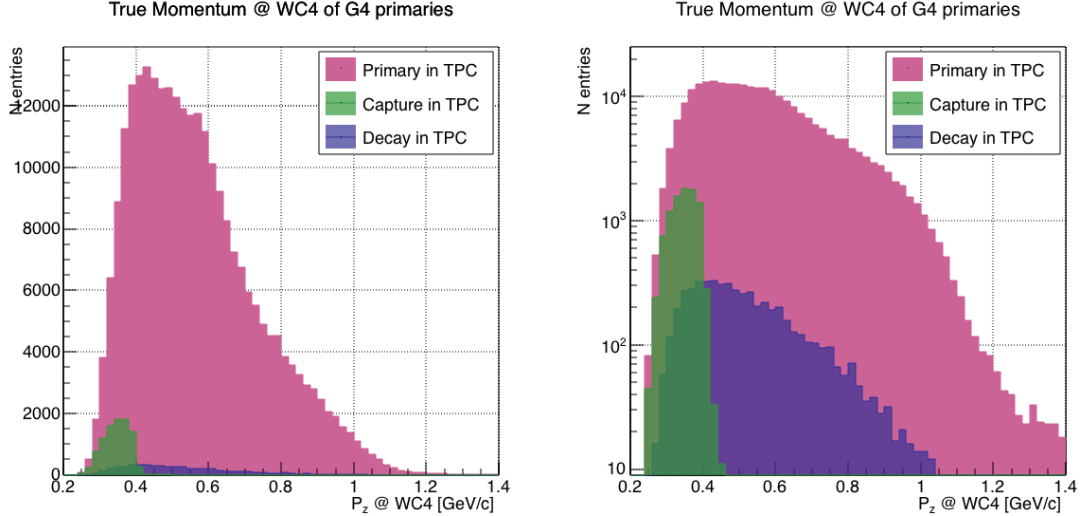


Figure 6.4: True momentum distribution at wire chamber 4 for every simulated pion arriving in the TPC (pink), ending its life in capture (green) or in decay (blue) in the TPC, linear vertical axis on the left, logarithmic on the right.

2053 shows the ratio of events which end their life in capture (green) or decay (blue) over
 2054 the total number of events as a function of the true momentum at wire chamber
 2055 four. This ratio is slightly dependent on the inelastic cross section implemented in
 2056 Geant4, as we are able to register a pion capture (or decay) only if it did not interact
 2057 inelastically in the TPC. We choose a momentum threshold of 420 MeV/c because
 2058 the percentage of capture events drops below 1% and the percentage of decays is
 2059 never above 2% for momenta greater than 420 MeV/c.

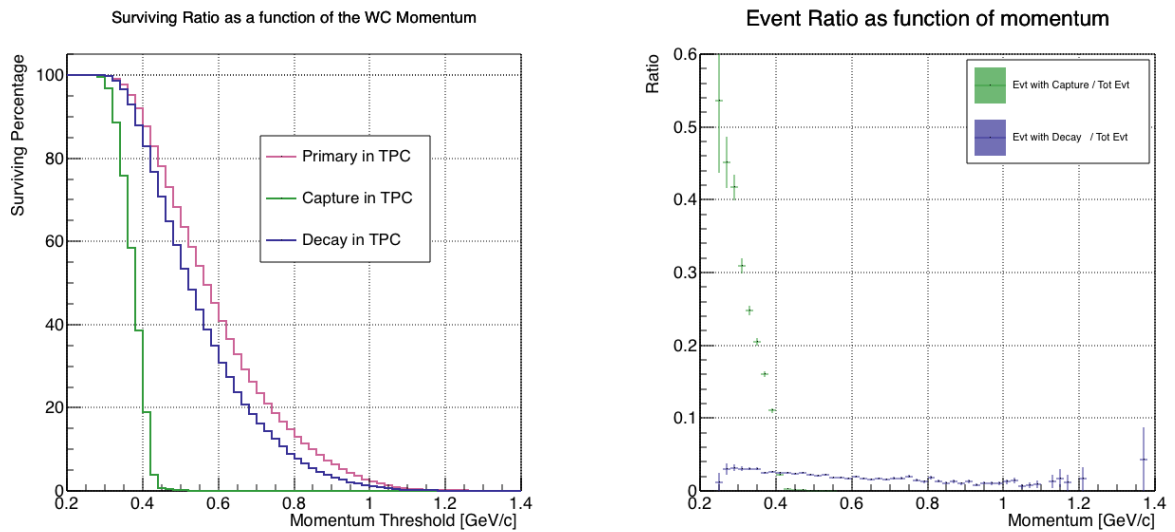


Figure 6.5: Survival ratio as a function of selection threshold on true momentum at wire chamber four for every simulated pion arriving in the TPC (pink), capture (green) or in decay (blue).

Figure 6.6: Ratio between the capture (green) and decay (blue) events over the total number of events as a function of the true momentum at wire chamber four.

2060 **Chapter 7**

2061 **Negative Pion Cross Section**

2062 **Measurement**

2063 **7.1 Estimate of E_{loss} before the TPC**

2064 The beamline particles travel a path from when their momentum is measured by
2065 the beamline detector, until they are tracked again inside the TPC. In the current
2066 LArIAT geometry, a particle leaving the fourth wire chamber will encounter the
2067 materials listed in Table 7.1 before being registered again. The energy lost by the
2068 particle in this non-instrumented material modifies the particle's kinetic energy and
2069 directly affects the cross section measurement, as shown in equation 4.5.

Material	density [g/cm ³]	width [cm]
Fiberglass laminate (G10)	1.7	1.28
Liquid Argon	1.4	3.20
Stainless Steel	7.7	0.23
Titanium	4.5	0.04
Air	$1.2 \cdot 10^{-3}$	89.43
Plastic Scintillator	1.03	1.20 (+ 1.30)

Table 7.1: LArIAT material budget from WC4 to the TPC Front Face.

We derive an estimate of the energy loss between the beamline momentum mea-

surement and the TPC (E_{loss}) from the Data Driven Monte Carlo using the pion and kaon samples separately, since this quantity is not measurable directly on data. The E_{loss} distribution for the 60A and 100A pion sample is shown in figure 7.1, left and right respectively. A clear double peaked structure is visible, which is due to the particles either missing or hitting the HALO paddle: a schematic rendering of this occurrence is shown in figure 7.2. The kinematic at WC4 determines the trajectory of a particle and whether or not it will hit the halo paddle. In figure 7.3 , we plot the true X component of the momentum versus the true X position at WC4 for pions missing the halo paddle (left) and for pions hitting the halo paddle (right) for the 60A MC simulation runs – analogous plots are obtained with the 100A simulation. These distributions can be separated drawing a line in this position-momentum space. We use a logistic regression [12] as a classifier to find the best separating line, shown in both plots as the red line. We classify as “hitting the halo paddle” all pions whose P_x and X are such that

$$P_x + 0.02 * X - 0.4 < 0$$

and as “missing the halo paddle” all pions whose P_x and X are such that

$$P_x + 0.02 * X - 0.4 > 0,$$

where the coefficients of the line are empirically found by the logistic regression estimation. Overall, this simple classifier classifies in the right category (hit or miss) about 86% of the pion events. We apply the same classifier on data. We assign $E_{loss} = 32 \pm 4$ MeV for events classified as “hitting the halo paddle”; we assign $E_{loss} = 24 \pm 3$ MeV for events classified as “missing the halo paddle”.

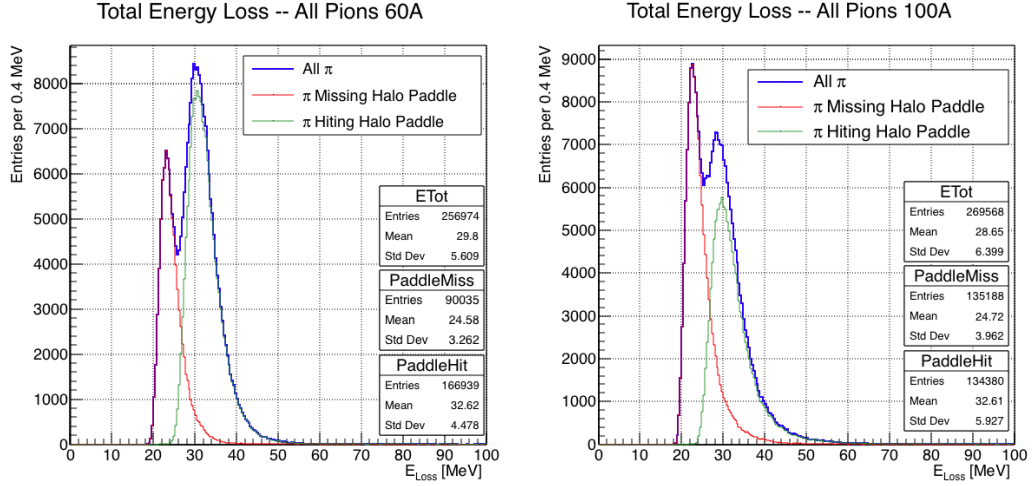


Figure 7.1: True energy loss between WC4 and the TPC front face according to the MC simulation of the 60A runs (left) and of the 100A runs (right). The distribution for the whole data sample is shown in blue, the distribution for the pions missing the halo is shown in red, and the distribution for the pions hitting the halo is shown in green.

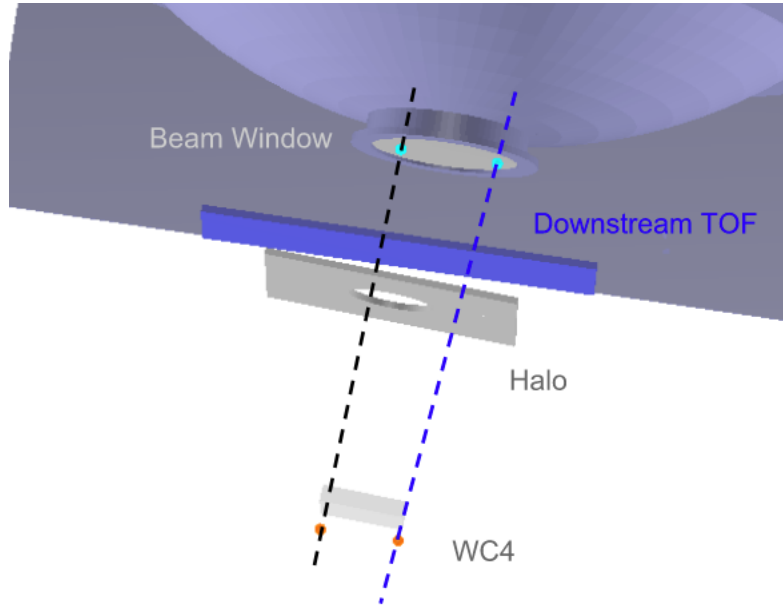


Figure 7.2: Schematic rendering of the particle path between WC4 and the TPC front face. The paddle with the hollow central circle represents the Halo paddle. We illustrate two possible trajectories: in black, a trajectory that miss the paddle and goes through the hole in the Halo, in blue a trajectory that hits the Halo paddle and goes through the scintillation material.

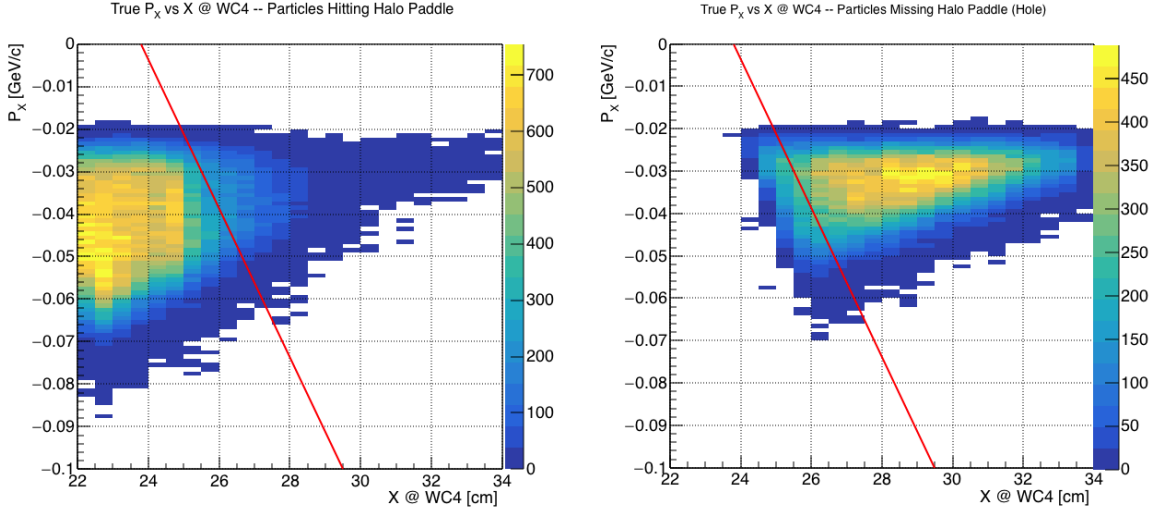


Figure 7.3: Horizontal component of the true momentum vs the horizontal position at WC4 for MC simulated pions of the 60A runs. The plot on the left shows the distribution for pion that miss the halo paddle and the plot on the right shows the distributions for pions that hit the halo. The form of the classifier is overlaid to both plots (red line).

2075 7.2 Interacting and Incident Distributions

2076 7.3 Total Hadronic Negative Pion-Argon Differen- 2077 tial Cross Section

2078 **Chapter 8**

2079 **Uncertainty budget**

2080 Measuring an hadronic cross section in LArIAT translates into counting how many
2081 hadrons impinged on a slab of argon at a given energy and how many of those hadrons
2082 interacted at said energy. So, the key questions here are:

- 2083 a) how well do we know the kinetic energy at each point of the tracking?
2084 b) how well do we know when the tracking stops?
2085 c) are there any systematic shifts?

2086 In order to answer this question, will discuss first a simple scenario were our beam
2087 is 100% made of pions which arrive as primaries in the TPC (no decay in the beam
2088 and no inelastic interaction before the TPC front face). We will then add a layer of
2089 complexity by discussing how we handle beamline contamination.

2090 **8.1 Pure beam of pions**

2091 Assuming a beam of pure pions gets to the TPC, let us explicit some of the vari-
2092 ables in the kinetic energy equation 4.6 to point out the important quantities in the
2093 uncertainty budget,

$$E_j^{kin} = E_{Beam}^{kin} - E_{loss} - \sum_{i < j} \frac{dE_i}{dx_i} * dx_i \quad (8.1)$$

$$= \sqrt{p_{Beam}^2 - m_{Beam}^2} - m_{Beam} - E_{loss} - \sum_{i < j} \frac{dE_i}{dx_i} * dx_i. \quad (8.2)$$

2094 8.1.1 Uncertainty on E_{Beam}^{kin}

2095 Let us start by discussing the uncertainty on E_{Beam}^{kin} . Since we are assuming a beam
 2096 of pions, the uncertainty on the value of mass of the pion (m_{Beam}) as given by the
 2097 pdg is irrelevant compared to the momentum uncertainties, thus $\delta E_{Beam}^{kin} = \delta p_{Beam}^{kin}$.
 2098 We estimate the momentum uncertainty as follows.

2099 We estimate the uncertainty on a 4-point track. In case of 3-points track, we add
 2100 an additional 2% coming from Greg's study. Uncertainty on a 4-point track:

- 2101 - Alignment surveys. 1mm misalignment translates to 3% in overall
- 2102 - Doug study dp/p = 2% based on field map (docdb 1710)
- 2103 - Minerva test beam paper

2104 8.1.2 Systematics on E_{loss}

2105 **Systematics** Discrepancies between the real TPC geometry and the simulated ge-
 2106 ometry can lead to a systematic in the E_{loss} calculation. In particular, we found a
 2107 difference in the depth of the un-instrumented argon upstream to the TPC front face,
 2108 the MC geometry reporting ~ 3.3 cm more un-instrumented argon than the TPC
 2109 survey. For a pion MIP, this depth corresponds to 7.4 MeV which we account for as
 2110 a double sided systematic in the determination of the pion kinetic energy.

2111 8.1.3 Uncertainty on dE/dx and pitch

2112 We obtain the uncertainty on dE/dx and track pitch by comparing the dE/dx and
2113 pitch distributions in data and MC. Currently, MPV MC = 1.70 and MPV DATA =
2114 1.72 MeV/cm (3% higher). TO DO HERE: calculate Argon density from mid-RTD
2115 temperature. Compare this density with MC Argon density. Density change affects
2116 dE/dx (in MeV/cm!). Try changing MC density up to “real one” and see if dEdX
2117 agrees between DATA and MC

2118 8.1.4 Uncertainty on track end, aka efficiency correction

2119 From the MC, we obtain an efficiency correction on the interacting and incident
2120 distributions separately. This is done by comparing the MC reconstructed with the
2121 true MC deposition on an event by event basis. This correction is applied bin by bin on
2122 the data interacting and incident distributions. The better our tracking, the smaller
2123 this efficiency correction will be. So, step number one is improving the tracking. Need
2124 to talk to Bruce about this. I don’t understand the angle cut that Dave Schmitz and
2125 Jon Paley were so vocal about.

2126 Now, the key question remains: does the tracking behave in the same way in
2127 data and MC? We can compare some key plots between reconstructed data and MC
2128 which gives us confidence this is true: the track pitch, the tracks straightness and the
2129 goodness of fit in data and MC. Does such a variable as “goodness of fit” exists in
2130 the tracking? We should ask Bruce.

2131 **Appendix A**

2132 **Measurement of LArIAT Electric**
2133 **Field**

2134 The electric field of a LArTPC in the drift volume is a fundamental quantity for
2135 the proper functionality of this technology, as it affects almost every reconstructed
2136 quantity such as the position of hits or their collected charge. Given its importance,
2137 we calculate the electric field for LArIAT with a single line diagram from our HV
2138 circuit and we cross check the obtained value with a measurement relying only on
2139 TPC data.

2140 Before getting into the details of the measurement procedures, it is important to
2141 explicit the relationship between some quantities in play. The electric field and the
2142 drift velocity (v_{drift}) are related as follows

$$v_{drift} = \mu(E_{field}, T)E_{field}, \quad (\text{A.1})$$

2143 where μ is the electron mobility, which depends on the electric field and on the
2144 temperature (T). The empirical formula for this dependency is described in [?] and
2145 shown in Figure A.1 for several argon temperatures.

2146 The relationship between the drift time (t_{drift}) and the drift velocity is trivially

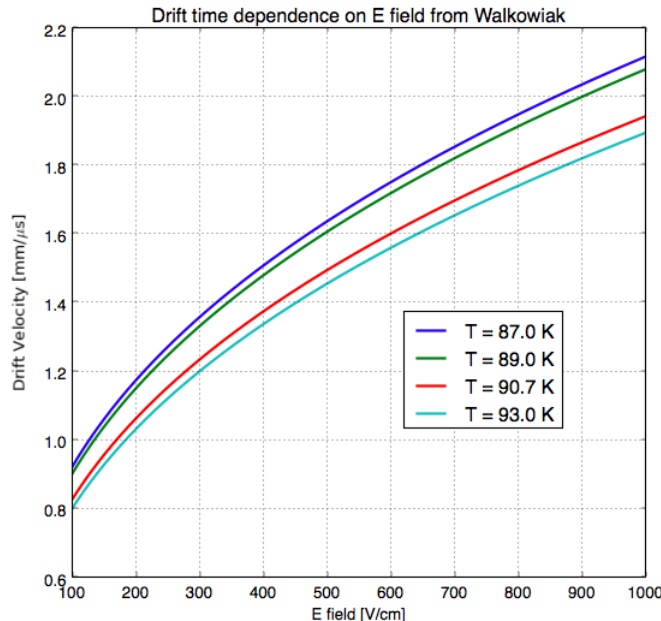


Figure A.1: Drift velocity dependence on electric field for several temperatures. The slope of the line at any one point represents the electron mobility for that given temperature and electric field.

Table A.1: Electric field and drift velocities in LArIAT smaller drift volumes

	Shield-Induction	Induction-Collection
E_{filed}	700.625 V/cm	892.5 V/cm
v_{drift}	1.73 mm/μs	1.90 mm/μs
t_{drift}	2.31 μs	2.11 μs

2147 given by

$$t_{drift} = \Delta x / v_{drift}, \quad (\text{A.2})$$

2148 where Δx is the distance between the edges of the drift region. Table A.1 reports the
2149 values of the electric field, drift velocity, and drift times for the smaller drift volumes.

2150 With these basic parameters established, we can now move on to calculating the
2151 electric field in the main drift region (between the cathode and the shield plane).

2152 Single line diagram method

2153 The electric field strength in the LArIAT main drift volume can be determined know-
 2154 ing the voltage applied to the cathode, the voltage applied at the shield plane, and the
 2155 distance between them. We assume the distance between the cathode and the shield
 2156 plane to be 470 mm and any length contraction due to the liquid argon is negligibly
 2157 small (~ 2 mm).

2158 The voltage applied to the cathode can be calculated using Ohm's law and the
 2159 single line diagram shown in Figure A.2. A set of two filter pots for emergency power
 2160 dissipation are positioned between the Glassman power supply and the cathode, one at
 2161 each end of the feeder cable, each with an internal resistance of $40 \text{ M}\Omega$. The output
 2162 current of the Glassman power supply is then used to determine the electric field
 2163 strength. Figure A.3 shows an average current of 0.004172 mA from the Glassman
 2164 power supply.

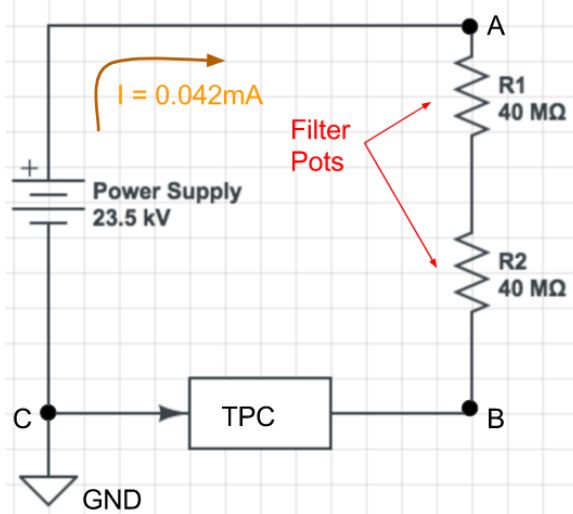


Figure A.2: get rid of current line LAr-IAT HV simple schematics.

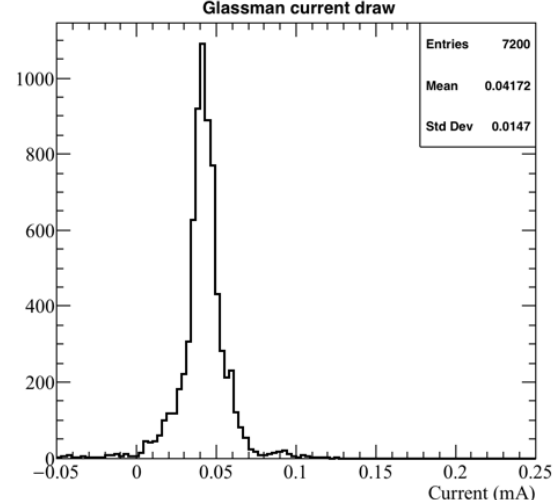


Figure A.3: **the axis is wrong!!** Current reading from the Glassman between May 25th and May 30th, 2016 (typical Run-II conditions).

2165 Using this current, the voltage at the cathode is calculated as

$$V_{BC} = V_{PS} - (I \times R_{eq}) = -23.5 \text{ kV} + (0.00417 \text{ mA} \times 80 \text{ M}\Omega) = -23.17 \text{ kV}, \quad (\text{A.3})$$

2166 where I is the current and R_{eq} is the equivalent resistor representing the two filter
2167 pots. The electric field, drift voltage, and drift time are then calculated to be

$$E_{\text{field}} = \frac{V_{BC} - V_{\text{shield}}}{\Delta x} = 486.54 \text{ V/cm} \quad (\text{A.4})$$

2168 **E field using cathode-anode piercing tracks**

2169 We devise an independent method to measure the drift time (and consequently drift
2170 velocity and electric field) using TPC cathode to anode piercing tracks. We use this
2171 method as a cross check to the single line method. The basic idea is simple:

- 2172 0. Select cosmic ray events with only 1 reconstructed track
- 2173 1. Reduce the events to the one containing tracks that cross both anode and
2174 cathode
- 2175 2. Identify the first and last hit of the track
- 2176 3. Measure the time difference between these two hits (Δt).

2177 This method works under the assumptions that the time it takes for a cosmic particle
2178 to cross the chamber ($\sim \text{ns}$) is small compared to the charge drift time ($\sim \text{hundreds}$
2179 of μs).

2180 We choose cosmic events to allow for a high number of anode to cathode piercing
2181 tracks (ACP tracks), rejecting beam events where the particles travel almost perpen-
2182 dicularly to drift direction. We select events with only one reconstructed track to
2183 maximize the chance of selecting a single crossing muon (no-michel electron). We
2184 utilize ACP tracks because their hits span the full drift length of the TPC, see figure

2185 A.4, allowing us to define where the first and last hit of the tracks are located in space
2186 regardless of our assumption of the electric field.

2187 One of the main features of this method is that it doesn't rely on the measurement
2188 of the trigger time. Since Δt is the time difference between the first and last hit of a
2189 track and we assume the charge started drifting at the same time for both hits, the
2190 measurement of the absolute beginning of drift time t_0 is unnecessary. We boost the
2191 presence of ACP tracks in the cosmic sample by imposing the following requirements
2192 on tracks:

- 2193 • vertical position (Y) of first and last hits within ± 18 cm from TPC center
2194 (avoid Top-Bottom tracks)
- 2195 • horizontal position (Z) of first and last hits within 2 and 86 cm from TPC front
2196 face (avoid through going tracks)
- 2197 • track length greater than 48 cm (more likely to be crossing)
- 2198 • angle from the drift direction (phi in figure A.5) smaller than 50 deg (more
2199 reliable tracking)
- 2200 • angle from the beam direction (theta in figure A.5) grater than 50 deg (more
2201 reliable tracking)

2202 Tracks passing all these selection requirements are used for the Δt calculation.

2203 For each track passing our selection, we loop through the associated hits in order
2204 to retrieve the timing information. The analysis is performed separately on hits on the
2205 collection plane and induction plane, but lead to consistent results. As an example
2206 of the time difference, figures A.6 and A.7 represent the difference in time between
2207 the last and first hit of the selected tracks for Run-II Positive Polarity sample on the
2208 collection and induction plane respectively. We fit with a Gaussian to the peak of the
2209 Δt distributions to extract the mean drift time and the uncertainty associated with

2210 it. The long tail at low Δt represent contamination of non-ACP tracks in the track
 2211 selection. We apply the same procedure to Run-I and Run-II, positive and negative
 2212 polarity alike.

2213 To convert Δt recorded for the hits on the induction plane to the drift time we
 2214 utilize the formula

$$t_{drift} = \Delta t - t_{S-I} \quad (\text{A.5})$$

2215 where t_{drift} is the time the charge takes to drift in the main volume between the
 2216 cathode and the shield plane and t_{S-I} is the time it takes for the charge to drift from
 2217 the shield plane to the induction plane. In Table A.1 we calculated the drift velocity
 2218 in the S-I region, thus we can calculate t_{S-I} as

$$t_{S-I} = \frac{l_{S-I}}{v_{S-I}} = \frac{4mm}{1.745mm/\mu s} \quad (\text{A.6})$$

2219 where l_{S-I} is the distance between the shield and induction plane and v_{S-I} is the drift
 2220 velocity in the same region. A completely analogous procedure is followed for the hits
 2221 on the collection plane, taking into account the time the charge spent in drifting from
 2222 shield to induction as well as between the induction and collection plane. The value
 2223 for Δt_{drift} , the calculated drift velocity (v_{drift}), and corresponding drift electric field
 2224 for the various run periods is given in Table A.2 and are consistent with the electric
 2225 field value calculated with the single line diagram method.

Delta t_{drift} , drift v and E field with ACP tracks

Data Period	Δt_{Drift} [μs]	Drift velocity [mm/ μs]	E field [V/cm]
RunI Positive Polarity Induction	311.1 ± 2.4	1.51 ± 0.01	486.6 ± 21
RunI Positive Polarity Collection	310.9 ± 2.6	1.51 ± 0.01	487.2 ± 21
RunII Positive Polarity Induction	315.7 ± 2.8	1.49 ± 0.01	467.9 ± 21
RunII Positive Polarity Collection	315.7 ± 2.7	1.49 ± 0.01	467.9 ± 21
RunII Negative Polarity Induction	315.9 ± 2.6	1.49 ± 0.01	467.1 ± 21
RunII Negative Polarity Collection	315.1 ± 2.8	1.49 ± 0.01	470.3 ± 21
Average Values	314.1	1.50 ± 0.01	474.3 ± 21

Table A.2: Δt for the different data samples used for the Anode-Cathode Piercing tracks study.

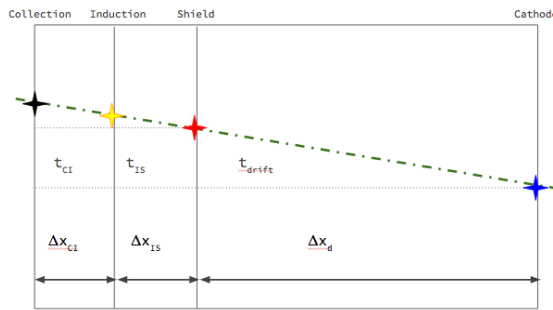


Figure A.4: Pictorial representation of the YX view of the TPC. The distance within the anode planes and between the shield plane and the cathode is purposely out of proportion to illustrate the time difference between hits on collection and induction. A ACP track is shown as an example.

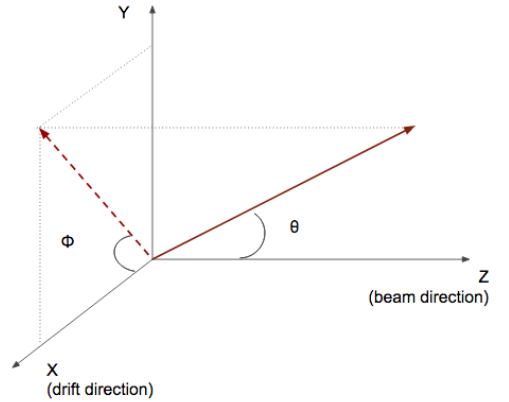


Figure A.5: Angle definition in the context of LArIAT coordinates system.

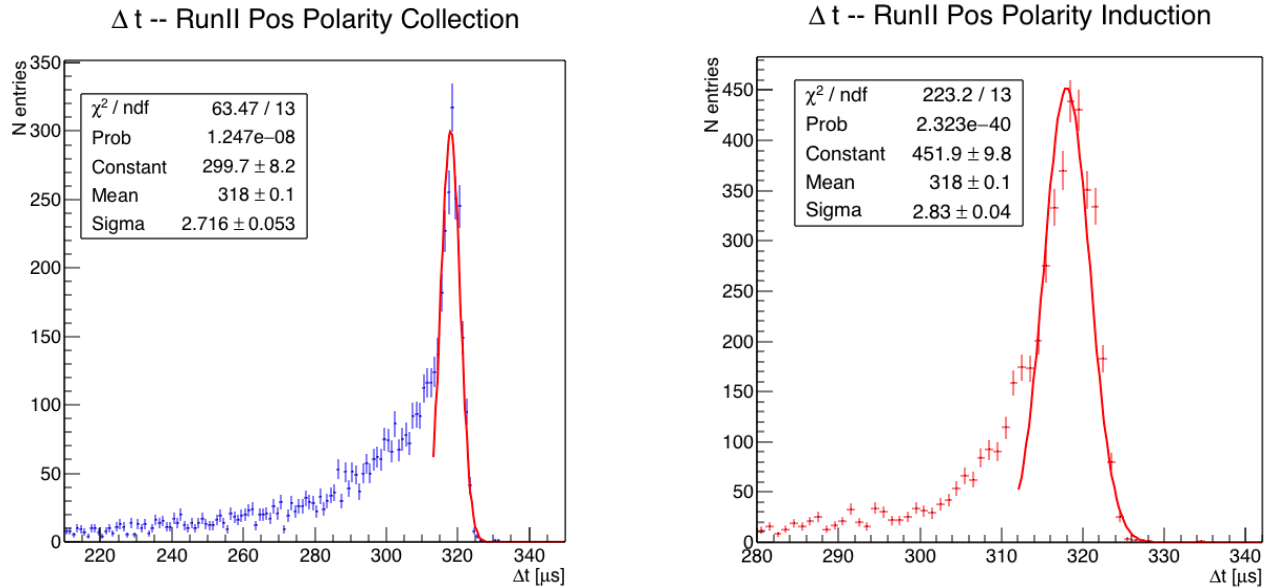


Figure A.6: Collection plane Δt fit for Run II positive polarity ACP data selected tracks.

Figure A.7: Induction plane Δt fit for Run II positive polarity ACP data selected tracks.

²²²⁶ Bibliography

- ²²²⁷ [1] Precision electroweak measurements on the Z resonance. *Physics Reports*,
²²²⁸ 427(5):257 – 454, 2006.
- ²²²⁹ [2] K. Abe, J. Amey, C. Andreopoulos, M. Antonova, S. Aoki, A. Ariga, D. Au-
²²³⁰ tiero, S. Ban, M. Barbi, G. J. Barker, G. Barr, C. Barry, P. Bartet-Friburg,
²²³¹ M. Batkiewicz, V. Berardi, S. Berkman, S. Bhadra, S. Bienstock, A. Blondel,
²²³² S. Bolognesi, S. Bordoni, S. B. Boyd, D. Brailsford, A. Bravar, C. Bronner,
²²³³ M. Buizza Avanzini, R. G. Calland, T. Campbell, S. Cao, S. L. Cartwright,
²²³⁴ M. G. Catanesi, A. Cervera, C. Checchia, D. Cherdack, N. Chikuma,
²²³⁵ G. Christodoulou, A. Clifton, J. Coleman, G. Collazuol, D. Coplowe, A. Cudd,
²²³⁶ A. Dabrowska, G. De Rosa, T. Dealtry, P. F. Denner, S. R. Dennis, C. Densham,
²²³⁷ D. Dewhurst, F. Di Lodovico, S. Di Luise, S. Dolan, O. Drapier, K. E. Duffy,
²²³⁸ J. Dumarchez, M. Dziewiecki, S. Emery-Schrenk, A. Ereditato, T. Feusels,
²²³⁹ A. J. Finch, G. A. Fiorentini, M. Friend, Y. Fujii, D. Fukuda, Y. Fukuda,
²²⁴⁰ V. Galymov, A. Garcia, C. Giganti, F. Gizzarelli, T. Golan, M. Gonin, D. R.
²²⁴¹ Hadley, L. Haegel, M. D. Haigh, D. Hansen, J. Harada, M. Hartz, T. Hasegawa,
²²⁴² N. C. Hastings, T. Hayashino, Y. Hayato, R. L. Helmer, A. Hillairet, T. Hiraki,
²²⁴³ A. Hiramoto, S. Hirota, M. Hogan, J. Holeczek, F. Hosomi, K. Huang, A. K.
²²⁴⁴ Ichikawa, M. Ikeda, J. Imber, J. Insler, R. A. Intonti, T. Ishida, T. Ishii, E. Iwai,
²²⁴⁵ K. Iwamoto, A. Izmaylov, B. Jamieson, M. Jiang, S. Johnson, P. Jonsson,
²²⁴⁶ C. K. Jung, M. Kabirnezhad, A. C. Kabeth, T. Kajita, H. Kakuno, J. Kameda,

2247 D. Karlen, T. Katori, E. Kearns, M. Khabibullin, A. Khotjantsev, H. Kim,
2248 J. Kim, S. King, J. Kisiel, A. Knight, A. Knox, T. Kobayashi, L. Koch, T. Koga,
2249 A. Konaka, K. Kondo, L. L. Kormos, A. Korzenev, Y. Koshio, K. Kowalik,
2250 W. Kropp, Y. Kudenko, R. Kurjata, T. Kutter, J. Lagoda, I. Lamont, M. Lam-
2251 oureux, E. Larkin, P. Lasorak, M. Laveder, M. Lawe, M. Licciardi, T. Lindner,
2252 Z. J. Liptak, R. P. Litchfield, X. Li, A. Longhin, J. P. Lopez, T. Lou, L. Ludovici,
2253 X. Lu, L. Magaletti, K. Mahn, M. Malek, S. Manly, A. D. Marino, J. F. Martin,
2254 P. Martins, S. Martynenko, T. Maruyama, V. Matveev, K. Mavrokordis, W. Y.
2255 Ma, E. Mazzucato, M. McCarthy, N. McCauley, K. S. McFarland, C. McGrew,
2256 A. Mefodiev, C. Metelko, M. Mezzetto, P. Mijakowski, A. Minamino, O. Mi-
2257 neev, S. Mine, A. Missert, M. Miura, S. Moriyama, Th. A. Mueller, J. Myslik,
2258 T. Nakadaira, M. Nakahata, K. G. Nakamura, K. Nakamura, K. D. Nakamura,
2259 Y. Nakanishi, S. Nakayama, T. Nakaya, K. Nakayoshi, C. Nantais, C. Nielsen,
2260 M. Nirko, K. Nishikawa, Y. Nishimura, P. Novella, J. Nowak, H. M. O'Keeffe,
2261 K. Okumura, T. Okusawa, W. Oryszczak, S. M. Oser, T. Ovsyannikova, R. A.
2262 Owen, Y. Oyama, V. Palladino, J. L. Palomino, V. Paolone, N. D. Patel,
2263 P. Paudyal, M. Pavin, D. Payne, J. D. Perkin, Y. Petrov, L. Pickard, L. Pick-
2264 ering, E. S. Pinzon Guerra, C. Pistillo, B. Popov, M. Posiadala-Zezula, J.-M.
2265 Poutissou, R. Poutissou, P. Przewlocki, B. Quilain, T. Radermacher, E. Radi-
2266 cioni, P. N. Ratoff, M. Ravonel, M. A. Rayner, A. Redij, E. Reinherz-Aronis,
2267 C. Riccio, P. A. Rodrigues, E. Rondio, B. Rossi, S. Roth, A. Rubbia, A. Rychter,
2268 K. Sakashita, F. Sánchez, E. Scantamburlo, K. Scholberg, J. Schwehr, M. Scott,
2269 Y. Seiya, T. Sekiguchi, H. Sekiya, D. Sgalaberna, R. Shah, A. Shaikhiev,
2270 F. Shaker, D. Shaw, M. Shiozawa, T. Shirahige, S. Short, M. Smy, J. T.
2271 Sobczyk, H. Sobel, M. Sorel, L. Southwell, J. Steinmann, T. Stewart, P. Stowell,
2272 Y. Suda, S. Suvorov, A. Suzuki, S. Y. Suzuki, Y. Suzuki, R. Tacik, M. Tada,
2273 A. Takeda, Y. Takeuchi, H. K. Tanaka, H. A. Tanaka, D. Terhorst, R. Terri,

2274 T. Thakore, L. F. Thompson, S. Tobayama, W. Toki, T. Tomura, C. Touramanis,
2275 T. Tsukamoto, M. Tzanov, Y. Uchida, M. Vagins, Z. Vallari, G. Vasseur,
2276 T. Vladislavljevic, T. Wachala, C. W. Walter, D. Wark, M. O. Wascko, A. We-
2277 ber, R. Wendell, R. J. Wilkes, M. J. Wilking, C. Wilkinson, J. R. Wilson, R. J.
2278 Wilson, C. Wret, Y. Yamada, K. Yamamoto, M. Yamamoto, C. Yanagisawa,
2279 T. Yano, S. Yen, N. Yershov, M. Yokoyama, K. Yoshida, T. Yuan, M. Yu, A. Za-
2280 lewska, J. Zalipska, L. Zambelli, K. Zaremba, M. Ziembicki, E. D. Zimmerman,
2281 M. Zito, and J. Źmuda. Combined analysis of neutrino and antineutrino oscil-
2282 lations at t2k. *Phys. Rev. Lett.*, 118:151801, Apr 2017.

2283 [3] K. Abe, Y. Haga, Y. Hayato, M. Ikeda, K. Iyogi, J. Kameda, Y. Kishimoto,
2284 M. Miura, S. Moriyama, M. Nakahata, T. Nakajima, Y. Nakano, S. Nakayama,
2285 A. Orii, H. Sekiya, M. Shiozawa, A. Takeda, H. Tanaka, T. Tomura, R. A. Wen-
2286 dell, R. Akutsu, T. Irvine, T. Kajita, K. Kaneyuki, Y. Nishimura, E. Richard,
2287 K. Okumura, L. Labarga, P. Fernandez, J. Gustafson, C. Kachulis, E. Kearns,
2288 J. L. Raaf, J. L. Stone, L. R. Sulak, S. Berkman, C. M. Nantais, H. A.
2289 Tanaka, S. Tobayama, M. Goldhaber, W. R. Kropp, S. Mine, P. Weatherly,
2290 M. B. Smy, H. W. Sobel, V. Takhistov, K. S. Ganezer, B. L. Hartfiel, J. Hill,
2291 N. Hong, J. Y. Kim, I. T. Lim, R. G. Park, A. Himmel, Z. Li, E. O’Sullivan,
2292 K. Scholberg, C. W. Walter, T. Wongjirad, T. Ishizuka, S. Tasaka, J. S. Jang,
2293 J. G. Learned, S. Matsuno, S. N. Smith, M. Friend, T. Hasegawa, T. Ishida,
2294 T. Ishii, T. Kobayashi, T. Nakadaira, K. Nakamura, Y. Oyama, K. Sakashita,
2295 T. Sekiguchi, T. Tsukamoto, A. T. Suzuki, Y. Takeuchi, T. Yano, S. V. Cao,
2296 T. Hiraki, S. Hirota, K. Huang, T. Kikawa, A. Minamino, T. Nakaya, K. Suzuki,
2297 Y. Fukuda, K. Choi, Y. Itow, T. Suzuki, P. Mijakowski, K. Frankiewicz, J. Hig-
2298 night, J. Imber, C. K. Jung, X. Li, J. L. Palomino, M. J. Wilking, C. Yanag-
2299 isawa, D. Fukuda, H. Ishino, T. Kayano, A. Kibayashi, Y. Koshio, T. Mori,
2300 M. Sakuda, C. Xu, Y. Kuno, R. Tacik, S. B. Kim, H. Okazawa, Y. Choi,

- 2301 K. Nishijima, M. Koshiba, Y. Totsuka, Y. Suda, M. Yokoyama, C. Bronner,
2302 M. Hartz, K. Martens, Ll. Marti, Y. Suzuki, M. R. Vagins, J. F. Martin, A. Kon-
2303 aka, S. Chen, Y. Zhang, and R. J. Wilkes. Search for proton decay via $p \rightarrow e^+ \pi^0$
2304 and $p \rightarrow \mu^+ \pi^0$ in 0.31 megaton·years exposure of the super-kamiokande water
2305 cherenkov detector. *Phys. Rev. D*, 95:012004, Jan 2017.
- 2306 [4] R Acciarri, C Adams, J Asaadi, B Baller, T Bolton, C Bromberg, F Ca-
2307 vanna, E Church, D Edmunds, A Ereditato, S Farooq, B Fleming, H Greenlee,
2308 G Horton-Smith, C James, E Klein, K Lang, P Laurens, D McKee, R Mehdiyev,
2309 B Page, O Palamara, K Partyka, G Rameika, B Rebel, M Soderberg, J Spitz,
2310 A M Szelc, M Weber, M Wojcik, T Yang, and G P Zeller. A study of electron
2311 recombination using highly ionizing particles in the argoneut liquid argon tpc.
2312 *Journal of Instrumentation*, 8(08):P08005, 2013.
- 2313 [5] R Acciarri, M Antonello, B Baibussinov, M Baldo-Ceolin, P Benetti,
2314 F Calaprice, E Calligarich, M Cambiaghi, N Canci, F Carbonara, F Cavanna,
2315 S Centro, A G Cocco, F Di Pompeo, G Fiorillo, C Galbiati, V Gallo, L Grandi,
2316 G Meng, I Modena, C Montanari, O Palamara, L Pandola, G B Piano Mortari,
2317 F Pietropaolo, G L Raselli, M Roncadelli, M Rossella, C Rubbia, E Segreto,
2318 A M Szelc, S Ventura, and C Vignoli. Effects of nitrogen contamination in
2319 liquid argon. *Journal of Instrumentation*, 5(06):P06003, 2010.
- 2320 [6] R. Acciarri et al. Demonstration and Comparison of Operation of Photomulti-
2321 plier Tubes at Liquid Argon Temperature. *JINST*, 7:P01016, 2012.
- 2322 [7] R. Acciarri et al. Design and Construction of the MicroBooNE Detector. *JINST*,
2323 12(02):P02017, 2017.
- 2324 [8] R. Acciarri et al. First Observation of Low Energy Electron Neutrinos in a
2325 Liquid Argon Time Projection Chamber. *Phys. Rev.*, D95(7):072005, 2017.

- 2326 [Phys. Rev.D95,072005(2017)].
- 2327 [9] M Adamowski, B Carls, E Dvorak, A Hahn, W Jaskierny, C Johnson, H Jostlein,
2328 C Kendziora, S Lockwitz, B Pahlka, R Plunkett, S Pordes, B Rebel, R Schmitt,
2329 M Stancari, T Tope, E Voirin, and T Yang. The liquid argon purity demon-
2330 strator. *Journal of Instrumentation*, 9(07):P07005, 2014.
- 2331 [10] C. Adams et al. The Long-Baseline Neutrino Experiment: Exploring Funda-
2332 mental Symmetries of the Universe. 2013.
- 2333 [11] P. Adamson, L. Aliaga, D. Ambrose, N. Anfimov, A. Antoshkin, E. Arrieta-
2334 Diaz, K. Augsten, A. Aurisano, C. Backhouse, M. Baird, B. A. Bambah,
2335 K. Bays, B. Behera, S. Bending, R. Bernstein, V. Bhatnagar, B. Bhuyan,
2336 J. Bian, T. Blackburn, A. Bolshakova, C. Bromberg, J. Brown, G. Brunetti,
2337 N. Buchanan, A. Butkevich, V. Bychkov, M. Campbell, E. Catano-Mur, S. Chil-
2338 dress, B. C. Choudhary, B. Chowdhury, T. E. Coan, J. A. B. Coelho, M. Colo,
2339 J. Cooper, L. Corwin, L. Cremonesi, D. Cronin-Hennessy, G. S. Davies, J. P.
2340 Davies, P. F. Derwent, R. Dharmapalan, P. Ding, Z. Djurcic, E. C. Dukes,
2341 H. Duyang, S. Edayath, R. Ehrlich, G. J. Feldman, M. J. Frank, M. Gabrielyan,
2342 H. R. Gallagher, S. Germani, T. Ghosh, A. Giri, R. A. Gomes, M. C. Goodman,
2343 V. Grichine, R. Group, D. Grover, B. Guo, A. Habig, J. Hartnell, R. Hatcher,
2344 A. Hatzikoutelis, K. Heller, A. Himmel, A. Holin, J. Hylen, F. Jediny, M. Judah,
2345 G. K. Kafka, D. Kalra, S. M. S. Kasahara, S. Kasetti, R. Keloth, L. Kolupaeva,
2346 S. Kotelnikov, I. Kourbanis, A. Kreymer, A. Kumar, S. Kurbanov, K. Lang,
2347 W. M. Lee, S. Lin, J. Liu, M. Lokajicek, J. Lozier, S. Luchuk, K. Maan, S. Mag-
2348 ill, W. A. Mann, M. L. Marshak, K. Matera, V. Matveev, D. P. Méndez, M. D.
2349 Messier, H. Meyer, T. Miao, W. H. Miller, S. R. Mishra, R. Mohanta, A. Moren,
2350 L. Mualem, M. Muether, S. Mufson, R. Murphy, J. Musser, J. K. Nelson,
2351 R. Nichol, E. Niner, A. Norman, T. Nosek, Y. Oksuzian, A. Olshevskiy, T. Ol-

- 2352 son, J. Paley, P. Pandey, R. B. Patterson, G. Pawloski, D. Pershey, O. Petrova,
2353 R. Petti, S. Phan-Budd, R. K. Plunkett, R. Poling, B. Potukuchi, C. Principato,
2354 F. Psihas, A. Radovic, R. A. Rameika, B. Rebel, B. Reed, D. Rocco, P. Rojas,
2355 V. Ryabov, K. Sachdev, P. Sail, O. Samoylov, M. C. Sanchez, R. Schroeter,
2356 J. Sepulveda-Quiroz, P. Shanahan, A. Sheshukov, J. Singh, J. Singh, P. Singh,
2357 V. Singh, J. Smolik, N. Solomey, E. Song, A. Sousa, K. Soustruznik, M. Strait,
2358 L. Suter, R. L. Talaga, M. C. Tamsett, P. Tas, R. B. Thayyullathil, J. Thomas,
2359 X. Tian, S. C. Tognini, J. Tripathi, A. Tsaris, J. Urheim, P. Vahle, J. Vasel,
2360 L. Vinton, A. Vold, T. Vrba, B. Wang, M. Wetstein, D. Whittington, S. G. Wo-
2361 jcicki, J. Wolcott, N. Yadav, S. Yang, J. Zalesak, B. Zamorano, and R. Zwaska.
2362 Constraints on oscillation parameters from ν_e appearance and ν_μ disappearance
2363 in nova. *Phys. Rev. Lett.*, 118:231801, Jun 2017.
- 2364 [12] Alan Agresti. *Categorical Data Analysis*. Wiley Series in Probability and Statis-
2365 tics. Wiley, 2013.
- 2366 [13] A. Aguilar-Arevalo et al. Evidence for neutrino oscillations from the observation
2367 of anti-neutrino(electron) appearance in a anti-neutrino(muon) beam. *Phys.*
2368 *Rev.*, D64:112007, 2001.
- 2369 [14] A. A. Aguilar-Arevalo et al. Improved Search for $\bar{\nu}_\mu \rightarrow \bar{\nu}_e$ Oscillations in the
2370 MiniBooNE Experiment. *Phys. Rev. Lett.*, 110:161801, 2013.
- 2371 [15] S. Amoruso et al. Study of electron recombination in liquid argon with the
2372 ICARUS TPC. *Nucl. Instrum. Meth.*, A523:275–286, 2004.
- 2373 [16] C. Anderson et al. The ArgoNeuT Detector in the NuMI Low-Energy beam
2374 line at Fermilab. *JINST*, 7:P10019, 2012.
- 2375 [17] C. Andreopoulos et al. The GENIE Neutrino Monte Carlo Generator. *Nucl.*
2376 *Instrum. Meth.*, A614:87–104, 2010.

- 2377 [18] M. Antonello, B. Baibussinov, P. Benetti, E. Calligarich, N. Canci, S. Centro,
2378 A. Cesana, K. Cieslik, D. B. Cline, A. G. Cocco, A. Dabrowska, D. De-
2379 qual, A. Dermenev, R. Dolfini, C. Farnese, A. Fava, A. Ferrari, G. Fiorillo,
2380 D. Gibin, S. Gninenko, A. Guglielmi, M. Haranczyk, J. Holeczek, A. Ivashkin,
2381 J. Kisiel, I. Kochanek, J. Lagoda, S. Mania, A. Menegolli, G. Meng, C. Monta-
2382 nari, S. Otwinowski, A. Piazzoli, P. Picchi, F. Pietropaolo, P. Plonski, A. Rap-
2383 poldi, G. L. Raselli, M. Rossella, C. Rubbia, P. Sala, A. Scaramelli, E. Seg-
2384 reto, F. Sergiampietri, D. Stefan, J. Stepaniak, R. Sulej, M. Szarska, M. Ter-
2385 rani, F. Varanini, S. Ventura, C. Vignoli, H. Wang, X. Yang, A. Zalewska,
2386 and K. Zaremba. Precise 3d track reconstruction algorithm for the ICARUS
2387 t600 liquid argon time projection chamber detector. *Advances in High Energy*
2388 *Physics*, 2013:1–16, 2013.
- 2389 [19] M. Antonello et al. A Proposal for a Three Detector Short-Baseline Neutrino
2390 Oscillation Program in the Fermilab Booster Neutrino Beam. 2015.
- 2391 [20] D. Ashery, I. Navon, G. Azuelos, H. K. Walter, H. J. Pfeiffer, and F. W.
2392 Schlepütz. True absorption and scattering of pions on nuclei. *Phys. Rev. C*,
2393 23:2173–2185, May 1981.
- 2394 [21] C. Athanassopoulos et al. Evidence for $\nu(\mu) \rightarrow \nu(e)$ neutrino oscillations
2395 from LSND. *Phys. Rev. Lett.*, 81:1774–1777, 1998.
- 2396 [22] Borut Bajc, Junji Hisano, Takumi Kuwahara, and Yuji Omura. Threshold
2397 corrections to dimension-six proton decay operators in non-minimal {SUSY}
2398 $su(5)$ {GUTs}. *Nuclear Physics B*, 910:1 – 22, 2016.
- 2399 [23] B. Baller. Trajcluster user guide. Technical report, apr 2016.
- 2400 [24] Gary Barker. Neutrino event reconstruction in a liquid argon TPC. *Journal of*
2401 *Physics: Conference Series*, 308:012015, jul 2011.

- 2402 [25] BASF Corp. 100 Park Avenue, Florham Park, NJ 07932 USA.
- 2403 [26] R. Becker-Szendy, C. B. Bratton, D. R. Cady, D. Casper, R. Claus, M. Crouch,
2404 S. T. Dye, W. Gajewski, M. Goldhaber, T. J. Haines, P. G. Halverson, T. W.
2405 Jones, D. Kielczewska, W. R. Kropp, J. G. Learned, J. M. LoSecco, C. Mc-
2406 Grew, S. Matsuno, J. Matthews, M. S. Mudah, L. Price, F. Reines, J. Schultz,
2407 D. Sinclair, H. W. Sobel, J. L. Stone, L. R. Sulak, R. Svoboda, G. Thornton,
2408 and J. C. van der Velde. Search for proton decay into $e^+ + \pi^0$ in the imb-3
2409 detector. *Phys. Rev. D*, 42:2974–2976, Nov 1990.
- 2410 [27] J B Birks. Scintillations from organic crystals: Specific fluorescence and relative
2411 response to different radiations. *Proceedings of the Physical Society. Section A*,
2412 64(10):874, 1951.
- 2413 [28] A. Bodek and J. L. Ritchie. Further studies of fermi-motion effects in lepton
2414 scattering from nuclear targets. *Phys. Rev. D*, 24:1400–1402, Sep 1981.
- 2415 [29] Mark G. Boulay and A. Hime. Direct WIMP detection using scintillation time
2416 discrimination in liquid argon. 2004.
- 2417 [30] D. V. Bugg, R. S. Gilmore, K. M. Knight, D. C. Salter, G. H. Stafford, E. J. N.
2418 Wilson, J. D. Davies, J. D. Dowell, P. M. Hattersley, R. J. Homer, A. W. O'dell,
2419 A. A. Carter, R. J. Tapper, and K. F. Riley. Kaon-nucleon total cross sections
2420 from 0.6 to 2.65 gev/ *c*. *Phys. Rev.*, 168:1466–1475, Apr 1968.
- 2421 [31] W. M. Burton and B. A. Powell. Fluorescence of tetraphenyl-butadiene in the
2422 vacuum ultraviolet. *Applied Optics*, 12(1):87, jan 1973.
- 2423 [32] A. S. Carroll, I. H. Chiang, C. B. Dover, T. F. Kycia, K. K. Li, P. O. Mazur,
2424 D. N. Michael, P. M. Mockett, D. C. Rahm, and R. Rubinstein. Pion-nucleus
2425 total cross sections in the (3,3) resonance region. *Phys. Rev. C*, 14:635–638,
2426 Aug 1976.

- 2427 [33] D. Casper. The nuance neutrino physics simulation, and the future. *Nuclear*
2428 *Physics B - Proceedings Supplements*, 112(1-3):161–170, nov 2002.
- 2429 [34] A. Cervera, A. Donini, M.B. Gavela, J.J. Gomez Cádenas, P. Hernández,
2430 O. Mena, and S. Rigolin. Golden measurements at a neutrino factory. *Nu-*
2431 *clear Physics B*, 579(1-2):17–55, jul 2000.
- 2432 [35] E. Church. LArSoft: A Software Package for Liquid Argon Time Projection
2433 Drift Chambers. 2013.
- 2434 [36] ATLAS Collaboration. Observation of a new particle in the search for the
2435 standard model higgs boson with the ATLAS detector at the LHC. *Physics*
2436 *Letters B*, 716(1):1–29, sep 2012.
- 2437 [37] CMS Collaboration. Observation of a new boson at a mass of 125 gev with the
2438 cms experiment at the lhc. *Physics Letters B*, 716(1):30 – 61, 2012.
- 2439 [38] The LArIAT Collaboration. The liquid argon in a testbeam (lariat) experiment.
2440 Technical report, In Preparation 2018.
- 2441 [39] Stefano Dell’Oro, Simone Marcocci, Matteo Viel, and Francesco Vissani. Neu-
2442 trinoless double beta decay: 2015 review. *Advances in High Energy Physics*,
2443 2016:1–37, 2016.
- 2444 [40] S.E. Derenzo, A.R. Kirschbaum, P.H. Eberhard, R.R. Ross, and F.T. Solmitz.
2445 Test of a liquid argon chamber with 20 m rms resolution. *Nuclear Instruments*
2446 *and Methods*, 122:319 – 327, 1974.
- 2447 [41] Savas Dimopoulos, Stuart Raby, and Frank Wilczek. Proton Decay in Super-
2448 symmetric Models. *Phys. Lett.*, B112:133, 1982.
- 2449 [42] D. Drakoulakos et al. Proposal to perform a high-statistics neutrino scattering
2450 experiment using a fine-grained detector in the NuMI beam. 2004.

- 2451 [43] A Ereditato, C C Hsu, S Janos, I Kreslo, M Messina, C Rudolf von Rohr,
2452 B Rossi, T Strauss, M S Weber, and M Zeller. Design and operation of
2453 argontube: a 5 m long drift liquid argon tpc. *Journal of Instrumentation*,
2454 8(07):P07002, 2013.
- 2455 [44] Torleif Ericson and Wolfram Weise. *Pions and Nuclei (The International Series*
2456 *of Monographs on Physics)*. Oxford University Press, 1988.
- 2457 [45] A.A. Aguilar-Arevalo et al. The miniboone detector. *Nuclear Instruments and*
2458 *Methods in Physics Research Section A: Accelerators, Spectrometers, Detectors*
2459 *and Associated Equipment*, 599(1):28 – 46, 2009.
- 2460 [46] Antonio Bueno et al. Nucleon decay searches with large liquid argon TPC de-
2461 tectors at shallow depths: atmospheric neutrinos and cosmogenic backgrounds.
2462 *Journal of High Energy Physics*, 2007(04):041–041, apr 2007.
- 2463 [47] A.S. Clough et al. Pion-nucleus total cross sections from 88 to 860 MeV. *Nuclear*
2464 *Physics B*, 76(1):15–28, jul 1974.
- 2465 [48] B.W. Allardyce et al. Pion reaction cross sections and nuclear sizes. *Nuclear*
2466 *Physics A*, 209(1):1 – 51, 1973.
- 2467 [49] C Athanassopoulos et al. The liquid scintillator neutrino detector and LAMPF
2468 neutrino source. *Nuclear Instruments and Methods in Physics Research Section*
2469 *A: Accelerators, Spectrometers, Detectors and Associated Equipment*, 388(1-
2470 2):149–172, mar 1997.
- 2471 [50] F. Binon et al. Scattering of negative pions on carbon. *Nuclear Physics B*,
2472 17(1):168 – 188, 1970.
- 2473 [51] L. Aliaga et al. Minerva neutrino detector response measured with test beam
2474 data. *Nuclear Instruments and Methods in Physics Research Section A: Ac-*

2475 *celerators, Spectrometers, Detectors and Associated Equipment*, 789:28 – 42,
2476 2015.

2477 [52] M Adamowski et al. The liquid argon purity demonstrator. *Journal of Instrumentation*, 9(07):P07005, 2014.

2479 [53] P. Vilain et al. Coherent single charged pion production by neutrinos. *Physics
2480 Letters B*, 313(1-2):267–275, aug 1993.

2481 [54] R. Acciarri et al. Convolutional neural networks applied to neutrino events
2482 in a liquid argon time projection chamber. *Journal of Instrumentation*,
2483 12(03):P03011, 2017.

2484 [55] R. Acciarri et al. Design and construction of the MicroBooNE detector. *Journal
2485 of Instrumentation*, 12(02):P02017–P02017, feb 2017.

2486 [56] C. E. Aalseth et al.l. DarkSide-20k: A 20 tonne two-phase LAr TPC for direct
2487 dark matter detection at LNGS. *The European Physical Journal Plus*, 133(3),
2488 mar 2018.

2489 [57] H Fenker. Standard beam pwc for fermilab. Technical report, Fermi National
2490 Accelerator Lab., Batavia, IL (USA), 1983.

2491 [58] H Fesbach. Theoretical nuclear physics: Nuclear reactions. 1992.

2492 [59] J. A. Formaggio and G. P. Zeller. From ev to eev: Neutrino cross sections across
2493 energy scales. *Rev. Mod. Phys.*, 84:1307–1341, Sep 2012.

2494 [60] E. Friedman et al. K+ nucleus reaction and total cross-sections: New analysis
2495 of transmission experiments. *Phys. Rev.*, C55:1304–1311, 1997.

2496 [61] V.M. Gehman, S.R. Seibert, K. Rielage, A. Hime, Y. Sun, D.-M. Mei,
2497 J. Maassen, and D. Moore. Fluorescence efficiency and visible re-emission

- 2498 spectrum of tetraphenyl butadiene films at extreme ultraviolet wavelengths.
2499 *Nuclear Instruments and Methods in Physics Research Section A: Accelerators,*
2500 *Spectrometers, Detectors and Associated Equipment*, 654(1):116 – 121, 2011.
- 2501 [62] H. Geiger and E. Marsden. On a diffuse reflection of the formula-particles.
2502 *Proceedings of the Royal Society A: Mathematical, Physical and Engineering*
2503 *Sciences*, 82(557):495–500, jul 1909.
- 2504 [63] Howard Georgi and S. L. Glashow. Unity of all elementary-particle forces. *Phys.*
2505 *Rev. Lett.*, 32:438–441, Feb 1974.
- 2506 [64] D.Y. Wong (editor) G.L. Shaw (Editor). *Pion-nucleon Scattering*. John Wiley
2507 & Sons Inc, 1969.
- 2508 [65] Glassman High Voltage, Inc., Precision Regulated High Voltage DC Power Sup-
2509 ply.
- 2510 [66] D S Gorbunov. Sterile neutrinos and their role in particle physics and cosmology.
2511 *Physics-Uspekhi*, 57(5):503, 2014.
- 2512 [67] C. Green, J. Kowalkowski, M. Paterno, M. Fischler, L. Garren, and Q. Lu. The
2513 Art Framework. *J. Phys. Conf. Ser.*, 396:022020, 2012.
- 2514 [68] S. Hansen, D. Jensen, G. Savage, E. Skup, and A. Soha. Fermilab test beam
2515 multi-wire proportional chamber tracking system upgrade. June 2014. Interna-
2516 tional Conference on Technology and Instrumentation in Particle Physics (TIPP
2517 2014).
- 2518 [69] J. Harada. Non-maximal θ_{23} , large θ_{13} and tri-bimaximal θ_{12} via quark-
2519 lepton complementarity at next-to-leading order. *EPL (Europhysics Letters)*,
2520 103(2):21001, 2013.

- 2521 [70] Peter W. Higgs. Broken symmetries and the masses of gauge bosons. *Physical*
2522 *Review Letters*, 13(16):508–509, oct 1964.
- 2523 [71] P.W. Higgs. Broken symmetries, massless particles and gauge fields. *Physics*
2524 *Letters*, 12(2):132–133, sep 1964.
- 2525 [72] H J Hilke. Time projection chambers. *Reports on Progress in Physics*,
2526 73(11):116201, 2010.
- 2527 [73] N. Ishida, M. Chen, T. Doke, K. Hasuike, A. Hitachi, M. Gaudreau, M. Kase,
2528 Y. Kawada, J. Kikuchi, T. Komiyama, K. Kuwahara, K. Masuda, H. Okada,
2529 Y.H. Qu, M. Suzuki, and T. Takahashi. Attenuation length measurements of
2530 scintillation light in liquid rare gases and their mixtures using an improved
2531 reflection suppresser. *Nuclear Instruments and Methods in Physics Research*
2532 *Section A: Accelerators, Spectrometers, Detectors and Associated Equipment*,
2533 384(2-3):380–386, jan 1997.
- 2534 [74] George Jaffé. Zur theorie der ionisation in kolonnen. *Annalen der Physik*,
2535 347(12):303–344, 1913.
- 2536 [75] C. Jarlskog. A basis independent formulation of the connection between quark
2537 mass matrices, CP violation and experiment. *Zeitschrift für Physik C Particles*
2538 *and Fields*, 29(3):491–497, sep 1985.
- 2539 [76] B J P Jones, C S Chiu, J M Conrad, C M Ignarra, T Katori, and M Toups. A
2540 measurement of the absorption of liquid argon scintillation light by dissolved ni-
2541 trogen at the part-per-million level. *Journal of Instrumentation*, 8(07):P07011,
2542 2013.
- 2543 [77] Benjamin J. P. Jones. *Sterile Neutrinos in Cold Climates*. PhD thesis, MIT,
2544 2015.

- 2545 [78] Cezary Juszczak, Jarosław A. Nowak, and Jan T. Sobczyk. Simulations from
2546 a new neutrino event generator. *Nuclear Physics B - Proceedings Supplements*,
2547 159:211–216, sep 2006.
- 2548 [79] D. I. Kazakov. Beyond the standard model: In search of supersymmetry. In
2549 *2000 European School of high-energy physics, Caramulo, Portugal, 20 Aug-2*
2550 *Sep 2000: Proceedings*, pages 125–199, 2000.
- 2551 [80] Dae-Gyu Lee, R. N. Mohapatra, M. K. Parida, and Merostar Rani. Predictions
2552 for the proton lifetime in minimal nonsupersymmetric $so(10)$ models: An
2553 update. *Phys. Rev. D*, 51:229–235, Jan 1995.
- 2554 [81] M A Leigui de Oliveira. Expression of Interest for a Full-Scale Detector Engi-
2555 neering Test and Test Beam Calibration of a Single-Phase LAr TPC. Technical
2556 Report CERN-SPSC-2014-027. SPSC-EOI-011, CERN, Geneva, Oct 2014.
- 2557 [82] W. H. Lippincott, K. J. Coakley, D. Gastler, A. Hime, E. Kearns, D. N. McK-
2558 insey, J. A. Nikkel, and L. C. Stonehill. Scintillation time dependence and pulse
2559 shape discrimination in liquid argon. *Phys. Rev. C*, 78:035801, Sep 2008.
- 2560 [83] Jorge L. Lopez and Dimitri V. Nanopoulos. Flipped SU(5): Origins and re-
2561 cent developments. In *15th Johns Hopkins Workshop on Current Problems*
2562 *in Particle Theory: Particle Physics from Underground to Heaven Baltimore,*
2563 *Maryland, August 26-28, 1991*, pages 277–297, 1991.
- 2564 [84] Vincent Lucas and Stuart Raby. Nucleon decay in a realistic $so(10)$ susy gut.
2565 *Phys. Rev. D*, 55:6986–7009, Jun 1997.
- 2566 [85] Ettore Majorana. Teoria simmetrica dell'elettrone e del positrone. *Il Nuovo*
2567 *Cimento*, 14(4):171–184, apr 1937.

- 2568 [86] Hisakazu Minakata and Alexei Yu. Smirnov. Neutrino mixing and quark-lepton
2569 complementarity. *Phys. Rev. D*, 70:073009, Oct 2004.
- 2570 [87] M. Mooney. The microboone experiment and the impact of space charge effects.
2571 2015.
- 2572 [88] E. Morikawa, R. Reininger, P. Gurtler, V. Saile, and P. Laporte. Argon, kryp-
2573 ton, and xenon excimer luminescence: From the dilute gas to the condensed
2574 phase. *The Journal of Chemical Physics*, 91(3):1469–1477, aug 1989.
- 2575 [89] FM Newcomer, S Tedja, R Van Berg, J Van der Spiegel, and HH Williams.
2576 A fast, low power, amplifier-shaper-discriminator for high rate straw tracking
2577 systems. *IEEE Transactions on Nuclear Science*, 40(4):630–636, 1993.
- 2578 [90] Emmy Noether. Invariant variation problems. *Transport Theory and Statistical
2579 Physics*, 1(3):186–207, jan 1971.
- 2580 [91] I. Nutini. Study of charged particles interaction processes on ar in the 0.2 - 2.0
2581 GeV energy range through combined information from ionization free charge
2582 and scintillation light. Technical report, jan 2015.
- 2583 [92] D. R. Nygren. The time projection chamber: A new 4π detector for charged
2584 particles. Technical report, 1974.
- 2585 [93] L. Onsager. Initial recombination of ions. *Phys. Rev.*, 54:554–557, Oct 1938.
- 2586 [94] S. Pascoli, S.T. Petcov, and A. Riotto. Leptogenesis and low energy cp-violation
2587 in neutrino physics. *Nuclear Physics B*, 774(1):1 – 52, 2007.
- 2588 [95] C. Patrignani et al. Review of Particle Physics. *Chin. Phys.*, C40(10):100001,
2589 2016.

- 2590 [96] B. Pontecorvo. Neutrino Experiments and the Problem of Conservation of
2591 Leptonic Charge. *Sov. Phys. JETP*, 26:984–988, 1968. [Zh. Eksp. Teor.
2592 Fiz.53,1717(1967)].
- 2593 [97] T. Yang R. Acciarri, M. Stancari. Determination of the electron lifetime in
2594 lariat. Technical report, March 2016.
- 2595 [98] Martti Raidal. Relation between the neutrino and quark mixing angles and
2596 grand unification. *Phys. Rev. Lett.*, 93:161801, Oct 2004.
- 2597 [99] Steve Ritz et al. Building for Discovery: Strategic Plan for U.S. Particle Physics
2598 in the Global Context. 2014.
- 2599 [100] C. Rubbia. The Liquid Argon Time Projection Chamber: A New Concept for
2600 Neutrino Detectors. 1977.
- 2601 [101] L.M. Saunders. Electromagnetic production of pions from nuclei. *Nucl. Phys.*,
2602 *B7*: 293-310(1968).
- 2603 [102] Qaisar Shafi and Zurab Tavartkiladze. Neutrino democracy, fermion mass hier-
2604 archies, and proton decay from 5d su(5). *Phys. Rev. D*, 67:075007, Apr 2003.
- 2605 [103] Sigma-Aldrich, P.O. Box 14508, St. Louis, MO 63178 USA.
- 2606 [104] R. K. Teague and C. J. Pings. Refractive index and the lorentz–lorenz function
2607 for gaseous and liquid argon, including a study of the coexistence curve near the
2608 critical state. *The Journal of Chemical Physics*, 48(11):4973–4984, jun 1968.
- 2609 [105] J. Thomas and D. A. Imel. Recombination of electron-ion pairs in liquid argon
2610 and liquid xenon. *Phys. Rev. A*, 36:614–616, Jul 1987.
- 2611 [106] D.R.O. Morrison N. Rivoire V. Flaminio, W.G. Moorhead. Compilation of
2612 Cross Sections I: π^+ and π^- Induced Reactions. *CERN-HERA*, pages 83–01,
2613 1983.

- 2614 [107] D.R.O. Morrison N. Rivoire V. Flaminio, W.G. Moorhead. Compilation of
2615 Cross Sections II: K^+ and K^- Induced Reactions. *CERN-HERA*, pages 83–02,
2616 1983.
- 2617 [108] Hermann Weyl. Gravitation and the electron. *Proceedings of the National
2618 Academy of Sciences of the United States of America*, 15(4):323–334, 1929.
- 2619 [109] Colin et al Wilkin. A comparison of pi+ and pi- total cross-sections of light
2620 nuclei near the 3-3 resonance. *Nucl. Phys.*, B62:61–85, 1973.
- 2621 [110] D. H. Wright and M. H. Kelsey. The Geant4 Bertini Cascade. *Nucl. Instrum.
2622 Meth.*, A804:175–188, 2015.
- 2623 [111] C. S. Wu, E. Ambler, R. W. Hayward, D. D. Hoppes, and R. P. Hudson.
2624 Experimental test of parity conservation in beta decay. *Phys. Rev.*, 105:1413–
2625 1415, Feb 1957.
- 2626 [112] N Yahlali, L M P Fernandes, K Gonzlez, A N C Garcia, and A Soriano. Imaging
2627 with sipms in noble-gas detectors. *Journal of Instrumentation*, 8(01):C01003,
2628 2013.
- 2629 [113] T. Yanagida. Horizontal symmetry and masses of neutrinos. *Progress of Theo-
2630 retical Physics*, 64(3):1103–1105, sep 1980.